

Metabolite interactions in the bacterial Calvin cycle and implications for flux regulation

Emil Sporre^{1*}, Jan Karlsen^{1*}, Karen Schriever², Johannes Asplund Samuelsson¹, Markus Janasch¹, David Koto¹, Linnéa Strandberg¹, Luise Zeckey¹, Ilaria Piazza³, Per-Olof Syrén², Fredrik Edfors¹, Elton P. Hudson^{1a}.

¹ Department of Protein Science, Science for Life Laboratory, KTH - Royal Institute of Technology, Stockholm, Sweden

² Department of Fibre and Polymer Technology, Science for Life Laboratory, KTH - Royal Institute of Technology, Stockholm, Sweden

³ Max Delbrück Center for Molecular Medicine in the Helmholtz Association (MDC Berlin), Berlin, Germany

* equal contribution

^a correspondence: paul.hudson@scilifelab.se

Abstract

Metabolite-level regulation of enzyme activity is important for coping with environmental shifts. Recently developed proteomics methodologies allow for mapping of post-translational interactions, including metabolite-protein interactions, that may be relevant for quickly regulating pathway activity. While feedback and feedforward regulation in glycolysis has been investigated, there is relatively little study of metabolite-level regulation in the Calvin cycle, particularly in bacteria. Here, we applied limited proteolysis small molecule mapping (LiP-SMap) to identify metabolite-protein interactions in four Calvin-cycle harboring bacteria, including two cyanobacteria and two chemolithoautotrophs. We identified widespread protein interactions with the metabolites GAP, ATP, and AcCoA in all strains. Some species-specific interactions were also observed, such as sugar phosphates in *Cupriavidus necator* and glyoxylate in *Synechocystis* sp. PCC 6803. We screened some metabolites with LiP interactions for their effects on kinetics of the enzymes F/SBPase and transketolase, two enzymatic steps of the Calvin cycle. For both *Synechocystis* and *Cupriavidus* F/SBPase, GAP showed an activating effect that may be part of feed-forward regulation in the Calvin cycle. While we verified multiple enzyme inhibitors on transketolase, the effect on kinetics was often small. Incorporation of F/SBPase and transketolase regulations into a kinetic metabolic model of *Synechocystis* central metabolism resulted in a general decreased stability of the network, and altered flux control coefficients of transketolase as well as other reactions. The LiP-SMap methodology is promising for uncovering new modes of metabolic regulation, but will benefit from improved peptide quantification and higher peptide coverage of enzymes, as known interactions are often not detected for low-coverage proteins. Furthermore, not all LiP interactions appear to be relevant for catalysis, as 4/8 (transketolase) and 5/6 (F/SBPase) of the tested LiP effectors had an effect in *in vitro* assays.

Introduction

Interaction proteomics coupled with mass spectrometry is emerging as a powerful tool for identifying proteome-wide post-translational regulations (Mateus et al., 2021). Limited proteolysis (LiP) and thermal proteome profiling (TPP) detect changes in protein conformation or melting temperature that occur when a protein undergoes conformational change or binds to other proteins, metabolites, or metal ions, without reliance on immuno-based enrichment or crosslinking. The techniques have provided insights into gene regulation in diverse biological systems. Thermal proteome profiling, which infers post-translational regulation through co-variance of proteins' melting temperatures, was developed to identify specific and secondary drug interactions in the proteome of mammalian cell models (Savitski et al., 2014; Tan et al., 2018). Variations of the technique have also been applied to microbes. Thermal melting curves of the *E. coli* proteome during the stationary phase showed that approximately 40 proteins had differential thermal stability compared to during exponential growth, and many of these were enzymes whose usage was expected to be altered in stationary phase (Mateus et al., 2018). The thermal stability of many proteins in cyanobacteria were shown to be altered in the day-night cycle, and these were coordinated by the circadian clock protein in response to energy status (Pattanayak et al. 2020). Thermal proteome profiling has also been used for metabolic engineering. Li et al. identified squalene synthase in *S. cerevisiae* as an essential enzyme with low thermal stability. Replacing it with an ortholog from a thermophilic yeast increased the survivable growth temperature of *S. cerevisiae* (Li et al., 2021).

Limited proteolysis is based on a protein's susceptibility to proteinase K digestion, which can be tracked proteome-wide using mass spectrometry. The digestion pattern of a protein may change due to a change in protein conformation which may be caused by biophysical interactions or post-translational modifications. Limited proteolysis performed on the proteome of yeast grown on ethanol showed that hundreds of proteins had different digestion patterns when compared to sugar-grown cells, indicating post-translational regulation during substrate shifts (Feng et al., 2014b). A variant of the limited proteolysis technique is to perform the proteinase K digestion of the extracted proteome in the presence of an added metabolite. In LiP-SMap (limited proteolysis-small molecule mapping), primary interactions of proteins with metabolites, or secondary effects such as protein-protein complexation, are revealed by comparison of digestion patterns with or without the added effector (Piazza et al. 2018). Protein-metabolite interactions are critical for adapting metabolic flux to changing conditions (Zampieri et al., 2019). To demonstrate and benchmark the LiP-SMap technique, Piazza et al. treated yeast and *E. coli* extracts with metabolites and monitored changes in the LiP digestion patterns (Piazza et al., 2018). Hundreds of metabolite-protein interactions were detected that were not previously known, and in many cases the altered peptides could be mapped near the enzyme active site. Among multiple sugar phosphates with widespread interactions in *E. coli* central metabolism, FBP was validated to alter the binding affinity of G6PDH for its substrate G6P.

A relatively unexplored application area for interaction proteomics is the Calvin cycle, present in diverse bacteria as well as eukaryotic algae and plants. The bacterial Calvin cycle is of biotechnological interest as cyanobacteria and chemolithoautotrophic bacteria have been modified to produce biochemicals from carbon dioxide using sunlight, electricity, or hydrogen as reducing power (Koch et al., 2020; Krieg et al., 2018; Liu et al., 2019; Müller et

al., 2013). An understanding of metabolite-level regulation of Calvin cycle enzymes, or central metabolic pathways where the Calvin cycle is enmeshed, could inform future metabolic engineering strategies. The Calvin cycle is autocatalytic, so that fixed carbon must be partitioned out of the cycle for anabolism, but also retained in order to regenerate the carbon dioxide fixation substrate ribulose 1,5-bisphosphate. The cycle is susceptible to instability at branch points where intermediates are drained, and the possible relative substrate affinities of cycle enzymes and branching enzymes are constrained (Barenholz et al., 2017; Janasch et al., 2019). Modulation of enzyme kinetic parameters (K_M , K_i , k_{cat}), such as by allosteric or competitive effectors, would thus be expected to affect cycle stability. While regulation of the Calvin cycle enzymes in plants has been extensively studied (Martin et al., 2000; Michelet et al., 2013; Raines, 2003), the Calvin cycle in bacteria is less characterized, particularly with respect to potential post-translational regulation. In light of the widespread distribution of the bacterial Calvin cycle, regulation may be different across species.

The freshwater cyanobacterium *Synechocystis* sp. PCC 6803 is a model for studying photosynthesis, particularly because it can also metabolize glucose, allowing for knockout of genes essential for autotrophy (Shen and Vermaas, 1994). *Synechococcus elongatus* PCC 7942 is an obligate photoautotroph, and a model strain for studying the circadian rhythm (Cohen and Golden, 2015). It was found that *Synechocystis* contains a larger number of isoenzymes than *Synechococcus*, which may be related to its metabolic versatility (Beck et al., 2012; Jablonsky et al., 2016). There is evidence of post-translational regulation in the Calvin cycle among cyanobacteria. For example, when metabolites are “drained” from the Calvin cycle, e.g. by sucrose formation and secretion in *Synechococcus* or ethanol synthesis in *Synechocystis*, the rate of CO₂ fixation by the cycle increases to replenish the depleted metabolites (Abramson et al., 2016; Kopka et al., 2017), with little concomitant protein upregulation (Borirak et al., 2015). A quantitative proteomics study found that the levels of central carbon enzymes were relatively stable over a range of growth rates when cells were C_i-limited (Jahn et al., 2018; Zavřel et al., 2019). Further, comparisons of the transcriptomic response of these two cyanobacteria during changes in inorganic C_i suggest that *Synechocystis* responds primarily through biochemical regulation of enzyme fluxes, while *Synechococcus* responds at the transcriptional level (Klähn et al., 2015; Schwarz et al., 2011). Thus, central carbon metabolism in these two strains may be regulated differently, with respect to potential metabolite inhibition or activation of enzymes.

A recent search of bacterial genomes found that the Calvin cycle was present in 6-8% of non-cyanobacterial genomes (Asplund-Samuelsson and Hudson, 2021). Microbes with genomes encoding the Calvin cycle may have a growth advantage in environments poor in organic substrates due to improved cofactor recycling, or in environments with mixed or fluctuating carbon sources (Jahn et al., 2021; McKinlay and Harwood, 2010). Nevertheless, knowledge of Calvin cycle regulation in chemolithoautotrophs is limited. *Cupriavidus necator* and *Hydrogenophaga pseudoflava* are chemolithoautotrophic betaproteobacteria in the order Burkholderiales. *Cupriavidus* acquired the Calvin cycle on a megaplasmid, where genes encoding all cycle enzymes are clustered as an operon under control of the CbbR transcriptional regulator. The *ccb* operon is duplicated on the chromosome (Kusian and Bowien, 1997; Pohlmann et al., 2006). The Calvin cycle of *Hydrogenophaga* is similarly clustered on the chromosome (Grenz et al., 2019; Meyer and Schlegel, 1978). To date, most study on regulation of Calvin cycle activity in chemolithoautotrophs has focused on

transcriptional regulation, where the transcriptional activator of the Calvin cycle operator CbbR has multiple effectors, including pathway intermediates and energy metabolites, that may be species dependent (Bowien and Kusian, 2002; Dangel and Tabita, 2015).

Here, we applied the LiP-SMap technique to uncover new allosteric or competitive interactions among central carbon metabolism in four bacterial strains containing the Calvin cycle, *Synechocystis* sp. PCC 6803, *Synechococcus* PCC 7942, *Cupriavidus necator* (formerly *Ralstonia eutropha*), and *Hydrogenophaga pseudoflava*. We screened metabolites against proteome extracts and found widespread interactions with GAP, ATP, and acetyl-CoA. We validated several interactions *in vitro* and found that the LiP-SMap technique generally reveals interactions that affect catalytic activity, though the effects are often small.

Results

Analysis of proteomics datasets

The LiP-SMap protocol was applied to the four microbes with the general protocol optimized by Piazza et al., with minor modifications (Piazza et al., 2018). *Synechocystis* and *Synechococcus* were cultivated photoautotrophically in an incubator with elevated CO₂ and constant light. *Cupriavidus* was cultivated on formate to induce expression of Calvin cycle genes (Jahn et al., 2021), and *Hydrogenophaga* was grown chemolithoautotrophically on a H₂, CO₂, O₂ gas mixture in sealed serum bottles. Extracted proteomes were first filtered and resuspended in a buffer containing 1 mM MgCl₂. After addition of metabolite, extracts were digested partially by proteinase K, followed by full digestion with a mixture of LysC and trypsin. The resultant peptide mixture was then run on LC-MS (Material and Methods).

We typically detected 8,000-15,000 peptides from the MS runs of bacterial samples (**Figure S1**). As the sensitivity of detecting a protein-metabolite interaction with LiP-SMap is heavily dependent on the number of peptides detected from each protein, a low peptide coverage will result in missing potential interactions. Coverage of Calvin cycle enzymes was generally high, averaging 17 peptides per enzyme (minimum 5, maximum 40), with sequence coverage of approximately 50% (**Figure 1**). To demonstrate the sensitivity of LiP to protein structure, we first tested the effect of added DTT (Dithiothreitol, a reductant) and DTNB (5,5'-dithiobis-2-nitrobenzoic acid, an oxidizing agent) on the extracted proteome of *Synechocystis*. Addition of DTT to 1 mM, a concentration chosen to induce specific redox effects in extracts (Alliegro 2000), resulted in altered peptides from 21 proteins, a small number that indicates that the *Synechocystis* proteome when extracted and filtered is likely in a reduced state. By contrast, addition of DTNB to 50 μ M, a concentration shown to completely inhibit cyanobacteria Prk *in vitro* (Kobayashi et al. 2003), altered peptides from 129 proteins, including Prk and Rubisco (**Figure S2, Dataset S1**). These results indicate that LiP can detect the changes in protein structure mediated by reducing and oxidizing agents, and that the cyanobacteria extracts are in a reduced state. To gauge the immediate reproducibility of the LiP method, we compared the results of adding example metabolites (AcCoA and ATP) to *Cupriavidus* extracts that were prepared from the same cultivation but run in different MS batches. The agreement in significant interacting proteins ($q < 0.01$)

between replicates was several times higher than expected by random chance, though the q value correlation between replicates was not higher than 0.52 and a significant fraction of the interactions were not reproducible (Spearman R; **Figure S3**). These results encapsulate variations in proteome extraction, Proteinase K digestion and trypsin digestion, as well as potential batch effects of different MS runs.

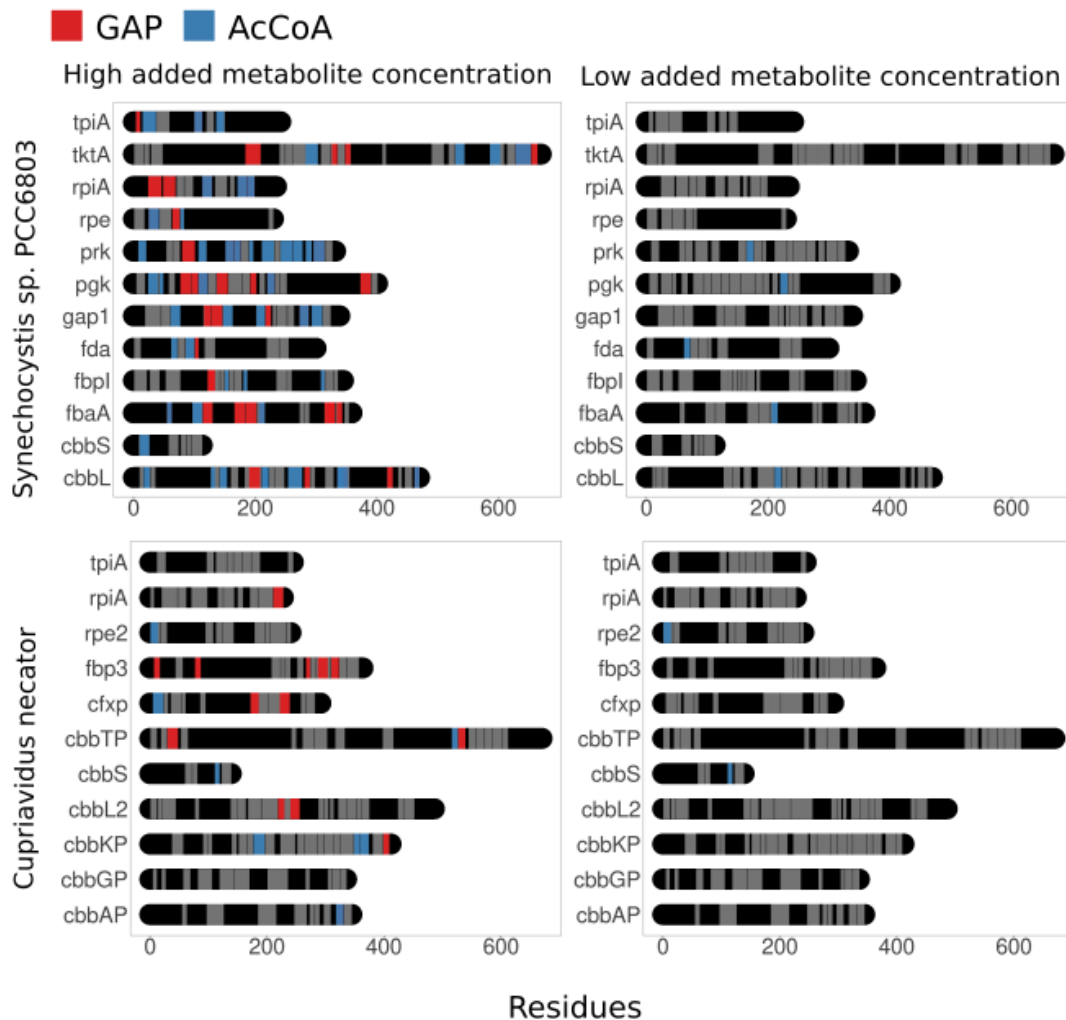


Figure 1. Representative peptide coverage plots showing peptides for Calvin cycle enzymes in *Synechocystis* and *Cupriavidus* from the LiP-SMap method. Peptide coverage of Calvin cycle proteins averaged 50%. Peptides showing a significant change in abundance in presence of added metabolites GAP and AcCoA are highlighted in color, while other detected peptides for each protein are grey. For high concentration tests, 5 mM GAP or 10 mM AcCoA was added. For low concentration tests, 0.5 mM GAP or 1 mM AcCoA was added.

Interactions of selected metabolites with Calvin cycle and surrounding enzymes

We selected 25 metabolites to screen for interactions with cell extracts of *Synechocystis*, *Synechococcus*, *Cupriavidus*, and *Hydrogenophaga*. For each metabolite, we chose two concentrations, typically 1 mM and 10 mM (**Tables S1 and S2**). The two metabolite concentrations were intended to mimic the spikes in metabolite levels that occur during environmental shifts, which may require rapid regulation of enzyme activity (Jaiswal and Wangikar, 2020; Lempp et al., 2019; Mettler et al., 2014; Werner et al., 2019). For each metabolite screen, LiP was performed in quadruplicate, alongside a control (added buffer) on the same MS plate (**Dataset S2**). Not all 25 metabolites were tested in all species (*Synechocystis* 25, *Synechococcus* 21, *Cupriavidus* 23, *Hydrogenophaga* 8). There were many more detected interactions from metabolites added at the high concentrations than at the low concentrations. The majority (typically > 80%) of interactions seen in the low-concentration treatment were also observed in the high concentration treatment, adding confidence to interactions observed from both treatments (**Figure S4**). We did not observe strong dose effects from the added metabolites (**Figure S5**). The \log_2FC of affected peptides when treated with the low metabolite concentration was similar to the \log_2FC seen when a high metabolite concentration was used, though ATP and GTP interactions were exceptions. This general insensitivity to concentration could indicate that most metabolite-protein binding events are already saturated at the low concentration (typically 1 mM). As expected, proteins that had more total mapped peptides also showed more metabolite interactions, across all tested metabolites and strains (**Figure S6**).

We extracted a list of all proteins affected by any metabolite for each strain and grouped them according to KEGG orthology groups (KOGs), including only orthology groups present in all four strains (**Figure S7; Dataset S3**). For the high metabolite concentrations, the PCA clustering analysis interactions showed that some metabolite-KOG interactions clustered together for all strains, as exemplified by citrate and AMP, which may indicate common mechanisms of action (**Figure 2**). For GAP, a metabolite with 150+ interactions in all four strains, the photoautotrophs clustered apart from the chemolithoautotrophs, suggesting that GAP-based regulation may be specific for a certain bacteria lifestyle. Other trends may indicate the presence of different metabolic capabilities. For example, G6P and KDPG, intermediates in glycolysis, showed significantly more interactions in *Cupriavidus* than in the photoautotrophs (KDPG was not tested in *Hydrogenophaga*). However, we note that the discrimination axes are relatively weak; with PC1 41% and PC2 7%. For the low metabolite concentrations, the number of interactions was significantly fewer, and the separation between strains was significantly weaker (**Figure S8**).

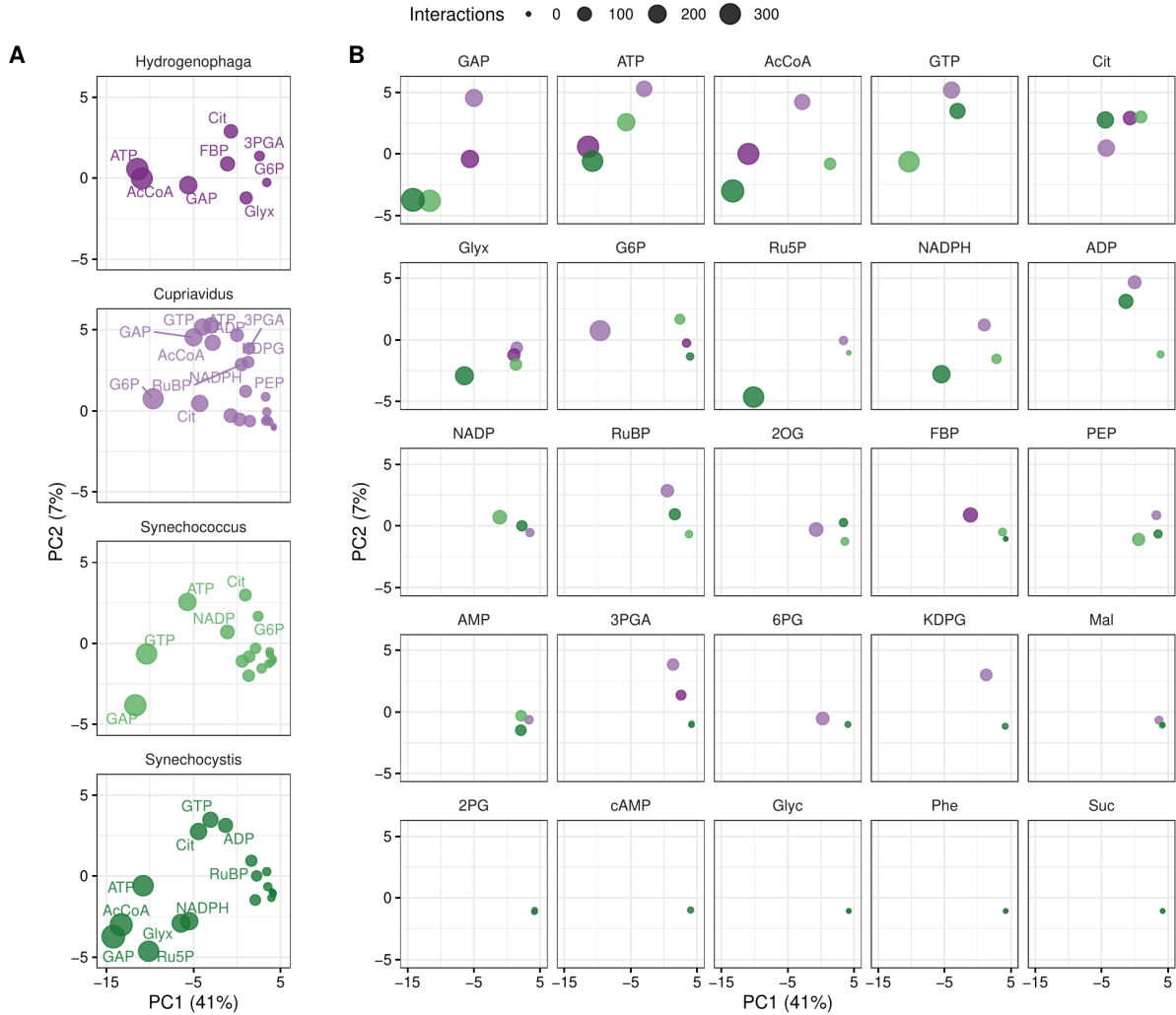


Figure 2. Similarity of ortholog interaction patterns, high added metabolite concentration. Principal components were calculated from the presence or absence of interaction with each of 477 orthologs (see Materials and Methods). All data points shown here are from the same principal component analysis, but split per organism (A) or metabolite (B) to reduce overplotting. Percentages indicate the fraction of the total variance captured by the principal components.

We next examined interactions of metabolites with enzymes in the Calvin cycle, as well as enzymes in the major pathways that siphon carbon out of the cycle (Figure 3, high concentrations; **Figure S9**, low concentrations). Calvin cycle enzymes in these four microbes are phylogenetically diverse, though the cyanobacteria enzymes are more closely related to each other than to the chemolithoautotroph orthologs (**Figure S10**). Common LiP-SMap interactions among all four microbes could indicate evolutionary conservation important to the Calvin cycle. Interactions with ATP and GAP were widespread in all four microbes, and AcCoA interactions were prominent in all strains, though less so in *Synechococcus*. AcCoA is a predicted cofactor for lysine post-translational acetylation *in vivo*, mediated by acyltransferases, but has also been shown to acylate lysines non-enzymatically *in vitro* (Wagner and Payne, 2013). GAP has not previously been shown to be a cofactor for protein acylation, but glyceraldehyde has been shown to form Schiff

adducts with lysine residues *in vitro* (Acharya and Manning, 1980; Acharya and Sussman, 1983). We therefore compared the AcCoA- and GAP-sensitive proteins that we detected in *Synechocystis* with published datasets for the *Synechocystis* acetylome and propionylome (Mo et al., 2015; Yang et al., 2019). Compared to proteins affected by other metabolites, the proteins detected as AcCoA-sensitive in LiP-SMap were more likely to include proteins that were acetylated in the reference literature (75% of 355 acetylated proteins at high AcCoA treatment) and the proteins detected as GAP-sensitive in LiP-SMap were more likely to include proteins that were propionylated in the reference literature (87% of 65 propionylated at high GAP treatment; **Figure S11**). LiP-SMap may therefore be detecting acylation that occurs during AcCoA or GAP treatment of cell extracts. ATP also showed many interactions and may act via a general mechanism. In addition to its role in metabolic reactions, ATP may cause secondary interactions due to its Mg^{2+} chelating effect ($\log_{10}K = 4.1$ for ATP binding Mg^{2+} (Pecoraro et al., 1984)). The number of ATP interactions in *Synechocystis* extracts was negatively correlated with $MgCl_2$ concentration in the LiP buffer (**Figure S12**). ATP treatment caused changes in many ribosome-derived peptides, indicating structural changes in the ribosome; a similar result was reported from LiP-SMap of ATP-treated *E. coli* extracts (Piazza et al., 2018). A recent TPP study of *E. coli* extracts treated with different ATP concentrations found that at low ATP levels ($<500 \mu M$), ATP interacts mostly with enzymes that use it as substrate or effector, but at higher concentrations ATP affects many protein-protein interactions (Sridharan et al., 2019). Some metabolite interactions were nearly exclusive to the photoautotrophs. For example, glyoxylate, a photorespiratory intermediate, showed extensive interactions in *Synechocystis*, even at low concentrations, and some “sink” reactions such as glucose-phosphate mutase (GPM) and ADP-glucose pyrophosphorylase (AGPase), steps in glycogen synthesis, had significantly more interactions in *Synechocystis* and *Synechococcus*. *Cupriavidus* enzymes were particularly sensitive to added phospho-sugars, such as KDPG, RuBP, and G6P. 3-Deoxy-D-arabinoheptulosonate 7-phosphate synthase (DAHPS), an enzyme that reacts with E4P in the shikimate synthesis pathway, showed interactions with several metabolites primarily in *Cupriavidus*, at both high and low concentrations. In summary, while there were some interactions observed in all strains, primarily GAP, AcCoA, and ATP, most metabolites showed species specific interactions.

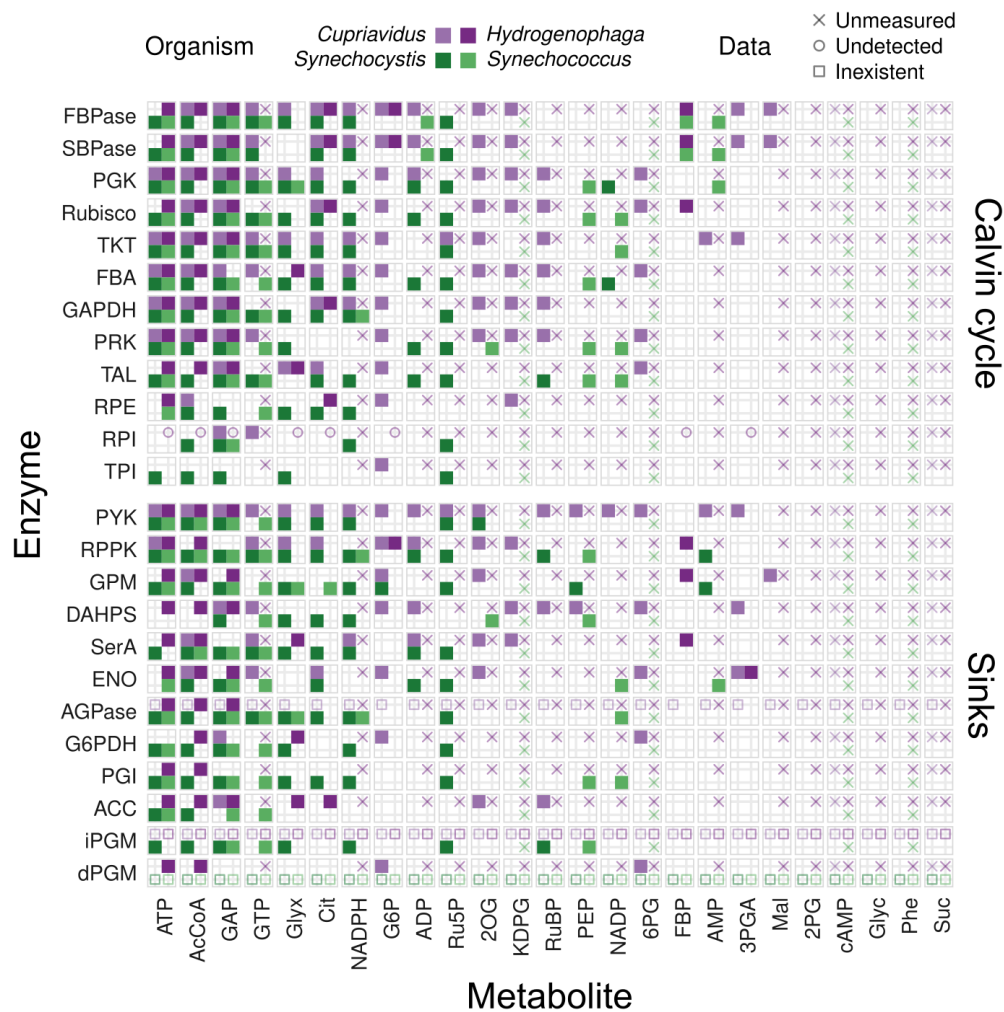


Figure 3. Interactions of Calvin cycle enzymes and selected central carbon metabolism enzymes with metabolites, high added metabolite concentration.

Interactions between metabolites (columns) at high concentration and enzymes (rows) identified by KEGG EC number annotation are shown for each organism by tiles filled with the corresponding color. A blank tile indicates that the interaction was not detected, while missing protein data is explained by a symbol. A cross indicates that the particular condition was not measured, a circle indicates that no proteins were detected, and a square indicates that there was no such enzyme in the corresponding genome. AGPase, ADP-glucose synthase (EC 2.7.7.27); DAHPS, 3-Deoxy-D-arabinoheptulosonate 7-phosphate synthase (EC 2.5.1.54); dPGM, 2,3-diphosphoglycerate-dependent phosphoglycerate mutase (EC 5.4.2.11); ENO, Enolase (EC 4.2.1.11); FBA, Fructose-bisphosphate aldolase (EC 4.1.2.13); FBPase, Fructose-1,6-bisphosphatase (EC 3.1.3.11); G6PDH, Zwf (EC 1.1.1.49); GAPDH, Glyceraldehyde 3-phosphate dehydrogenase (EC 1.2.1.12, 1.2.1.13, 1.2.1.59); GPM, Phosphoglucumutase (EC 5.4.2.2); iPGM, 2,3-diphosphoglycerate-independent phosphoglycerate mutase (EC 5.4.2.12); PGI, Phosphoglucosomerase (EC 5.3.1.9); PGK, Phosphoglycerate kinase (EC 2.7.2.3); PRK, Phosphoribulokinase (EC 2.7.1.19); PYK, Pyruvate kinase (EC 2.7.1.40); RPE, Ribulose-phosphate 3-epimerase (EC 5.1.3.1); RPI, Ribose 5-phosphate isomerase (EC 5.3.1.6); RPPK, Ribose-5-phosphate pyrophosphokinase (EC 2.7.6.1); Rubisco, Ribulose-bisphosphate carboxylase (EC 4.1.1.39); SBPase, Sedoheptulose-1,7-bisphosphatase (EC 3.1.3.37); SerA, Phosphoglycerate dehydrogenase (EC 1.1.1.95); TAL, Transaldolase (EC 2.2.1.2); TKT,

Transketolase (EC 2.2.1.1); TPI, Triose-phosphate isomerase (EC 5.3.1.1). Similar plot for low metabolite concentrations in **Figure S9**.

Validation of metabolite interactions and effect on enzyme activity

An interaction of an enzyme with a metabolite as revealed by LiP-SMap does not necessarily mean that the metabolite interacts directly, or that catalytic activity is affected. To explore whether LiP-SMap hits to enzymes tended to affect catalytic activity, we purified and screened F/SBPase and transketolase from *Synechocystis* (syn-F/SBPase *fbpI*, syn-TKT *tktA*) and *Cupriavidus* (cn-F/SBPase *cbbFp*, cn-TKT *cbbTp*). F/SBPase is a target for altering Calvin cycle flux in cyanobacteria as it has been predicted by metabolic modeling to have some control over the overall rate of CO₂ fixation (Janasch et al., 2019; Pettersson and Ryde-Pettersson, 1989a) and overexpression of F/SBPase has been shown to have a positive effect on autotrophic growth (De Porcellinis et al., 2018; Liang and Lindblad, 2016; Yu King Hing et al., 2019). F/SBPase activity is also important for other industrial microbes. In methylotrophic bacteria, the regeneration arm of the RuMP pathway requires a F/SBPase enzyme (Stolzenberger et al., 2013), and overexpression of the *E. coli* F/SBPase *glpX* increased methanol assimilation in an *E. coli* strain engineered to contain the RuMP pathway (Woolston et al., 2018). Transketolase catalyses the transfer of a two-carbon ketol group to an aldehyde and has a central role in both the Calvin cycle and the pentose phosphate pathway. The transketolase of *E. coli* has been studied extensively, and has been shown to form a dimer and exhibit considerable cooperativity between monomers (Wilkinson and Dalby, 2020). The transketolases of *Synechocystis* and *Cupriavidus* have not been characterized previously.

Five of the LiP-SMap detected metabolites for syn-F/SBPase and cn-F/SBPase were screened for their effects on kinetics by *in vitro* assays, as well as for direct binding by thermal shift assay (melting temperature determination; **Table 1**, **Table S3**). The previously known allosteric inhibitor AMP was also included although AMP did not show a LiP interaction in either enzyme. Due to the strong impact that AMP effector has on syn-F/SBPase activity (IC₅₀ value of 34 µM (Feng et al., 2014a)), even residual amounts of AMP effector present in the lysate samples after proteome washing may impact the protein's conformation and thus mask it from additional conformational change upon incubation with externally added AMP. This notion is supported by the observation that AMP did show interaction with the *Synechococcus* PCC 7942 F/SBPase, for which the AMP inhibitory effect is reported to be weaker (Cotton et al., 2015; Tamoi et al., 1998). In accordance with the literature, addition of 0.25 mM AMP completely inhibited syn-F/SBPase activity (the effect on cn-F/SBPase was not measured) and increased the thermal stability of both enzymes, indicating a direct conformational change induced by the metabolite (**Figure S13**). Addition of 0.5 mM GAP stimulated syn-F/SBPase and cn-F/SBPase activity by reducing the *K_M*-value, **Figure 4**). GAP also caused a thermal shift of the syn-F/SBPase enzyme at multiple Mg²⁺ concentrations, indicating that the LiP and kinetic effect is caused by a direct conformational change mediated by GAP, and that the effect is likely not due to sequestration of the required Mg²⁺ cofactor from the enzyme (**Figure S14**). In contrast, no thermal shift was observed upon adding GAP to cn-F/SBPase. Addition of 3 mM NADPH reduced the maximum turnover rate of both syn-F/SBPase and cn-F/SBPase, but inhibition

was not significant at substrate concentrations below K_M . The thermal stability increased slightly for both enzymes upon NADPH addition, again indicating a conformational change mediated directly by an interaction with the metabolite (change in $T_m = 1-2\text{ }^{\circ}\text{C}$, **Figure S15**). The similar kinetic effects observed for NADPH, GAP and AMP suggest evolutionary conservation, as syn-F/SBPase (class II) and cn-F/SBPase (class I) have similar folds but little sequence similarity (Brown et al., 2009; Feng et al., 2014a).

Addition of AcCoA did not significantly alter the kinetics of syn-F/SBPase (**Figure 4**), though the interaction was detected by the LiP assay. Added AcCoA induced a small but statistically significant change in T_m . However, the melting temperature shift may be due to the Li^+ counterion in the AcCoA salt used in that assay, which may displace the Mg^{2+} cofactor in the enzyme active site (Ganapathy et al., 2015). We confirmed Li^+ sensitivity of syn-F/SBPase, and saw that the T_m effect of the added Li-AcCoA was indeed dependent on Mg^{2+} concentration. The T_m increased at high Mg^{2+} concentration and decreased at lower Mg^{2+} concentration, potentially due to a mixed effect of Li^+ interaction and Mg^{2+} chelation by AcCoA (Maloney and Dennis, 1977; Martell and Smith, 2013). Finally, addition of the LiP-altering metabolite citrate at 5 mM increased the K_M -value of syn-F/SBPase, which is consistent with the reported sensitivity of *Mycobacterium* F/SBPase to citrate, and the presence of citrate in the crystal structure of *Mycobacterium* F/SBPase (Wolf et al., 2018). However, thermal shift assays indicated that the inhibitory effect of citrate was likely due to chelation of Mg^{2+} from the active site of F/SBPase (**Figure S16**), as described above for Li-AcCoA. The affinity of citrate for Mg^{2+} reported in literature is considerably higher than that of the other effectors ($\log_{10}K$ for Mg^{2+} binding: citrate 3.4, AcCoA 2.9, NADPH 2.6, GAP 1.8 (Maloney and Dennis, 1977; Martell and Smith, 2013)). Chelation of Mg^{2+} ions is likely to have wide-spread effects throughout metabolism since many enzymes require on Mg^{2+} for structural integrity as well as cofactor for catalysis.

In summary, the F/SBPase LiP results were often translated into altered T_m or altered kinetics, for two F/SBPases with dissimilar sequences.

Table 1: Validation of LiP-sensitive metabolites for effect on F/SBPase

Effector (mM)	Interaction in LiP	Kinetic effect	Effect on T_m
<i>Synechocystis fbp1</i>			
GAP (0.5)	Yes	$-K_m$	+
NADPH (3)	Yes	$-K_{cat}$	n.t.
Citrate (5)	Yes	$+K_m$	-*
AcCoA (2)	Yes	n.c.	n.c.**
AMP (0.25)	No	***	+
<i>Curpriavidus fbp3</i>			
GAP (0.5)	Yes	$-K_m$	n.c.
NADPH (3)	Yes	$-k_{cat} -K_m$	+****
AMP	No	n.t.	+

n.t. = Not tested; n.c. = No significant change,

* Mg^{2+} chelation

** Lithium AcCoA salt was used, Mg^{2+} -correlated effect

*** No activity detected

**** T_m change 1-2 $^{\circ}\text{C}$

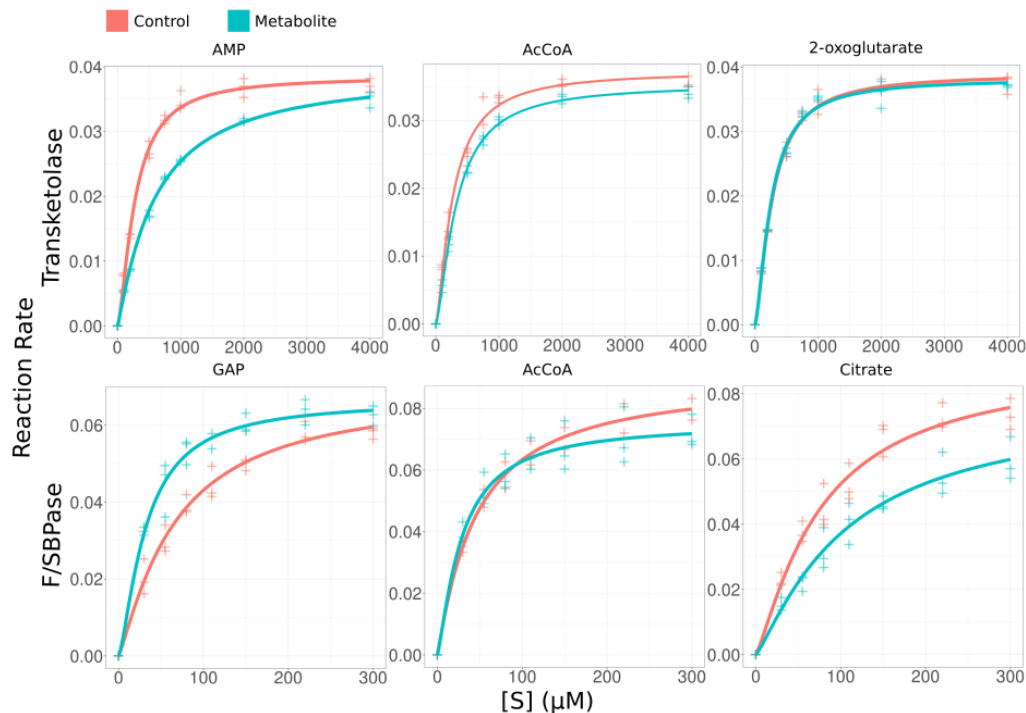


Figure 4. Kinetic effect of selected effector metabolites on *Synechocystis* TKT and F/SBPase kinetics. For transketolase assays, the varied substrate was R5P, with Erythrulose in excess. For F/SBPase assays, the varied substrate was FBP. For experimental details, see Materials and Methods. Y-axis unit is absorbance per minute. The F/SBPase assay y-axis unit is $\mu\text{M/s}$. Kinetic plots for all added metabolites in **Figures S17-S19**.

Besides showing an interaction on the general protein level, the LiP data indicated that GAP and NADPH cause conformational changes in syn F/SBPase at sites that are distal to the AMP allosteric site (**Figure 5**). To test whether the GAP activation and NADPH inhibition mechanisms are distinct from the AMP allostery, we created a single residue exchange variant of syn-F/SBPase (R194H) at a position that is located at the enzyme surface in a β -sheet connecting the substrate binding site to the AMP-binding site and that was not included in any of the metabolite LiP-hits for this enzyme. This mutant lost AMP sensitivity, but retained sensitivity to both GAP activation and NADPH inhibition (**Figure S20**).

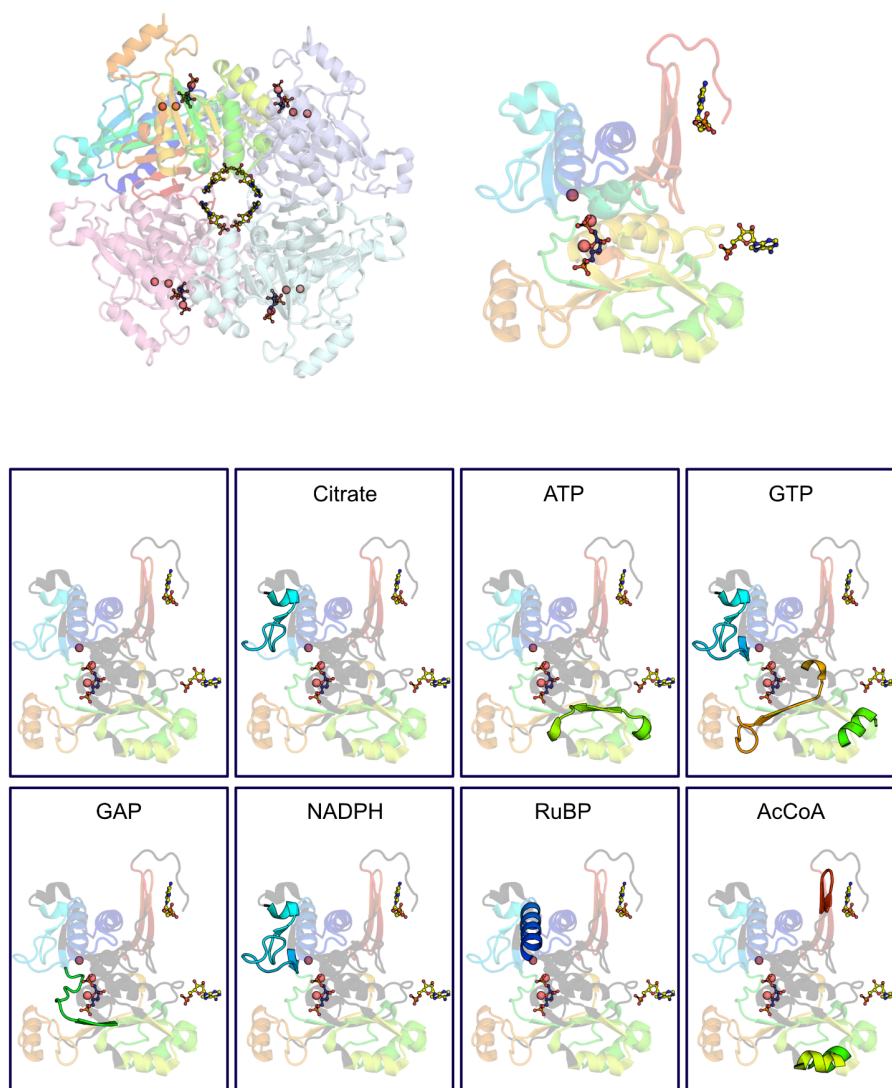


Figure 5. Structure of *Synechocystis* F/SBPase showing peptide coverage and affected peptides from LiP-SMap. Top left: F/SBPase assembles as a homotetramer (PDB-ID: 3RPL (Feng et al., 2014a)). The substrate FBP (shown as blue sticks) is coordinated by active site residues as well as Mg^{2+} ions (red spheres), and AMP allosteric inhibitor molecules at the central interface of the tetramer are shown as yellow sticks. Top right: monomeric view colored according to different structural elements, showing interaction with FBP and the AMP-molecules at two adjacent interfaces with other monomers. Bottom: Monomeric view as shown in top right panel with peptides that were not detected in any condition shown as dark-gray ribbon. Peptides affected by the indicated metabolites (high added concentration) are outlined as opaque ribbon in individual panels;

The transketolases from *Synechocystis* and *Cupriavidus* were screened *in vitro* against all metabolites that showed a LiP interaction with the enzyme in any of the four species (**Table 2**). The most prominent effect was AMP, which significantly reduced activity of both syn-TKT and cn-TKT enzymes. While ATP and ADP inhibition of transketolases have been shown

(Markert et al., 2014), inhibition by AMP has not been reported. Many of the other LiP-sensitive metabolites had small but statistically significant effects on kinetic parameters (**Figure 4, Supplementary Table 4**). However, only a single metabolite (G6P) affected the T_m of either transketolase. Taking together data from the two transketolases, we found that of twelve metabolites showing interaction in LiP, six had an effect on enzyme kinetics in the *in vitro* assay, and of eight metabolites not showing interaction in LiP, four had an effect on kinetics in the *in vitro* assay.

Table 2: Validation of metabolites for transketolase

Effector (1 mM)	Interaction in LiP	Kinetic effect	Interaction in LiP	Kinetic effect
	<i>Synechocystis tktA</i>		<i>Cupriavidus cbbTP</i>	
2OG	No	n.c.	Yes	- K_m
2PG	No	n.c.	Yes	n.c.
3PGA	No	n.c.	n.t.	n.t.
AcCoA	Yes	n.c.	n.t.	n.t.
AMP	No	+ K_m	Yes	+ K_m
ATP	Yes	- k_{cat}	Yes	n.c.
Citrate	Yes	- k_{cat}	Yes	n.c.
DHAP	n.t.	n.t.	n.t.	+ K_m
G6P	No	n.c.	Yes	n.c.
Glyoxylate	Yes	+ K_m	Yes	- k_{cat}
GTP	Yes	n.c.	Yes	n.t.
Malate	No	n.t.	No	n.c.
KDPG	No	+ K_m	n.t.	n.t.
NADP	No	n.c.	No	+ K_m
RuBP	No	+ K_m , - k_{cat}	n.t.	n.t.

n.t. = Not tested; n.c. = No significant change

Predicted effects of enzyme-metabolite interactions on stability and flux control in *Synechocystis*

To evaluate the effect of regulatory interactions on flux control, they must be viewed in the context of the metabolic network. The regulations identified and assayed for syn-F/SBPase and syn-TKT were incorporated into a kinetic model of the central metabolism of *Synechocystis*. As a basis, the kinetic model structure for the Calvin cycle in *Synechocystis* from a previous study (Janasch et al., 2019) was expanded to cover adjacent parts of metabolism including the regulatory metabolites (**Figure 6A**). Four model variants were designed: two models with LiP-SMap regulatory interactions added to the F/SBPase reaction or TKT1/2 reactions (models “F/SBPase” and “TKT” respectively), one model with regulations on both enzymes simultaneously (model “Both”), and one model with none of the newly discovered interactions added (model “Base”). For the analysis of the dynamics of the metabolic states, *i.e.* stability and distribution of flux control, and the influence of the added regulations, an ensemble modelling approach was employed. In brief, steady-state flux through each reaction was calculated and concentrations for each metabolite were randomly sampled, cumulatively defining the metabolic state of the system. Then, sets of kinetic

parameters (V_{\max} , K_i , K_m) for each reaction were randomly sampled so that the steady-state flux was achieved, allowing the evaluation of the dynamics of the model around the steady-state. Repeating the metabolite and parameter sampling resulted in an ensemble of kinetic models and consequently a probabilistic overview of the dynamics. The resulting concentrations from the metabolite sampling are shown in **Figure S21**.

As a first analysis step, the stability associated with metabolite concentrations was compared for the four model variants. Here, stability refers to the ability of the system to return to its metabolic state upon an infinitesimal small perturbation of the metabolite concentrations. All model variants were less stable than the original model of the Calvin cycle. Generated parameter sets in the “Base” model had a median stability of 38% over all metabolomes (min 11%, max 58%), compared to 67% for the original Calvin cycle model (min 25%, max 93% (Janasch et al., 2019)). The lower stability was not surprising as expanding the system out from the intrinsically stable Calvin cycle provides more potential for components to influence stability. The addition of regulation on F/SBPase increased stability slightly (model “F/SBPase” median: 40%, min: 11%, max: 60%), while addition of regulation to TKT1/2 reduced stability strongly (model “TKT” median: 26%, min: 0.6%, max: 46.5%). When adding regulations to both enzymes, interactions on F/SBPase slightly compensated for the decreased stability caused by regulation on TKT1/2, but the latter dominated the trend (model “Both” median: 26%, min: 0.4%, max: 48%). This observed reduction in stability upon additional biochemical regulation is contradictory to previous findings (Grimbs et al., 2007; Murabito et al., 2014), but has been reported before for Calvin cycle regulation in chloroplasts (Pettersson and Ryde-Pettersson, 1989b).

The sampling of thermodynamically feasible metabolomes and the subsequent analysis of the dynamics around the steady-state allows for the association of metabolite concentrations with trends in stability. In **Figure 6 B** concentrations associated with most or fewest stable states for each model variant are shown (see **Figure S22** for all metabolites). The width of the distributions resembles the thermodynamically feasible concentration range for the corresponding metabolites. Higher concentrations of the Rubisco-substrate RuBP are linked to instability in all four current variants, albeit less pronounced than in the original analysis of the isolated Calvin cycle. An association with instability was also found for high concentrations of S7P, while the two products of the TKT2 reaction R5P and X5P showed instability for low concentrations. Low concentrations of E4P and S17P tended towards stability. The metabolite distributions and their stability association have to be interpreted with care, as the results are of rather exploratory nature due to the broad concentration ranges (Asplund-Samuelsson et al., 2018), and describe the dynamic behavior of the system at the individual concentrations.

The trends in the distributions for more or fewer stable states were generally similar between all model variants, though the TKT regulation did have an effect. Significant differences between the distributions leading to most stable parameter sets between the “Base” model and the “TKT” and “Both” variants were verified by statistical testing (Kolmogorov-Smirnov test, $p < 0.05$, **Figure S23**). For the “TKT” and “Both” model variants, the distributions for metabolite concentrations associated with stability and instability became more similar for RuBP and E4P, indicating that the effect of these metabolites on system stability are reduced. In contrast, the distributions became more separated for R5P and X5P, indicating that these metabolites have an increased influence over system stability when regulation to

TKT is added to the model. Surprisingly, the concentrations of the regulators GAP and AMP, identified by LiP-Smap and verified by kinetic assay, did not appear to affect stability in any model.

Fully parameterized kinetic models enable the quantification of flux control using metabolic control analysis (MCA), resulting in flux control coefficients (FCCs) for each reaction (**Figure 6C**, **Figure S24** for all FCCs). Generally, the supply of ATP and NADPH via the light reactions (lumped as reactions ATPSyn and NADPase, respectively), and phosphate showed a positive effect on most fluxes, emphasizing their importance on autotrophic metabolism. Furthermore, PRK, the enzyme producing the Rubisco-substrate RuBP, had a positive influence on many reactions, while Rubisco showed positive flux control only over reactions downstream of the Calvin cycle towards the TCA cycle. Flux control for an enzyme was often local, only over other enzymes in the pathway or subnetwork, such as within reactions of the photorespiration (RubisO, PGP, GLCO) and the phosphoketolase shunt reactions (XFPK1/2, PTA) which influenced mainly each other (**Supplementary Figure 24**).

ALD and FBPase were among the most affected reactions, as their steady-state fluxes were set relatively low based on fluxomics analyses (Gopalakrishnan et al., 2018), causing relatively large FCCs even upon small perturbations as the FCC quantification is based on relative changes. Studies overexpressing Calvin cycle enzymes showed positive effects on growth rate for TKT, F/SBPase and FBA/ALD (Liang and Lindblad, 2016), which was partly represented in the trends of the FCCs, for example by SBPase exerting positive flux control over many reactions. Comparing the trends in flux control between the four models revealed generally similar behavior between them, with the F/SBPase variant showing some distinctions. The additional regulation on F/SBPase increased the magnitude of FCCs in many cases, for example the positive control of ATPSyn over many reactions.

Discussion

In this study we were interested primarily in using LiP-SMap to reveal new metabolite-level regulation of enzymes within the Calvin cycle and central carbon metabolism. Previously, inference of allosteric interaction in microbial metabolism has been done through analysis of time-resolved metabolite and proteomics datasets (Lempp et al., 2019; Link et al., 2013), fitting of multi-omics steady-state data (Hackett et al., 2016; Nishiguchi et al., 2020), or through co-elution of proteins and metabolites from a chromatography column (Li et al., 2010; Veyel et al., 2018). By quantification of individual peptides, the LiP-SMap method can provide insight into the binding mode of metabolites to a protein, which is an extra level of information compared to inference methods. However, there are some limitations of the method compared to other interaction proteomics. The peptide coverage in our data is only moderate. The coverage achieved is the result of a tradeoff between the quantity of screened samples and the sample preparation and analysis time. For example, it is possible to increase protein coverage by chromatographic fractionation of peptide mixtures, though this will considerably increase the required mass spectrometry resources. Quantification of the effect of added metabolite over a broader concentration range can also increase confidence in a particular interaction (Piazza et al., 2020). It is also possible that we will miss metabolite-protein interactions that are relevant for growth conditions other than photoautotrophy. It has been shown by complementary proteomics methods that widespread formation of protein complexes occur in cyanobacteria cultivated in the dark (Guerreiro et al., 2016; Pattanayak GK, Liao Y, Wallace EWJ, Budnik B, Drummond DA, Rust MJ, 2020). The LiP method could potentially also detect changes in protein complexation, as well as protein susceptibility to metabolite interactions.

Our results also show validation of LiP-Smap interactions with multiple methods are needed to deduce mechanism. Based on LiP-SMap, kinetic assays, and melting temperature analysis performed at higher MgCl_2 concentrations, we propose that most observed LiP interactions with citrate and ATP are due to Mg^{2+} chelation. The widespread interactions of AcCoA and GAP may be due to acetylation or propionylation occurring in the LiP mixture, where potential acylases are present, based on overlap between the interacting proteins and these PTMs mapped in *Synechocystis*. The cofactor for such propionylation in bacteria is presumed to be propionyl-CoA, not aldehydes (Sun et al., 2016). However, it has been shown that Schiff-base adducts between primary amines and glyceraldehyde can form non-enzymatically *in vitro*, at similar conditions used in our LiP and F/SBPase kinetic assays (Acharya and Manning, 1980), though stable formation of Schiff bases between aldehydes and lysine residues appears to require a reducing compound such as borohydride that was not present in our assay, although DTT was added (Natsch et al., 2012). Additionally, a lysine nearby to the GAP-affected peptide of *fbpI* (K156) was recently shown to be propionylated *in vivo* in *Synechocystis*, and the mutant enzyme K156R, presumably insensitive to propionylation showed reduced catalytic activity (Yang et al., 2019). We did not test if F/SBPase becomes propionylated by GAP in our *in vitro* assay. Further study on the mechanism of the GAP activation of F/SBPase is thus warranted.

The potential for secondary effects through catalytic conversion of an added metabolite during Lip-SMap is likely low. Since the proteome is filtered before treatment with a metabolite, the required cofactors for most eventual catalytic reactions are missing.

However, for reactions not requiring a cofactor, conversion of the metabolite could occur. We estimate that most central carbon metabolism enzymes would be present at similar concentrations as used for *in vitro* assays, so that metabolite conversion could occur if cofactors are not needed. For example *syn*-TKT was used at 3 $\mu\text{g/mL}$ in the *in-vitro* assays, where 0.25 mM of substrate was converted after 8 minutes. *Syn*-TKT is present in the LiP mixture at 5-10 $\mu\text{g/mL}$, estimated from its reported fraction of the total cyanobacteria proteome (Jahn et al., 2018).

The discovery of potential regulatory interactions with methods such as LiP-SMap has potential to enhance predictions of metabolic models. Biochemical regulations are important for capturing dynamic behavior, and integration of new regulation has helped to explain growth behavior and flux control in well studied organisms such as *E. coli* (Christodoulou et al., 2019; Millard et al., 2021). Integrating the regulations identified in the present study into the steady-state kinetic model revealed only a limited effect on flux control, which could be attributed to the nature of the model, as it models slight perturbations around a steady state. The controlling effect of such biochemical regulations is probably relevant during adaptation for changing environments, which is difficult to cover with a single physiological steady-state. Nonetheless, testing the effect of the regulatory interactions on F/SBPase and TKT revealed a reduction of overall stability when regulation was added to TKT. While metabolic feedback regulation has generally been linked to increased stability as shown computationally (Grimbs et al., 2007; Murabito et al., 2014) and experimentally (Christodoulou et al., 2019; Sander et al., 2019) in some metabolic systems, a computational study considering the effect of competitive inhibition on Calvin cycle enzymes showed contradictory results. In their work, Pettersson and Ryde-Pettersson (Pettersson and Ryde-Pettersson, 1989b) found these inhibitions to exert insignificant flux control and to reduce stability of the Calvin cycle. Here, the reduction in stability caused by the TKT regulation could point towards more narrow metabolite distributions necessary for other metabolic functions outside of the modelled network.

The modeling results reported here come with some important caveats. The lack of exact data describing the metabolic state required the computational sampling of metabolite concentrations, which albeit thermodynamically feasible, were broadly distributed and thereby covered potentially unphysiological values. While dynamic metabolite data in cyanobacteria were reported for shifting environments such as light/dark (Werner et al., 2019) or changes in production capability (Kopka et al., 2017), steady-state metabolomics data in combination with other physiological parameters, such as protein expression and abundance, would reveal the extent of regulatory interactions and potential other compensatory mechanisms (Gerosa et al., 2015; Hackett et al., 2016). The sparse availability of actual kinetic enzyme data, beyond F/SBPase and TKT, is another challenging aspect. Reproducing the *in-vivo* environment of an enzyme, including all known and potentially unknown cofactors and modifications, for *in vitro* measurements is challenging. The parameterization approach employed here, *e.g.* sampling of the saturation states of the individual enzymes' active sites, finds values describing the steady-state fluxes, but could result in unrealistically low or high values when combined. Additional physiological data, such as absolute protein abundances or metabolite concentrations, would constrain the allowable ranges of the kinetic parameters and thereby reduce the sampling space closer to the *in vivo* values (Saa and Nielsen, 2016).

The extent of metabolite-protein interactions at low added metabolite concentrations (0.5 -1 mM) was significantly less than at high concentrations (5-10 mM). This suggests that metabolite control of enzyme activity is probably not prevalent at steady state metabolite concentrations, which are likely lower than 1 mM, but rather becomes relevant when metabolite levels fluctuate or spike. The inhibition of F/SBPase by AMP has been reported previously, though its role in Calvin cycle regulation is not clear. AMP levels have been shown to increase above $K_{i,AMP}$ during the first 30 minutes of carbon limitation, which would be expected to inactivate FBPase and the Calvin cycle (Selim et al., 2018).

Post-translational inactivation of F/SBPase could facilitate a rapid downregulation of the Calvin cycle in the early response to carbon limitation, and enable the mobilization of glycogen via the pentose phosphate pathway towards TCA cycle intermediates.

Replenishment of TCA cycle intermediates is important for sustained amino acid synthesis, and to balance nitrogen uptake through elevated 2-oxoglutarate levels (Eisenhut et al., 2008). The increase in K_m of F/SBPase in presence of NADPH would reduce the enzyme activity response to accumulated FBP levels, which may be beneficial under conditions when NADPH is high, e.g. during nitrogen limitation when Calvin cycle flux is downregulated and F6P is used for glycogen synthesis rather than regeneration of RuBP. It is possible that NADPH inhibition also affects the kinetics for SBP dephosphorylation, which could be relevant for redirecting and regulating carbon flux towards glycogen during nutrient stress.

Activation of F/SBPase by GAP has not been reported previously. Such feed-forward activation may work to prevent GAP accumulation and increase Calvin cycle activity under CO_2 replete conditions, conceptually similar to feed forward activation of pyruvate kinase by fructose bisphosphate in *E. coli* and red blood cells (Kochanowski et al., 2013; Schuster and Holzhütter, 1995). To date there has been little experimental exploration of metabolite-mediated feedback or feedforward regulation on the Calvin cycle. It was recently shown that photorespiratory metabolite 2PG acts as a feedback inhibitor of the Calvin cycle in *Arabidopsis thaliana* by inhibiting TIM and SBPase at sub-millimolar concentrations.

Crucially, this was found to be metabolically relevant, as a forced increase of 2PG by graded anti-sense regulation of 2-phosphoglycolate phosphatase (PGLP1) reduced photosynthetic yield, CO_2 fixation, and plant growth, while an overexpression of PGLP1 increased growth (Flügel et al., 2017). In the context of such works, LiP-SMap will aid in finding new regulators.

Materials and methods

Cultivations and harvest

Cupriavidus necator strain DSMZ 428 was grown in Ralstonia Minimal Media (RMM) with 100 mM HEPES pH 7.5 under chemostat conditions in a Photon Systems Instruments Multi-Cultivator MC-1000 OD. Each reactor tube was set up to a volume of 55 mL, OD₆₀₀ 0.05 and 3.5 g/L fructose. Once growth ceased, an inlet feed of 0.01 - 0.05 mL/min of 8 g/L formic acid in RMM with 100 mM HEPES pH 7.5 was initiated. Cultivations were kept running until a stable OD₆₀₀ had been observed for at least 5 doubling times.

Hydrogenophaga pseudoflava strain DSMZ 1084 were grown at 30 °C and 200 RPM in sealed flasks of ~135 mL containing ~25 mL DSMZ media 133 and ~110 mL of gas (70% H₂, 15% CO₂ and 15% O₂) at 1 bar overpressure. Cultivations were started from overnight cultures on 1.5 g/L acetate and harvested during exponential growth at OD₆₀₀ ~1.0.

Synechocystis sp. PCC6803 (gift from Klaas Hellingwerf, University Amsterdam) & *Synechococcus elongates* PCC7942 (from Pasteur Culture Collection, France) were grown in BG-11 media at 1% CO₂ and a light intensity of ~70 μmol·s⁻¹·m⁻² in 500 mL flasks containing 100 mL liquid until an OD₇₃₀ of ~1.0.

For each microbe, four biological replicate cultivations were performed, and immediately before harvest the replicates were pooled. Cells were harvested by centrifugation and washed three times with cold lysis buffer before being resuspended in a small amount of lysis buffer, snap frozen in liquid nitrogen, and stored as aliquots in -80 °C. The cyanobacteria were exposed to light at ~ 400 μmol·s⁻¹·m⁻² for 5 minutes prior to snap freezing.

Proteome extraction

Frozen aliquots were thawed on ice and lysed mechanically through bead beating by a FastPrep-24 5G lysis machine over six cycles of 45 seconds at 6.5 m/s with 30 seconds on ice between cycles. The lysate was spun down and the supernatant was run through a Zeba Spin Desalting Column. Protein concentration in the desalted lysate was evaluated using a Bradford assay. The samples were kept at 4 °C throughout the procedure.

Limited proteolysis

For every experiment three sample groups were created, one with no added metabolite and two with different concentrations of metabolite specified in **Table S1**. Each sample group was prepared as four technical replicates with 1 μg/μL extracted protein. Proteinase K was simultaneously added to all samples at a 1:100 protease to protein ratio and incubated at 25 °C for exactly 10 minutes before immediate denaturation.

Complete digestion

The protein mix was incubated at 96 °C for 3 min prior to treatment with 5% Sodium Deoxycholate and 10 mM DTT and another 10 min at 96 °C after. The samples were then alkylated by 10 mM Iodoacetamide at RT for 30 min in the dark, after which proteases LysC and trypsin were applied at a 1:100 protease to protein ratio and incubated at 37 °C and 400 RPM in a thermocycler for 3 and 16 hours, respectively. Digestion was halted by addition of formic acid to reduce pH below 2 which caused sodium deoxycholate to precipitate. Samples

were then centrifuged at 14,000g for 10 min after which the supernatant was removed and stored at -20 °C.

Peptide purification

Pipette tips packed with six layers of C18 matrix discs (20-200 µL; Empore SPE Discs) were activated with acetonitrile and equilibrated with 0.1% formic acid prior to being loaded with thawed peptide mixes. The matrix was then washed twice with one loading volume of 0.1% formic acid before being eluted with a mixture of 4:1 ratio of acetonitrile to 0.1% formic acid. The eluate was stored at -20 °C until analysis by LC/MS.

LC/MS analysis

Analysis was performed on a Q-exactive HF Hybrid Quadrupole-Orbitrap Mass Spectrometer coupled with an UltiMate 3000 RSLCnano System with an EASY-Spray ion source. 2 µL of each sample was loaded onto a C18 Acclaim PepMap 100 trap column (75 µm x 2 cm, 3 µm, 100 Å) with a flow rate of 7 µL per min, using 3% acetonitrile, 0.1% formic acid and 96.9% water as solvent. The samples were then separated on ES802 EASY-Spray PepMap RSLC C18 Column (75 µm x 25 cm, 2 µm, 100Å) with a flow rate of 3.6 µL per minute for 40 minutes using a linear gradient from 1% to 32% with 95% acetonitrile, 0.1% formic acid and 4.9% water as secondary solvent. After separation MS analysis was performed using one full scan (resolution 30,000 at 200 m/z, mass range 300 – 1200 m/z) followed by 30 MS2 DIA scans (resolution 30,000 at 200 m/z, mass range 350 – 1000 m/z) with an isolation window of 10 m/z. Precursor ion fragmentation was performed with high-energy collision-induced dissociation at an NCE of 26. The maximum injection times for the MS1 and MS2 were 105 ms and 55 ms respectively, and the automatic gain control was set to $3 \cdot 10^6$ and $1 \cdot 10^6$ respectively. The EncyclopeDIA and ProSight workflows were used to generate a predicted library from a fasta file of the appropriate organisms UniProt proteome set (*C. necator*: UP000008210, *Synechocystis* sp. PCC 6803: UP000001425, *Synechococcus elongatus* sp. PCC 7942: UP000002717, *H. pseudoflava*: UP000293912) against which an EncyclopeDIA search was performed to generate a list of detected peptides.

Data analysis

Peptides detected in at least three replicates in every sample group were tested for differential peptide abundance using the MSstats package (version 3.18.5) in R (version 3.6.3). For every peptide in each metabolite concentration comparison MSstats estimated fold changes and p-values adjusted for multiple hypothesis testing (Benjamini-Hochberg method) with a significance threshold of 0.01. A protein was considered to interact with a metabolite supplied at low or high concentration if at least one peptide showed significant interaction. General data and quality assessment statistics and visualizations were generated by the pipeline available at <https://github.com/Asplund-Samuelsson/lipsmap>, implemented in R version 4.1.1 with Tidyverse version 1.3.1.

Ortholog annotations

In order to compare metabolite-protein interaction patterns between organisms, it was necessary to determine orthologous genes. Ortholog labels from the eggNOG database were downloaded from UniProt (<https://www.uniprot.org/>) on 14 June 2021 for each protein in the four organisms. Version 5.0 of eggNOG was used except for proteins Q31NB2 (ENOG4108VFZ), Q31RK3 (ENOG4105KVS), and Q31RK2 (ENOG4105HKE) in *Synechococcus*, which were annotated with eggNOG version 4.1. Only the 481 orthologs found in all organisms were considered. The number of interacting proteins were counted for each ortholog and metabolite concentration, in each organism. Furthermore, ortholog counts

were summarized into the 20 functional categories each represented by a single letter, e.g. “A” for “RNA processing and modification.”

Principal component analysis of interactions with orthologs

The metabolite-protein interaction patterns of orthologs were compared between metabolites and organisms using R. The interaction per ortholog was first classified binarily so that the interaction was 1 (one) if there was at least one interaction for the ortholog in a particular combination of organism, metabolite, and concentration. Otherwise the interaction was classified as 0 (zero). Orthologs without interactions were filtered out. A matrix with rows representing organism and metabolite, and columns containing the binary interaction classification of each ortholog, was subjected to principal component analysis (PCA; function *prcomp*). The first two principal components were then plotted in order to visualize how similar different organisms and metabolites were in terms of interaction with the full set of orthologous genes. The PCA was performed separately for low and high metabolite concentrations.

Clustered heatmap of interactions with orthologs

The metabolite-protein interaction patterns of orthologs, summarized per ortholog functional category, were further inspected through visualization with a heatmap with clustered rows and columns. The ortholog interaction counts were normalized to indicate the fraction of interacting orthologs within each combination of functional category, organism, metabolite, and concentration. These fractions were then used to calculate Euclidean distance (function *vegdist* from library *vegan*) followed by clustering (*ward.D2* method in function *hclust*), which determined the order of functional categories (heatmap rows), and metabolites and concentrations (heatmap columns). Organisms contributed both to row and column clustering. Finally, the ortholog interaction fractions were plotted as heatmaps, using row and column orders as described, with dendrograms clarifying the clustering (function *ggtree* from library *ggtree*).

Phylogenetic analysis

We wanted to compare evolutionary relationships of Calvin cycle proteins to their interaction patterns in the different organisms, prompting a phylogenetic analysis. Sequences for Calvin cycle KEGG orthologs (KO) in module M00165, supplemented with transaldolase (K00616 and K13810), triose-phosphate isomerase (K01803), and ribulose-phosphate epimerase (K01783), were downloaded from UniProt on 14 October 2021. Each set of KO sequences were reduced in number with cd-hit version 4.8.1 (Fu et al., 2012; Li and Godzik, 2006) by selecting the highest percent identity setting between 50% (-c 0.5) and 100% (-c 1), in 5% steps, that resulted in fewer than 1 000 representative sequences. For each KO set, we added any missing corresponding protein sequences in the four organisms studied here. Sequences were aligned using mafft version 7.453 at default settings (Kato and Standley, 2013). The alignments were then used to construct phylogenetic trees with FastTree version 2.1.11 Double precision at default settings (Price et al., 2010). NCBI taxonomy data downloaded on 8 October 2021 was used to identify organism groups. Trees were plotted using *phytools* and *ggtree* in R in order to visualize the phylogenetic distribution of sequences and metabolite interactions for the four organisms under study.

Ortholog analysis code is available at <https://github.com/Asplund-Samuelsson/lipsmap>.

Cloning and transformation

The *tktA* gene in *PCC6803* and the *cbbTP* gene in *C. necator* were PCR amplified using the primer pairs tktAF+tktAR and cbbTpF+cbbTpR respectively. The backbone pET-28a(+) was linearized using the primer pair pETF+peTR after which the constructs were assembled through Gibson assembly. The products were verified by sequencing and transformed into *E. coli* BL21 by heat shock.

tktAF: 5'-CCATTTGCTGTCCACCAGACAGTGAGGAGTTTTAAGCTTGG-3'
tktAR: 5'-CCGCGCGGCAGCCATATGAACATTATGGTCGTTGCTACCC-3'
cbbTpF: 5'-CCATTTGCTGTCCACCAGATCAAGCGTCCTCCAGCAG-3'
cbbTpR: 5'-CCGCGCGGCAGCCATATGGAGATGAACGCACCCGAACG-3'
pETF: 5'-CATATGGCTGCCGCGCGG-3'
pETR: 5'-CTGGTGGACAGCAAATGGGTCG-3'

Production and purification of recombinant F/SBPase and TKT

The mutants were cultivated in 2YT media at 37 °C and 200 RPM until OD 0.4-0.6 after which overexpression was induced by 1 mM IPTG. The *tktA* gene was incubated at 37 °C for 8h after induction, whereas the *cbbTP* gene was incubated at 18 °C for 24 hours. Cells were harvested by centrifugation at 4 °C and stored at -20 °C. Frozen pellets were resuspended in 3-5 mL of B-PER and incubated on a rocking table for ~30 min before centrifugation at 4,000 g. The soluble fraction was loaded onto an HisTrap Fast Flow Cytiva column (1 mL) and washed with wash buffer (50 mM Tris-HCl, 300 mM NaCl, 20 mM imidazole, pH 7.5) prior to elution with elution buffer (50 mM Tris-HCl, 300 mM NaCl, 500 mM imidazole, pH 7.5). Fractions containing transketolase were combined and the buffer was exchanged to storage buffer (50 mM Tris-HCl, pH 7.5) using a HiTrap Cytiva desalting column. The purified protein was quantified by Bradford assay and stored at -80 °C in aliquots.

Enzyme kinetic validation of TKT metabolite interactions

Transketolase was characterized following (Brilisauer et al., 2019). The conversion of D-ribose-5-phosphate and L-erythrulose to sedoheptulose-7-phosphate and glycolaldehyde was measured through the consumption of NADH by alcohol dehydrogenase when reducing glycolaldehyde to ethylene glycol. Initially, the kinetics were calculated from measurements of reaction rates at 12 different substrate concentrations (0, 100, 200, 300, 400, 500, 600, 800, 1000, 2000, 4000, 8000 μ M) in quadruplicate. Subsequently, relative comparisons of enzyme kinetics were made as calculated from 8 different substrate concentrations (0, 100, 200, 500, 750, 1000, 2000 and 4000 μ M) with and without 1 mM added metabolite. The tested metabolites were 2OG, 2PG, ATP, AMP, G6P, Citrate, Glyoxylate, Malate, NADP and DHAP. The reaction mix contained 100 mM glycylglycine buffer pH 7.5, 5 mM MgCl₂, 2 mM thiamine pyrophosphate, 0.5 mM NADH, 100 mM L-erythrulose, 10 U ADH, 2.875 μ g/mL transketolase and D-ribose-5-phosphate to a final volume of 100 μ L. Absorption was measured at 340 nm twice per minute over 30 minutes starting immediately after addition of D-ribose-5-phosphate.

Enzyme kinetic validation of F/SBPase metabolite interactions

In vitro enzyme activity assays were conducted to validate the kinetic effect of F/SBPase metabolite interactions detected by LiP-SMap. To determine metabolite-induced changes in enzyme kinetic parameters, reaction rates were measured at eight different substrate concentrations (0, 30, 55, 80, 110, 150, 220, 300 μ M) in the presence and absence of a metabolite (+M and -M). Tested metabolites were GAP, NADPH, AMP, AcCoA, and citrate (0.5, 3, 0.25, 2, and 5 mM, respectively). The conversion rate of fructose-1-6-bisphosphate to fructose-6-phosphate was determined from the release of inorganic phosphate over time, using a Malachite Green (MG) assay adapted from (Vardakou et al., 2014). MG dye stock (1.55 g/L Malachite Green oxalate salt, 3 M H₂SO₄) was used to prepare a fresh phosphate colorimetric development solution prior to each experiment (400 μ L MG dye stock, 125 μ L ammonium molybdate (60 mM), 10 μ L Tween-20 (11% v/v)). The development solution was filtered through a 0.2 μ m syringe filter and kept in the dark. Development plates were prepared by mixing 36 μ L development solution with 100 μ L reaction buffer (50 mM Tris-HCl, 15 mM MgCl₂, 10 mM DTT) lacking DTT. Enzyme solutions for +M and -M conditions were

prepared in separate 8-tube PCR strips (VWR #732-1521 or low-protein binding) by mixing 25 μL reaction buffer (+M/-M) with 25 μL purified enzyme constituted in -M reaction buffer. The two strips were pre-incubated at 30 $^{\circ}\text{C}$ for 12 minutes in a thermocycler together with two additional PCR strips which contained substrate at eight different concentrations in -M reaction buffer. Reactions were initiated by quickly mixing 50 μL substrate with the enzyme mixture in one of the reaction strips, using a multipipette ($[\text{F/SBPase}]_{\text{Final}}=0.42 \text{ ng}/\mu\text{L}$). A sample of 20 μL was immediately transferred to a development plate before incubating the reaction strip at 30 $^{\circ}\text{C}$. The initiation procedure was repeated for the second reaction strip with a two minute delay. Samples were collected after 10, 20, and 30 minutes. Each sampling event was followed by an addition of 7.5 μL sodium citrate (34% w/v) to stabilize the color of the development solution. Triplicate series of phosphate standards (0-100 μM) were added to the development plate as a reference. The plate was incubated for 20 minutes in the dark before measuring the absorbance at 620 nm in a plate reader. The experiment was replicated twice. To quantify the amount of phosphate, the background absorbance measured at time zero was first subtracted from raw absorbance measurements. Phosphate standard series were then used to convert absorbances to phosphate concentrations. Outliers and phosphate concentrations that were lower than 10 μM (sensitivity threshold), or that exceeded 60% of the initial substrate concentration (10-minute time points were always kept nonetheless), were removed. Reaction rates were calculated as the change in phosphate concentration over time using linear regression. To determine kinetic parameters, reaction rates and substrate concentrations were fit to the Hill equation using non-linear regression. A parameter change was considered statistically significant for $p < 0.05$ (Student's t-test).

Melting point measurements

The samples were drawn up into capillaries and inserted in a Prometheus NT.48 nanoDSF machine set to 95% excitation power that assayed the stability of the sample while increasing the temperature from 20 $^{\circ}\text{C}$ to 95 $^{\circ}\text{C}$ at a rate of 1 $^{\circ}\text{C}$ per minute. Transketolase samples were prepared in 50 mM Tris-HCl pH 7.5 with 5 mM MgCl_2 , 2 mM TPP, 200 ng/ μL enzyme and 1 mM of metabolite. In addition, samples with and without 2 mM TPP and 10 mM DTT were also run to assay the effect of the cofactor and reductive power on protein stability. F/SBPase samples were prepared in 50 mM Tris-HCl pH 8 with 15 mM MgCl_2 , 10 mM DTT and varying concentrations of metabolite (**Table 1**). Additional samples with 5 mM citrate were run while varying MgCl_2 concentrations were run to investigate if the observed effects were due to magnesium chelation.

Kinetic metabolic model

Model structure

The kinetic model for *Synechocystis* central carbon metabolism was based on a previous model (Janasch et al., 2019), and expanded to cover the reactions of photorespiration, oxidative pentose phosphate (OPP) pathway, anaplerotic reactions around acetyl-CoA and pyruvate, as well as the TCA cycle with its forked nature. The final model contained 53 reactions connecting 57 metabolites (41 internal). Sink reactions were formulated as irreversible Michaelis-Menten-type equations. Supply reactions followed mass action kinetics. Four model variants were created: One base model, including only the regulatory interactions in the previous version (Janasch et al., 2019), two models with interactions on F/SBPase (AMP, GAP, NADPH, CIT) and TKT1/2 (AMP, ATP, CIT, GLX, RuBP), respectively, and one model including all regulations.

Metabolic flux distribution

The steady-state flux distribution was obtained using a genome-scale metabolic model (GEM) of *Synechocystis* (Sarkar et al., 2019). All flux simulations were performed in Matlab

R2020b using the *Gurobi Optimizer* version 9.1.1. First, the GEM was modified by allowing reversibility of the conversion of NADPH to NADH and replacing the two individual reactions corresponding to Rubisco carboxylase and oxygenase by a single Rubisco reaction representing 97% carboxylase and 3% oxygenase activity as implemented in a previous network reconstruction (Knoop et al., 2013). Fluxes were constrained by ranges taken from Gopalakrishnan et al., 2018 (Gopalakrishnan et al., 2018), bicarbonate uptake was constrained to a maximum of $3.7 \text{ mmol} \cdot \text{gDW}^{-1} \cdot \text{h}^{-1}$ (Nogales et al., 2012). Maximizing autotrophic growth was set as the objective function and fluxes were sampled using the *randomSampling* function of the RAVEN Toolbox 2 version 2.4.3 (Wang et al., 2018) allowing for 95% of the optimized objective value. Fluxes were manually curated to adjust the genome-scale flux distribution to the small-scale kinetic model structure and transformed into mM/min by multiplying with a cellular density of 434.78 g/L (*E. coli*, (Bennett et al., 2008)).

Metabolite concentrations

Due to the uncertainty associated with published metabolomics datasets, potential thermodynamically feasible metabolite concentrations describing the metabolic state were randomly sampled, as performed similarly before (Janasch et al., 2019). Metabolite concentration ranges identified via NET analysis (Asplund-Samuelsson et al., 2018) were adjusted to the present model structure and used as constraints for the sampling. To cover the whole feasible solution space efficiently, a hit-and-run algorithm was employed. Starting from a feasible metabolite concentration set (fMCS), the algorithm randomly selects a direction and feasible step length to move through the logarithmic solution space, creating fMCSs with each step. MDF (Noor et al., 2014) analysis followed by thermodynamic variability analysis (Janasch et al., 2021 *manuscript*) was used to identify 83 fMCSs as starting points for the random sampling. For each initial fMCS, five runs were performed with each $1 \cdot 10^6$ steps, of which each 1000th step was recorded resulting in ~415000 fMCSs. Pool sizes for the supply reactions were sampled in a range between 1.1x to 5x around their corresponding metabolite concentrations, simulating fast supply (pool size close to metabolite concentration) and slow supply, respectively. For practical reasons 5000 fMCSs were randomly selected to form a representative overview of the thermodynamically feasible concentrations of the analyzed metabolic state to be used in the subsequent parameter sampling.

Parameter Sampling

Rate equations were generally parameterized around the corresponding metabolite concentrations by sampling the range of 0.01x to 100x metabolite concentration in logarithmic space for K_m values, corresponding to 99% to 1% active site saturation, as performed previously (Janasch et al., 2019). Inhibition constants K_i for the regulations identified by LiP-SMap were sampled in a narrower range of 0.2x to 5x around the metabolite concentrations used for the enzyme assays. For F/SBPase 50 μM , 3 mM and 5 mM were used for AMP, NADPH and CIT, respectively. For TKT, all interaction constants were sampled around 1 mM. For the activation of F/SBPase by GAP, K_m could maximally be reduced by 75%. Hill coefficients for FBPase and TKT1/2 were sampled between 1 and 2, while for SBPase the range was between 1 and 4, following the observed difference between FBPase and SBPase reactions identified in (Feng et al., 2014a). V_{max} values were calculated back from metabolite concentrations, sampled kinetic constants and the steady-state flux distribution. For each of the 5000 fMCSs, 1000 parameter samplings were performed, resulting in an ensemble of 5 million kinetic steady-state models to be analyzed for stability and metabolic control.

Metabolic control analysis

The dynamic behavior of the models was analyzed by linearizing them around their steady-state as performed previously (Janasch et al., 2019; Murabito et al., 2014), based on (Reder, 1990), by forming the Jacobian matrix. The stability of each model in the ensemble was evaluated by calculating the eigenvalues of the Jacobian matrix, where positive

eigenvalues cause instability. Flux control coefficients were calculated for all stable parameter sets based on elasticities and concentration control coefficients as described in (Janasch et al., 2019). The models and all code required to perform the kinetic modelling analysis is available at https://github.com/MJanasch/KX_Kinetics.

Acknowledgements

We are grateful to Michael Jahn (KTH Stockholm) for helpful discussion on proteomics and cultivation of *Cupriavidus necator*. We thank Ralf Steuer (Humboldt University, Berlin) for discussions on kinetic modeling.

Funding for this work was from the Swedish Research Council Vetenskapsrådet (grant number 2016-06160), the Swedish Foundation for Strategic Research SSF (ARC19-0051) and the Novo Nordisk Foundation (grant numbers NNF19OC0057652 and NNF20OC0061469).

Contributions

Conceptualization: EPH, PS, FE, IP, JAS, JK, ES

Experimental proteomics: JK, ES, DK, LS, FE

Proteomics data analysis: JAS, JK, ES, FE

Enzyme kinetics and melting analyses: JK, KS, ES

Metabolic modeling: MJ, LZ

Writing initial draft: EPH, ES, JK, JAS, MJ

Editing of final draft: EPH, ES, JK, JAS, MJ, KS

Funding acquisition: EPH, PS

References

Abramson, B.W., Kachel, B., Kramer, D.M., and Ducat, D.C. (2016). Increased Photochemical Efficiency in Cyanobacteria via an Engineered Sucrose Sink. *Plant Cell Physiol.* 57, 2451–2460.

Acharya, A.S., and Manning, J.M. (1980). Reactivity of the amino groups of carbonmonoxyhemoglobin S with glyceraldehyde. *J. Biol. Chem.* 255, 1406–1412.

Acharya, A.S., and Sussman, L.G. (1983). Reductive hydroxyethylation of hemoglobin A. Functional properties of hemoglobin A selectively hydroxyethylated or dihydroxypropylated at the alpha-amino groups. *J. Biol. Chem.* 258, 13761–13767.

Asplund-Samuelsson, J., and Hudson, E.P. (2021). Wide range of metabolic adaptations to the acquisition of the Calvin cycle revealed by comparison of microbial genomes. *PLoS Comput. Biol.* 17, e1008742.

Asplund-Samuelsson, J., Janasch, M., and Hudson, E.P. (2018). Thermodynamic analysis of computed pathways integrated into the metabolic networks of *E. coli* and *Synechocystis* reveals contrasting expansion potential. *Metab. Eng.* 45, 223–236.

Barenholz, U., Davidi, D., Reznik, E., Bar-On, Y., Antonovsky, N., Noor, E., and Milo, R. (2017). Design principles of autocatalytic cycles constrain enzyme kinetics and force low substrate saturation

at flux branch points. *Elife* 6.

Beck, C., Knoop, H., Axmann, I.M., and Steuer, R. (2012). The diversity of cyanobacterial metabolism: genome analysis of multiple phototrophic microorganisms. *BMC Genomics* 13, 1–17.

Bennett, B.D., Yuan, J., Kimball, E.H., and Rabinowitz, J.D. (2008). Absolute quantitation of intracellular metabolite concentrations by an isotope ratio-based approach. *Nat. Protoc.* 3, 1299–1311.

Borirak, O., de Koning, L.J., van der Woude, A.D., Hoefsloot, H.C.J., Dekker, H.L., Roseboom, W., de Koster, C.G., and Hellingwerf, K.J. (2015). Quantitative proteomics analysis of an ethanol- and a lactate-producing mutant strain of *Synechocystis* sp. PCC6803. *Biotechnol. Biofuels* 8, 111.

Bowien, B., and Kusian, B. (2002). Genetics and control of CO₂ assimilation in the chemoautotroph *Ralstonia eutropha*. *Arch. Microbiol.* 178, 85–93.

Brilisauer, K., Rapp, J., Rath, P., Schöllhorn, A., Bleul, L., Weiß, E., Stahl, M., Grond, S., and Forchhammer, K. (2019). Cyanobacterial antimetabolite 7-deoxy-sedoheptulose blocks the shikimate pathway to inhibit the growth of prototrophic organisms. *Nat. Commun.* 10, 1–11.

Brown, G., Singer, A., Lunin, V.V., Proudfoot, M., Skarina, T., Flick, R., Kochinyan, S., Sanishvili, R., Joachimiak, A., Edwards, A.M., et al. (2009). Structural and biochemical characterization of the type II fructose-1,6-bisphosphatase GlpX from *Escherichia coli*. *J. Biol. Chem.* 284, 3784–3792.

Christodoulou, D., Kuehne, A., Estermann, A., Fuhrer, T., Lang, P., and Sauer, U. (2019). Reserve Flux Capacity in the Pentose Phosphate Pathway by NADPH Binding Is Conserved across Kingdoms. *iScience* 19, 1133–1144.

Cohen, S.E., and Golden, S.S. (2015). Circadian Rhythms in Cyanobacteria. *Microbiol. Mol. Biol. Rev.* 79, 373–385.

Cotton, C.A.R., Kabasakal, B.V., Miah, N.A., and Murray, J.W. (2015). Structure of the dual-function fructose-1,6/sedoheptulose-1,7-bisphosphatase from *Thermosynechococcus elongatus* bound with sedoheptulose-7-phosphate. *Acta Crystallogr. Sect. F Struct. Biol. Cryst. Commun.* 71, 1341–1345.

Dangel, A.W., and Tabita, F.R. (2015). CbbR, the Master Regulator for Microbial Carbon Dioxide Fixation. *J. Bacteriol.* 197, 3488–3498.

De Porcellinis, A.J., Nørgaard, H., Brey, L.M.F., Erstad, S.M., Jones, P.R., Heazlewood, J.L., and Sakuragi, Y. (2018). Overexpression of bifunctional fructose-1,6-bisphosphatase/sedoheptulose-1,7-bisphosphatase leads to enhanced photosynthesis and global reprogramming of carbon metabolism in *Synechococcus* sp. PCC 7002. *Metab. Eng.* 47, 170–183.

Eisenhut, M., Huege, J., Schwarz, D., Bauwe, H., Kopka, J., and Hagemann, M. (2008). Metabolome phenotyping of inorganic carbon limitation in cells of the wild type and photorespiratory mutants of the cyanobacterium *Synechocystis* sp. strain PCC 6803. *Plant Physiol.* 148, 2109–2120.

Feng, L., Sun, Y., Deng, H., Li, D., Wan, J., Wang, X., Wang, W., Liao, X., Ren, Y., and Hu, X. (2014a). Structural and biochemical characterization of fructose-1,6/sedoheptulose-1,7-bisphosphatase from the cyanobacterium *Synechocystis* strain 6803. *FEBS J.* 281, 916–926.

Feng, Y., De Franceschi, G., Kahraman, A., Soste, M., Melnik, A., Boersema, P.J., de Laureto, P.P., Nikolaev, Y., Oliveira, A.P., and Picotti, P. (2014b). Global analysis of protein structural changes in complex proteomes. *Nat. Biotechnol.* 32, 1036–1044.

Flügel, F., Timm, S., Arrivault, S., Florian, A., Stitt, M., Fernie, A.R., and Bauwe, H. (2017). The Photorespiratory Metabolite 2-Phosphoglycolate Regulates Photosynthesis and Starch Accumulation in *Arabidopsis*. *Plant Cell* 29, 2537–2551.

- Fu, L., Niu, B., Zhu, Z., Wu, S., and Li, W. (2012). CD-HIT: accelerated for clustering the next-generation sequencing data. *Bioinformatics* 28, 3150–3152.
- Ganapathy, U., Marrero, J., Calhoun, S., Eoh, H., de Carvalho, L.P.S., Rhee, K., and Ehrt, S. (2015). Two enzymes with redundant fructose biphosphatase activity sustain gluconeogenesis and virulence in *Mycobacterium tuberculosis*. *Nat. Commun.* 6, 7912.
- Gerosa, L., van Rijsewijk, B.R.B.H., Christodoulou, D., Kochanowski, K., Schmidt, T.S.B., Noor, E., and Sauer, U. (2015). Pseudo-transition Analysis Identifies the Key Regulators of Dynamic Metabolic Adaptations from Steady-State Data. *Cell Systems* 1, 270–282.
- Gopalakrishnan, S., Pakrasi, H.B., and Maranas, C.D. (2018). Elucidation of photoautotrophic carbon flux topology in *Synechocystis* PCC 6803 using genome-scale carbon mapping models. *Metab. Eng.* 47, 190–199.
- Grenz S, Baumann PT, Rückert C, Nebel BA, Siebert D, Schwentner A, Eikmanns BJ, Hauer B, Kalinowski J, Takors R, Blombach B (2019). Exploiting Hydrogenophaga pseudoflava for aerobic syngas-based production of chemicals. *Metabolic Engineering* 55, 220–230.
- Grimbs, S., Selbig, J., Bulik, S., Holzhütter, H.-G., and Steuer, R. (2007). The stability and robustness of metabolic states: identifying stabilizing sites in metabolic networks. *Mol. Syst. Biol.* 3, 146.
- Guerreiro, A.C.L., Penning, R., Raaijmakers, L.M., Axman, I.M., Heck, A.J.R., and Altelaar, A.F.M. (2016). Monitoring light/dark association dynamics of multi-protein complexes in cyanobacteria using size exclusion chromatography-based proteomics. *J. Proteomics* 142, 33–44.
- Hackett, S.R., Zanolli, V.R.T., Xu, W., Goya, J., Park, J.O., Perlman, D.H., Gibney, P.A., Botstein, D., Storey, J.D., and Rabinowitz, J.D. (2016). Systems-level analysis of mechanisms regulating yeast metabolic flux. *Science* 354.
- Jablonsky, J., Papacek, S., and Hagemann, M. (2016). Different strategies of metabolic regulation in cyanobacteria: from transcriptional to biochemical control. *Sci. Rep.* 6, 33024.
- Jahn, M., Vialas, V., Karlsen, J., Maddalo, G., Edfors, F., Forsström, B., Uhlén, M., Käll, L., and Hudson, E.P. (2018). Growth of Cyanobacteria Is Constrained by the Abundance of Light and Carbon Assimilation Proteins. *Cell Rep.* 25, 478–486.e8.
- Jahn, M., Crang, N., Janasch, M., Hober, A., Forsström, B., Kimler, K., Mattausch, A., Chen, Q., Asplund-Samuelsson, J., and Hudson, E.P. (2021). Protein allocation and utilization in the versatile chemolithoautotroph *Cupriavidus necator*.
- Jaiswal, D., and Wangikar, P.P. (2020). Dynamic Inventory of Intermediate Metabolites of Cyanobacteria in a Diurnal Cycle. *iScience* 23, 101704.
- Janasch, M., Asplund-Samuelsson, J., Steuer, R., and Hudson, E.P. (2019). Kinetic modeling of the Calvin cycle identifies flux control and stable metabolomes in *Synechocystis* carbon fixation. *J. Exp. Bot.* 70, 973–983.
- Katoh, K., and Standley, D.M. (2013). MAFFT multiple sequence alignment software version 7: improvements in performance and usability. *Mol. Biol. Evol.* 30, 772–780.
- Klähn, S., Orf, I., Schwarz, D., Matthiessen, J.K.F., Kopka, J., Hess, W.R., and Hagemann, M. (2015). Integrated Transcriptomic and Metabolomic Characterization of the Low-Carbon Response Using an *ndhR* Mutant of *Synechocystis* sp. PCC 6803. *Plant Physiol.* 169, 1540–1556.
- Knoop, H., Gründel, M., Zilliges, Y., Lehmann, R., Hoffmann, S., Lockau, W., and Steuer, R. (2013). Flux balance analysis of cyanobacterial metabolism: the metabolic network of *Synechocystis* sp. PCC 6803. *PLoS Comput. Biol.* 9, e1003081.

- Koch, M., Bruckmoser, J., Scholl, J., Hauf, W., Rieger, B., and Forchhammer, K. (2020). Maximizing PHB content in *Synechocystis* sp. PCC 6803: a new metabolic engineering strategy based on the regulator PirC. *Microb. Cell Fact.* **19**, 231.
- Kochanowski, K., Volkmer, B., Gerosa, L., Haverkorn van Rijsewijk, B.R., Schmidt, A., and Heinemann, M. (2013). Functioning of a metabolic flux sensor in *Escherichia coli*. *Proc. Natl. Acad. Sci. U. S. A.* **110**, 1130–1135.
- Kopka, J., Schmidt, S., Dethloff, F., Pade, N., Berendt, S., Schottkowski, M., Martin, N., Dühning, U., Kuchmina, E., Enke, H., et al. (2017). Systems analysis of ethanol production in the genetically engineered cyanobacterium sp. PCC 7002. *Biotechnol. Biofuels* **10**, 56.
- Krieg, T., Sydow, A., Faust, S., Huth, I., and Holtmann, D. (2018). CO₂to Terpenes: Autotrophic and Electroautotrophic α -Humulene Production with *Cupriavidus necator*. *Angewandte Chemie* **130**, 1897–1900.
- Kusian, B., and Bowien, B. (1997). Organization and regulation of cbb CO₂ assimilation genes in autotrophic bacteria. *FEMS Microbiol. Rev.* **21**, 135–155.
- Lempp, M., Farke, N., Kuntz, M., Freibert, S.A., Lill, R., and Link, H. (2019). Systematic identification of metabolites controlling gene expression in *E. coli*. *Nat. Commun.* **10**, 1–9.
- Li, W., and Godzik, A. (2006). Cd-hit: a fast program for clustering and comparing large sets of protein or nucleotide sequences. *Bioinformatics* **22**, 1658–1659.
- Li, G., Hu, Y., Zrimec, J., Luo, H., Wang, H., Zelezniak, A., Ji, B., and Nielsen, J. (2021). Bayesian genome scale modelling identifies thermal determinants of yeast metabolism. *Nat. Commun.* **12**, 1–12.
- Li, X., Gianoulis, T.A., Yip, K.Y., Gerstein, M., and Snyder, M. (2010). Extensive in vivo metabolite-protein interactions revealed by large-scale systematic analyses. *Cell* **143**, 639–650.
- Liang, F., and Lindblad, P. (2016). Effects of overexpressing photosynthetic carbon flux control enzymes in the cyanobacterium *Synechocystis* PCC 6803. *Metab. Eng.* **38**, 56–64.
- Link, H., Kochanowski, K., and Sauer, U. (2013). Systematic identification of allosteric protein-metabolite interactions that control enzyme activity in vivo. *Nat. Biotechnol.* **31**, 357–361.
- Liu, X., Miao, R., Lindberg, P., and Lindblad, P. (2019). Modular engineering for efficient photosynthetic biosynthesis of 1-butanol from CO₂ in cyanobacteria. *Energy & Environmental Science* **12**, 2765–2777.
- Maloney, R.J., and Dennis, D.T. (1977). The role of divalent cations in the activation of the NADP⁺-specific isocitrate dehydrogenase from *Pisum sativum* L. *Can. J. Biochem.* **55**, 928–934.
- Markert, B., Stolzenberger, J., Brautaset, T., and Wendisch, V.F. (2014). Characterization of two transketolases encoded on the chromosome and the plasmid pBM19 of the facultative ribulose monophosphate cycle methylotroph *Bacillus methanolicus*. *BMC Microbiol.* **14**, 7.
- Martell, A.E., and Smith, R.M. (2013). *Critical stability constants: First supplement* (New York, NY: Springer).
- Martin, W., Scheibe, R., and Schnarrenberger, C. (2000). The Calvin Cycle and Its Regulation. *Photosynthesis* 9–51.
- Mateus, A., Bobonis, J., Kurzawa, N., Stein, F., Helm, D., Hevler, J., Typas, A., and Savitski, M.M. (2018). Thermal proteome profiling in bacteria: probing protein state. *Mol. Syst. Biol.* **14**, e8242.
- Mateus, A., Savitski, M.M., and Piazza, I. (2021). The rise of proteome-wide biophysics. *Mol. Syst.*

Biol. 17, e10442.

McKinlay, J.B., and Harwood, C.S. (2010). Carbon dioxide fixation as a central redox cofactor recycling mechanism in bacteria. *Proc. Natl. Acad. Sci. U. S. A.* 107, 11669–11675.

Mettler, T., Mühlhaus, T., Hemme, D., Schöttler, M.-A., Rupprecht, J., Idoine, A., Veyel, D., Pal, S.K., Yaneva-Roder, L., Winck, F.V., et al. (2014). Systems Analysis of the Response of Photosynthesis, Metabolism, and Growth to an Increase in Irradiance in the Photosynthetic Model Organism *Chlamydomonas reinhardtii*. *Plant Cell* 26, 2310–2350.

Meyer, O., and Schlegel, H.G. (1978). Reisolation of the carbon monoxide utilizing hydrogen bacterium *Pseudomonas carboxydovorans* (Kistner) comb. nov. *Arch. Microbiol.* 118, 35–43.

Michelet, L., Zaffagnini, M., Morisse, S., Sparla, F., Pérez-Pérez, M.E., Francia, F., Danon, A., Marchand, C.H., Fermani, S., Trost, P., et al. (2013). Redox regulation of the Calvin-Benson cycle: something old, something new. *Front. Plant Sci.* 4, 470.

Millard, P., Enjalbert, B., Uttenweiler-Joseph, S., Portais, J.-C., and Létisse, F. (2021). Control and regulation of acetate overflow in. *Elife* 10.

Mo, R., Yang, M., Chen, Z., Cheng, Z., Yi, X., Li, C., He, C., Xiong, Q., Chen, H., Wang, Q., et al. (2015). Acetylome analysis reveals the involvement of lysine acetylation in photosynthesis and carbon metabolism in the model cyanobacterium *Synechocystis* sp. PCC 6803. *J. Proteome Res.* 14, 1275–1286.

Müller, J., MacEachran, D., Burd, H., Sathitsuksanoh, N., Bi, C., Yeh, Y.-C., Lee, T.S., Hillson, N.J., Chhabra, S.R., Singer, S.W., et al. (2013). Engineering of *Ralstonia eutropha* H16 for autotrophic and heterotrophic production of methyl ketones. *Appl. Environ. Microbiol.* 79, 4433–4439.

Murabito, E., Verma, M., Bekker, M., Bellomo, D., Westerhoff, H.V., Teusink, B., and Steuer, R. (2014). Monte-Carlo Modeling of the Central Carbon Metabolism of *Lactococcus lactis*: Insights into Metabolic Regulation. *PLoS ONE* 9, e106453.

Natsch, A., Gfeller, H., Haupt, T., and Brunner, G. (2012). Chemical reactivity and skin sensitization potential for benzaldehydes: can Schiff base formation explain everything? *Chem. Res. Toxicol.* 25, 2203–2215.

Nishiguchi, H., Liao, J., Shimizu, H., and Matsuda, F. (2020). Novel allosteric inhibition of phosphoribulokinase identified by ensemble kinetic modeling of sp. PCC 6803 metabolism. *Metab Eng Commun* 11, e00153.

Nogales, J., Gudmundsson, S., Knight, E.M., Palsson, B.O., and Thiele, I. (2012). Detailing the optimality of photosynthesis in cyanobacteria through systems biology analysis. *Proc. Natl. Acad. Sci. U. S. A.* 109, 2678–2683.

Noor, E., Bar-Even, A., Flamholz, A., Reznik, E., Liebermeister, W., and Milo, R. (2014). Pathway thermodynamics highlights kinetic obstacles in central metabolism. *PLoS Comput. Biol.* 10, e1003483.

Pattanayak GK, Liao Y, Wallace EWJ, Budnik B, Drummond DA, Rust MJ (2020). Daily Cycles of Reversible Protein Condensation in Cyanobacteria. *Cell Reports* 32, 108032.

Pecoraro, V.L., Hermes, J.D., and Cleland, W.W. (1984). Stability constants of Mg²⁺ and Cd²⁺ complexes of adenine nucleotides and thionucleotides and rate constants for formation and dissociation of MgATP and MgADP. *Biochemistry* 23, 5262–5271.

Pettersson, G., and Ryde-Pettersson, U. (1989a). Dependence of the Calvin cycle activity on kinetic parameters for the interaction of non-equilibrium cycle enzymes with their substrates. *Eur. J. Biochem.* 186, 683–687.

Pettersson, G., and Ryde-Pettersson, U. (1989b). On the regulatory significance of inhibitors acting on non-equilibrium enzymes in the Calvin photosynthesis cycle. *Eur. J. Biochem.* **182**, 373–377.

Piazza, I., Beaton, N., Bruderer, R., Knobloch, T., Barbisan, C., Chandat, L., Sudau, A., Siepe, I., Rinner, O., de Souza, N., et al. (2020). A machine learning-based chemoproteomic approach to identify drug targets and binding sites in complex proteomes. *Nat. Commun.* **11**, 1–13.

Piazza I, Kochanowski K, Cappelletti V, Fuhrer T, Noor E, Sauer U, Picotti P (2018). A Map of Protein-Metabolite Interactions Reveals Principles of Chemical Communication. *Cell* **172**, 358–372.e23.

Pohlmann, A., Fricke, W.F., Reinecke, F., Kusian, B., Liesegang, H., Cramm, R., Eiting, T., Ewering, C., Pötter, M., Schwartz, E., et al. (2006). Genome sequence of the bioplastic-producing “Knallgas” bacterium *Ralstonia eutropha* H16. *Nature Biotechnology* **24**, 1257–1262.

Price, M.N., Dehal, P.S., and Arkin, A.P. (2010). FastTree 2--approximately maximum-likelihood trees for large alignments. *PLoS One* **5**, e9490.

Raines, C.A. (2003). The Calvin cycle revisited. *Photosynth. Res.* **75**, 1–10.

Reder, C. (1990). The Structural Approach to Metabolic Control Analysis I: Theoretical Aspects. *Control of Metabolic Processes* 121–127.

Saa, P.A., and Nielsen, L.K. (2016). A probabilistic framework for the exploration of enzymatic capabilities based on feasible kinetics and control analysis. *Biochim. Biophys. Acta* **1860**, 576–587.

Sander, T., Farke, N., Diehl, C., Kuntz, M., Glatter, T., and Link, H. (2019). Allosteric Feedback Inhibition Enables Robust Amino Acid Biosynthesis in *E. coli* by Enforcing Enzyme Overabundance. *Cell Syst* **8**, 66–75.e8.

Sarkar, D., Mueller, T.J., Liu, D., Pakrasi, H.B., and Maranas, C.D. (2019). A diurnal flux balance model of *Synechocystis* sp. PCC 6803 metabolism. *PLoS Comput. Biol.* **15**, e1006692.

Savitski, M.M., Reinhard, F.B.M., Franken, H., Werner, T., Savitski, M.F., Eberhard, D., Martinez Molina, D., Jafari, R., Dovega, R.B., Klaeger, S., et al. (2014). Tracking cancer drugs in living cells by thermal profiling of the proteome. *Science* **346**, 1255784.

Schuster, R., and Holzhütter, H.G. (1995). Use of mathematical models for predicting the metabolic effect of large-scale enzyme activity alterations. Application to enzyme deficiencies of red blood cells. *Eur. J. Biochem.* **229**, 403–418.

Schwarz, D., Nodop, A., Hüge, J., Purfürst, S., Forchhammer, K., Michel, K.P., Bauwe, H., Kopka, J., and Hagemann, M. (2011). Metabolic and transcriptomic phenotyping of inorganic carbon acclimation in the Cyanobacterium *Synechococcus elongatus* PCC 7942. *Plant Physiol.* **155**.

Selim, K.A., Haase, F., Hartmann, M.D., Hagemann, M., and Forchhammer, K. (2018). PII-like signaling protein SbtB links cAMP sensing with cyanobacterial inorganic carbon response. *Proceedings of the National Academy of Sciences* **115**, E4861–E4869.

Shen, G., and Vermaas, W.F. (1994). Chlorophyll in a *Synechocystis* sp. PCC 6803 mutant without photosystem I and photosystem II core complexes. Evidence for peripheral antenna chlorophylls in cyanobacteria. *Journal of Biological Chemistry* **269**, 13904–13910.

Sridharan, S., Kurzawa, N., Werner, T., Günthner, I., Helm, D., Huber, W., Bantscheff, M., and Savitski, M.M. (2019). Proteome-wide solubility and thermal stability profiling reveals distinct regulatory roles for ATP. *Nat. Commun.* **10**, 1–13.

Stolzenberger, J., Lindner, S.N., Persicke, M., Brautaset, T., and Wendisch, V.F. (2013). Characterization of fructose 1,6-bisphosphatase and sedoheptulose 1,7-bisphosphatase from the

facultative ribulose monophosphate cycle methylotroph *Bacillus methanolicus*. *J. Bacteriol.* **195**, 5112–5122.

Sun, M., Xu, J., Wu, Z., Zhai, L., Liu, C., Cheng, Z., Xu, G., Tao, S., Ye, B.-C., Zhao, Y., et al. (2016). Characterization of Protein Lysine Propionylation in *Escherichia coli*: Global Profiling, Dynamic Change, and Enzymatic Regulation. *J. Proteome Res.* **15**, 4696–4708.

Tamoi, M., Murakami, A., Takeda, T., and Shigeoka, S. (1998). Acquisition of a new type of fructose-1,6-bisphosphatase with resistance to hydrogen peroxide in cyanobacteria: molecular characterization of the enzyme from *Synechocystis* PCC 6803. *Biochim. Biophys. Acta* **1383**, 232–244.

Tan, C.S.H., Go, K.D., Bisteau, X., Dai, L., Yong, C.H., Prabhu, N., Ozturk, M.B., Lim, Y.T., Sreekumar, L., Lenggqvist, J., et al. (2018). Thermal proximity coaggregation for system-wide profiling of protein complex dynamics in cells. *Science* **359**, 1170–1177.

Vardakou, M., Salmon, M., Faraldos, J.A., and O'Maille, P.E. (2014). Comparative analysis and validation of the malachite green assay for the high throughput biochemical characterization of terpene synthases. *MethodsX* **1**, 187–196.

Veyel, D., Sokolowska, E.M., Moreno, J.C., Kierszniowska, S., Cichon, J., Wojciechowska, I., Luzarowski, M., Kosmacz, M., Szlachetko, J., Gorka, M., et al. (2018). PROMIS, global analysis of PROtein-metabolite interactions using size separation in. *J. Biol. Chem.* **293**, 12440–12453.

Wagner, G.R., and Payne, R.M. (2013). Widespread and enzyme-independent N ϵ -acetylation and N ϵ -succinylation of proteins in the chemical conditions of the mitochondrial matrix. *J. Biol. Chem.* **288**, 29036–29045.

Wang, H., Marcišauskas, S., Sánchez, B.J., Domenzain, I., Hermansson, D., Agren, R., Nielsen, J., and Kerkhoven, E.J. (2018). RAVEN 2.0: A versatile toolbox for metabolic network reconstruction and a case study on *Streptomyces coelicolor*. *PLoS Comput. Biol.* **14**, e1006541.

Werner, A., Broeckling, C.D., Prasad, A., and Peebles, C.A.M. (2019). A comprehensive time-course metabolite profiling of the model cyanobacterium *Synechocystis* sp. PCC 6803 under diurnal light:dark cycles. *Plant J.* **99**, 379–388.

Wilkinson, H.C., and Dalby, P.A. (2020). The Two-Species Model of transketolase explains donor substrate-binding, inhibition and heat-activation. *Sci. Rep.* **10**, 1–10.

Wolf, N.M., Gutka, H.J., Movahedzadeh, F., and Abad-Zapatero, C. (2018). Structures of the *Mycobacterium tuberculosis* GlpX protein (class II fructose-1,6-bisphosphatase): implications for the active oligomeric state, catalytic mechanism and citrate inhibition. *Acta Crystallogr D Struct Biol* **74**, 321–331.

Woolston, B.M., King, J.R., Reiter, M., Van Hove, B., and Stephanopoulos, G. (2018). Improving formaldehyde consumption drives methanol assimilation in engineered *E. coli*. *Nat. Commun.* **9**, 1–12.

Yang, M., Huang, H., and Ge, F. (2019). Lysine Propionylation is a Widespread Post-Translational Modification Involved in Regulation of Photosynthesis and Metabolism in Cyanobacteria. *Int. J. Mol. Sci.* **20**.

Yu King Hing, N., Liang, F., Lindblad, P., and Morgan, J.A. (2019). Combining isotopically non-stationary metabolic flux analysis with proteomics to unravel the regulation of the Calvin-Benson-Bassham cycle in *Synechocystis* sp. PCC 6803. *Metab. Eng.* **56**, 77–84.

Zampieri, M., Hörl, M., Hotz, F., Müller, N.F., and Sauer, U. (2019). Regulatory mechanisms underlying coordination of amino acid and glucose catabolism in *Escherichia coli*. *Nat. Commun.* **10**, 1–13.

Zavřel, T., Faizi, M., Loureiro, C., Poschmann, G., Stühler, K., Sinetova, M., Zorina, A., Steuer, R., and Červený, J. (2019). Quantitative insights into the cyanobacterial cell economy. *Elife* **8**.

Supplementary Material

Metabolite interactions in the bacterial Calvin cycle and implications for flux regulation

Sporre, Karlsen, *et al*

List of Supplementary Figures and Tables

Figure S1: Number of detected peptides in every LiP-SMap experiment

Figure S2: Log2 fold change and significance of detected proteins upon reduction and oxidation of the proteome.

Figure S3: Correlation of minimum q value between repeated experiments

Figure S4: Persistence of low concentration interactions in high concentration

Figure S5: Correlation of log2(fold change) of peptides detected in low and high concentration

Figure S6: Number of peptides detected per metabolite-interacting protein compared to non-interacting proteins

Figure S7: Fraction interacting orthologs within functional groups in each organism

Figure S8: Similarity of ortholog interaction patterns (low concentration)

Figure S9: Interactions of Calvin cycle enzymes and selected central carbon metabolism enzymes with metabolites (low concentration)

Figure S10: (separate PDF file) Phylogenetic trees of Calvin cycle enzymes labeled with detected protein-metabolite interactions

Figure S11: Comparison between protein-metabolite interactions and acetylated or propionylated proteins in *Synechocystis*

Figure S12: Log2 fold change and significance of detected proteins in presence of ATP at different Mg^{2+} concentrations

Figure S13: AMP effect on thermal stability of *Synechocystis* (6083) and *Cupriavidus* (H16) F/SBPase

Figure S14: Glyceraldehyde-3-phosphate (GAP) effect on thermal stability of *Synechocystis* F/SBPase at different Mg^{2+} concentrations

Figure S15: NADPH effect on thermal stability of *Synechocystis* (6803) and *Cupriavidus* (H16) F/SBPase

Figure S16: Citrate effect on thermal stability of *Synechocystis* F/SBPase at different Mg^{2+} concentrations

Figure S17: Kinetic profiles of *C. necator* transketolase with added metabolites

Figure S18: Kinetic profiles of *Synechocystis* sp. PCC6803 transketolase with added metabolites

Figure S19: Kinetic profiles of the F/SBPases with added metabolites

Figure S20: Kinetic profile of *Synechocystis* F/SBPase R194H mutant

Figure S21: Distributions of metabolite concentrations of the 5000 fMCSs created by random sampling

Figure S22: Tendency of metabolite concentrations to be associated with more or fewer stable states

Figure S23: Statistically testing the differences in metabolite concentration distributions with most stable states between the model variants

Figure S24: Flux control coefficients for all reactions in the model.

Table S1: Chosen concentrations for every used metabolite and their most extreme values found in literature

Table S2: All metabolite concentrations found across 7 metabolomics studies

Table S3: Changes in transketolase kinetic parameters in the presence of metabolites

Table S4: Changes in fructose/sedoheptulose biphosphatase kinetic parameters in the presence of metabolites

Supplemental Dataset S1 (separate data file) List of significantly changed proteins by reduction/oxidation through DTT/DTNB

Supplemental Dataset S2: (separate data file) List of all detected peptides across all LiP-SMap experiments

Supplemental Dataset S3: (separate data file) List of all proteins affected by metabolites in all four microbes, with indicated KEGG pathways

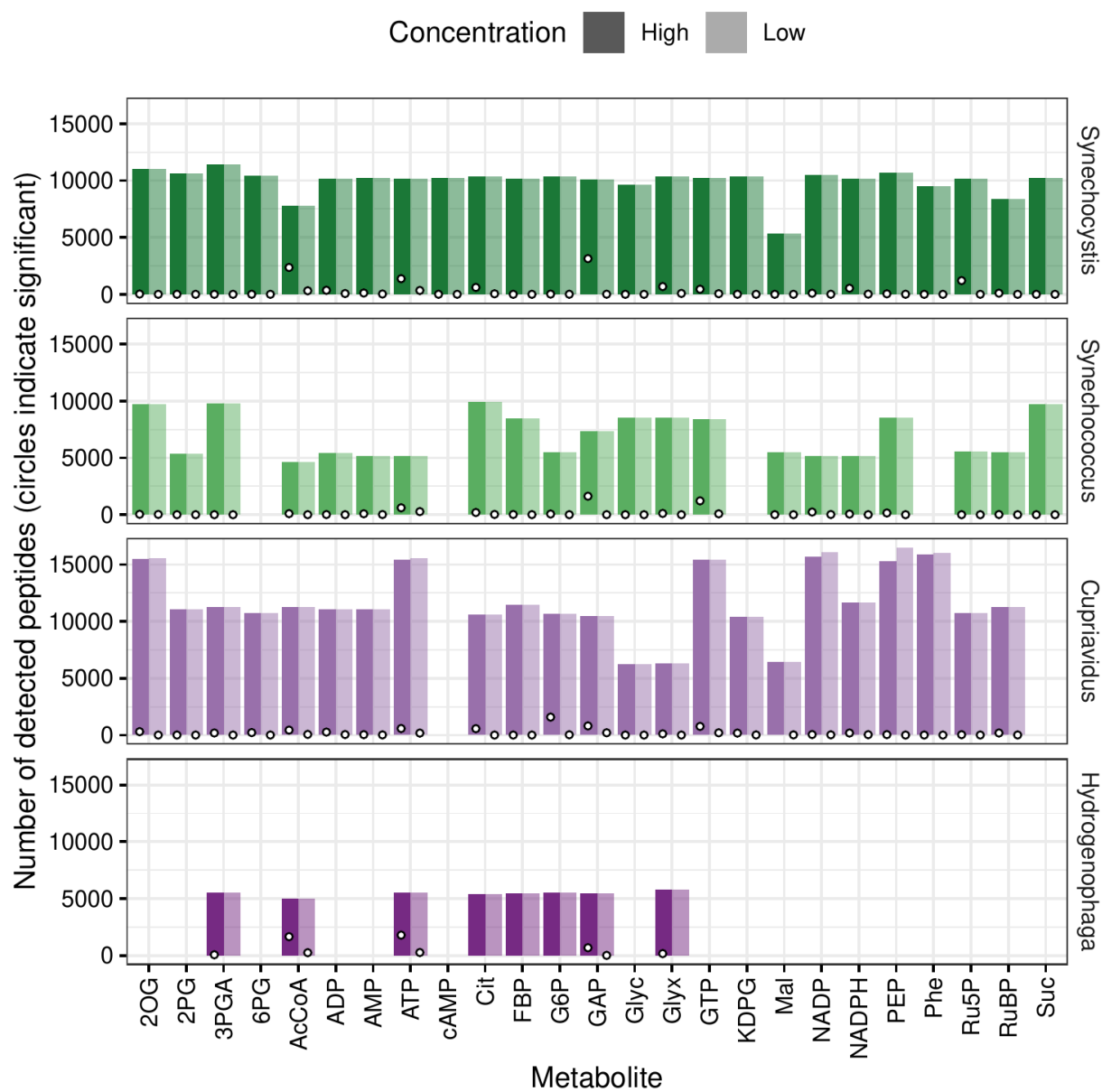


Figure S1. Number of detected peptides in every LiP-SMap experiment.

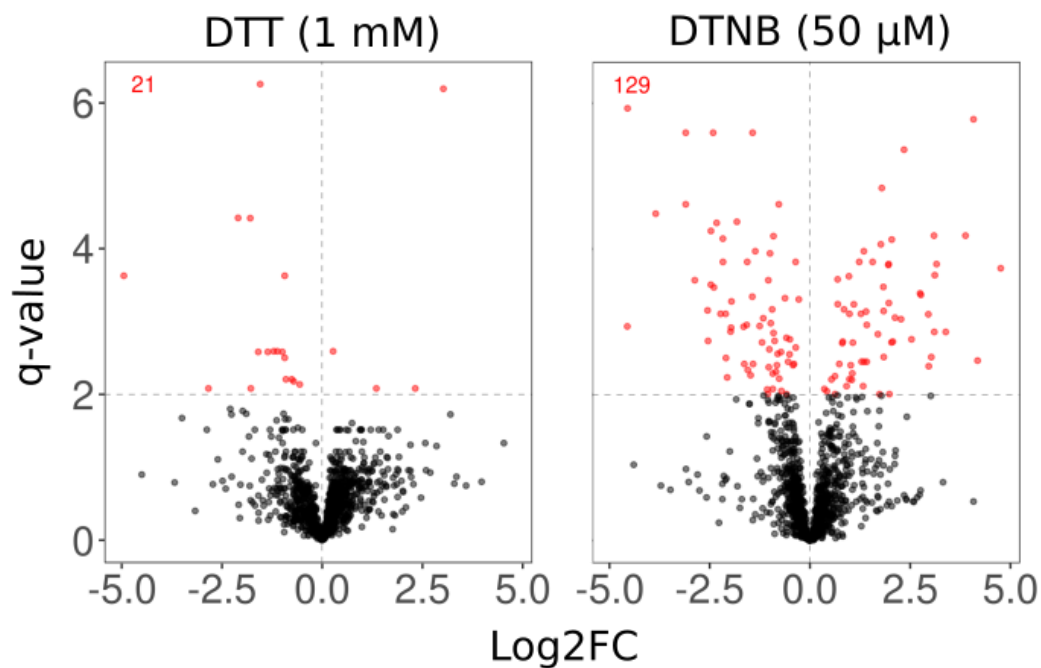


Figure S2. Log2 fold change and significance of detected proteins upon reduction and oxidation of the proteome. DTT and DTNB were used on the proteome of *Synechocystis sp. PCC6803* as reductive and oxidative agents, respectively and compared to an untreated proteome. Each protein detected in both treated and untreated samples are represented by one dot with significantly ($q < 0.01$) changed proteins in red.

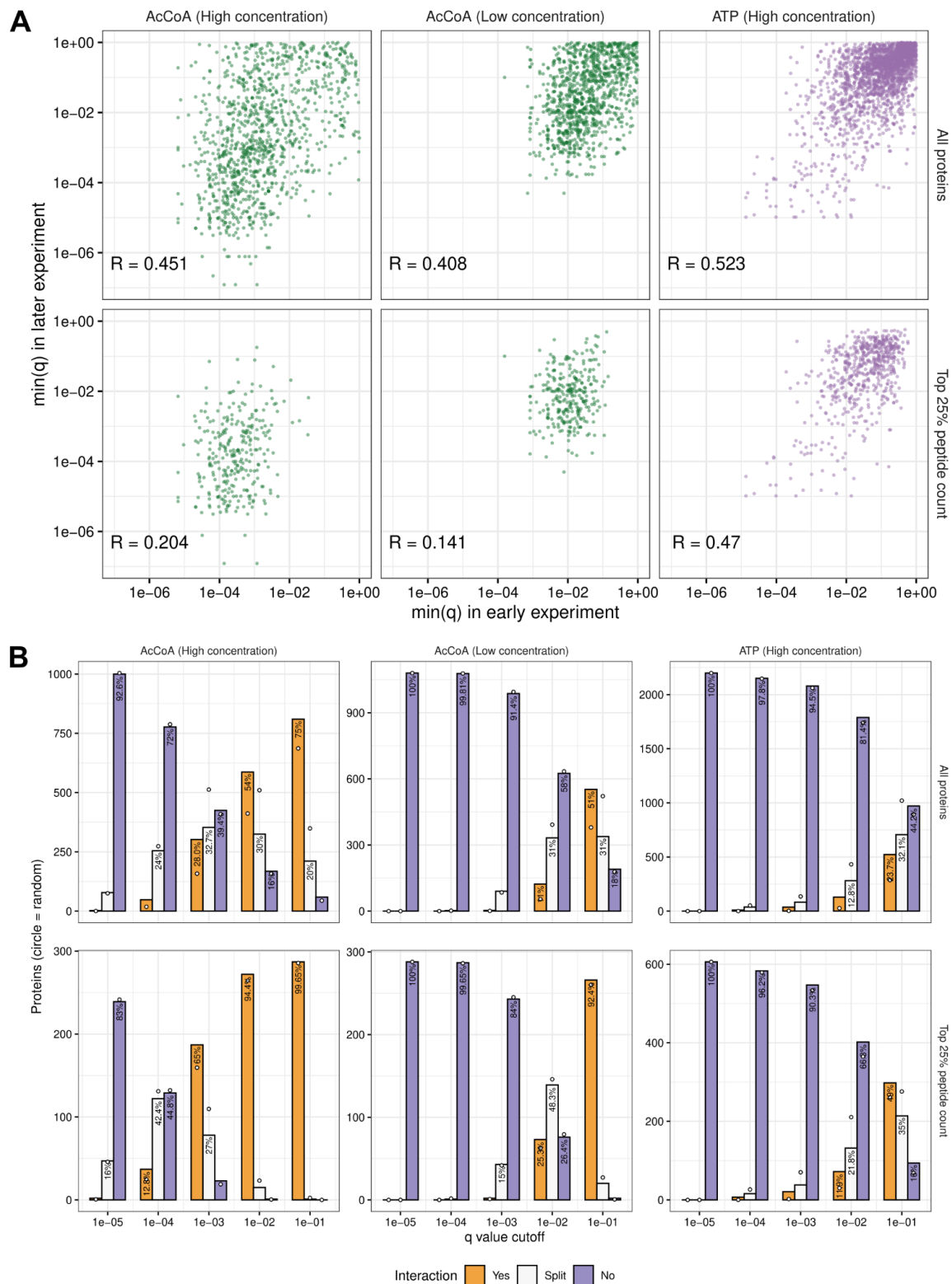
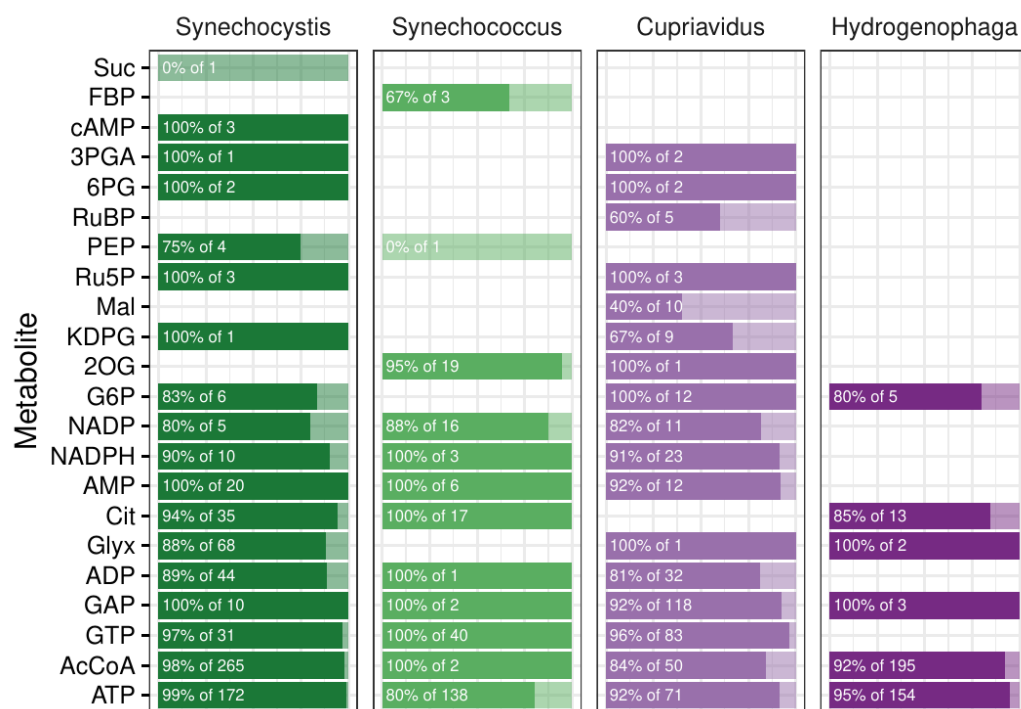


Figure S3. Correlation of minimum q value (A) and agreement of interaction classification (B) between repeated experiments. First, correlation between experiments was assessed (A). The minimum q value for peptides in each protein was correlated (Spearman method) for

proteins detected in both of two consecutive experiments (“early” and “later”) using high and low concentration of acetyl-CoA (AcCoA) and high concentration of ATP. Logarithmic scales are used to display the minimum q values of each protein (points). Correlation was performed for all proteins and for proteins within the top 25% based on detected peptide count. Proteins were classified as interacting if having at least one peptide with a q value lower than the cutoff (x-axis). Second, agreement between experiments was assessed (B). Protein-metabolite interaction classification between two consecutive experiments, using high and low concentration of acetyl-CoA (AcCoA) and high concentration of ATP, was evaluated as agreeing on interaction (“Yes”; both experiments passed the q value cutoff), disagreeing (“Split”; only one experiment passed the q value cutoff), or agreeing on no interaction (“No”; neither experiment passed the q value cutoff). The number of proteins within each class of interaction (y-axis) is displayed as bars labeled by the percentage of proteins within each group of three bars (unless < 10%). The frequency of proteins classified as interacting or not was calculated within each experiment and then used to calculate the expected frequency of agreement classes (“Yes”, “Split”, or “No”) if those were overlapping just by random (circles). Note that ideally two experiments would be in total agreement (no “Split” proteins). Agreement was evaluated for all proteins and for proteins within the top 25% based on detected peptide count.



Persistence of low concentration interactions in high concentration

Figure S4. Persistence of low concentration interactions in high concentration. Opaque bars indicate the fraction of low concentration interactions that were detected both in the low concentration and high concentration experiments, while transparent bars indicate interactions that were only detected in the low concentration experiments. Metabolites are ordered by the total number of interactions. Metabolites without low concentration interactions are excluded.

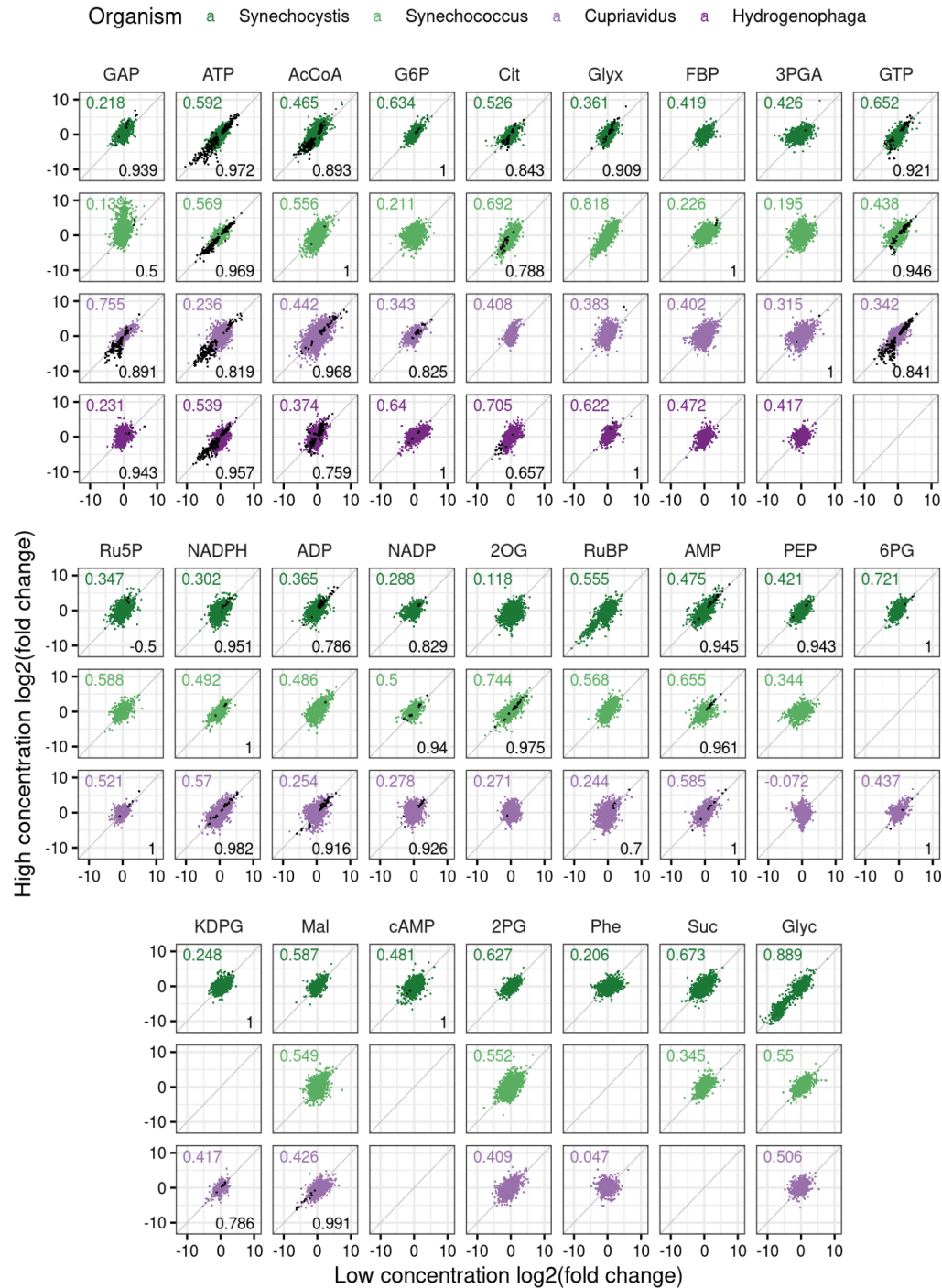


Figure S5. Correlation of log2(fold change) of peptides detected in low and high concentration. Spearman correlation was used to quantify agreement in peptide fold change between low and high concentration experiments. Colored points show peptides that were not significant in any concentration, while black points show peptides significant in both concentrations.

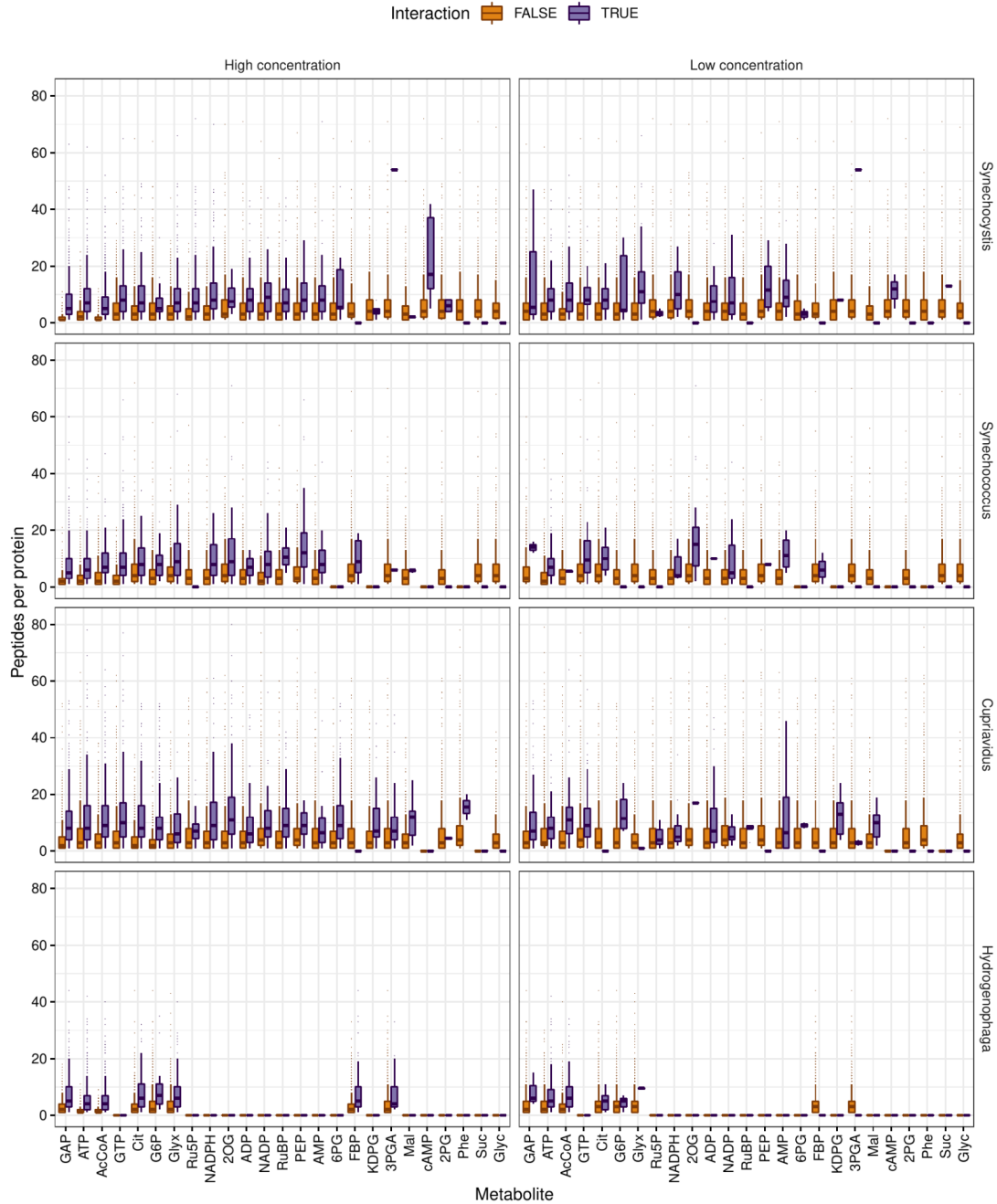


Figure S6. Number of peptides detected per metabolite-interacting protein compared to non-interacting proteins. Proteins were classified as not having interaction or having interaction with the tested metabolites, *i.e.* “Interaction FALSE” and “Interaction TRUE”. Interaction means that at least one peptide was significantly changed in abundance in presence of the metabolite ($q < 0.01$). The y-axis indicates the number of peptides detected per protein summarized as box plots. The plots are split by high and low concentration of the interacting metabolite (columns) and by organism (rows).

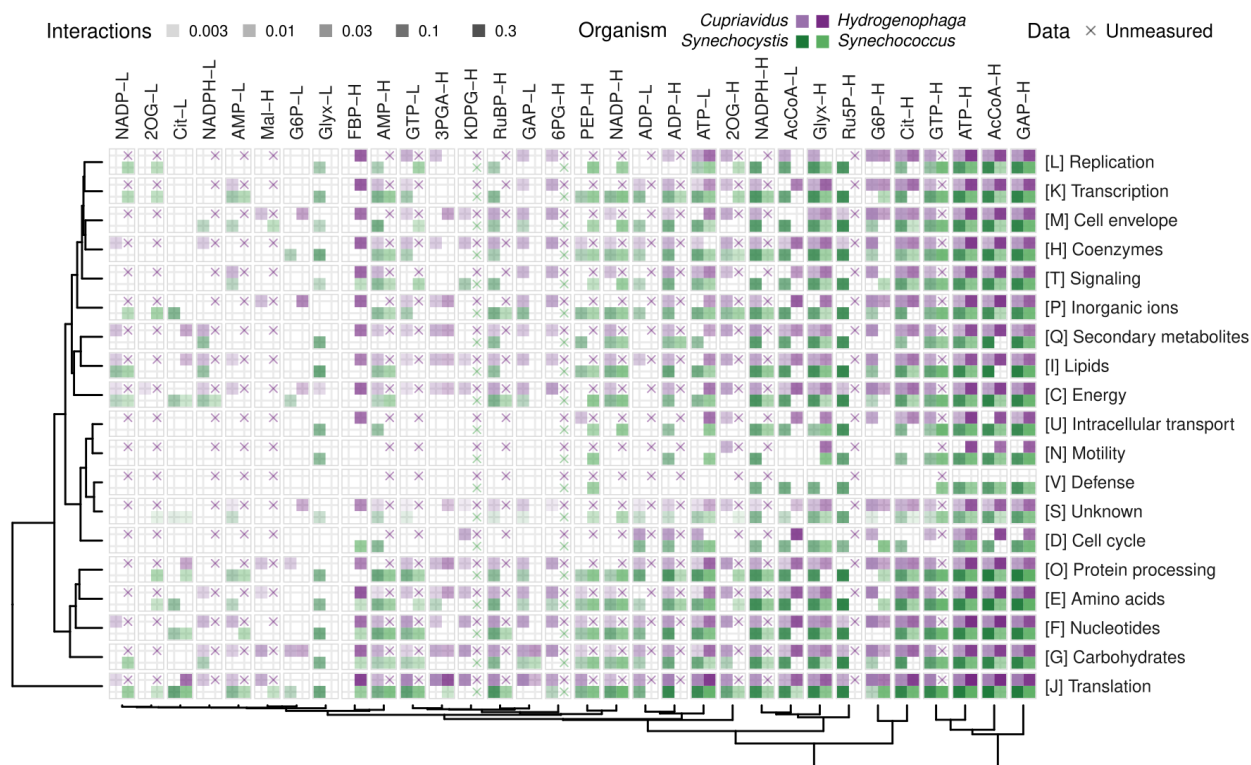


Figure S7. Fraction interacting orthologs within functional groups in each organism. If at least one sequence per ortholog family interacted with a metabolite at low (L) or high (H) concentration (heatmap columns), that ortholog was considered to be interacting. Interactions were then summarized per functional group (heatmap rows) and normalized by the total number of orthologs in that group. Dendrograms illustrate the clustering patterns of rows and columns based on Euclidean distance and the Ward.D2 algorithm. Interaction fractions in all four organisms contributed both to rows and columns. A cross indicates that the particular condition was not measured.

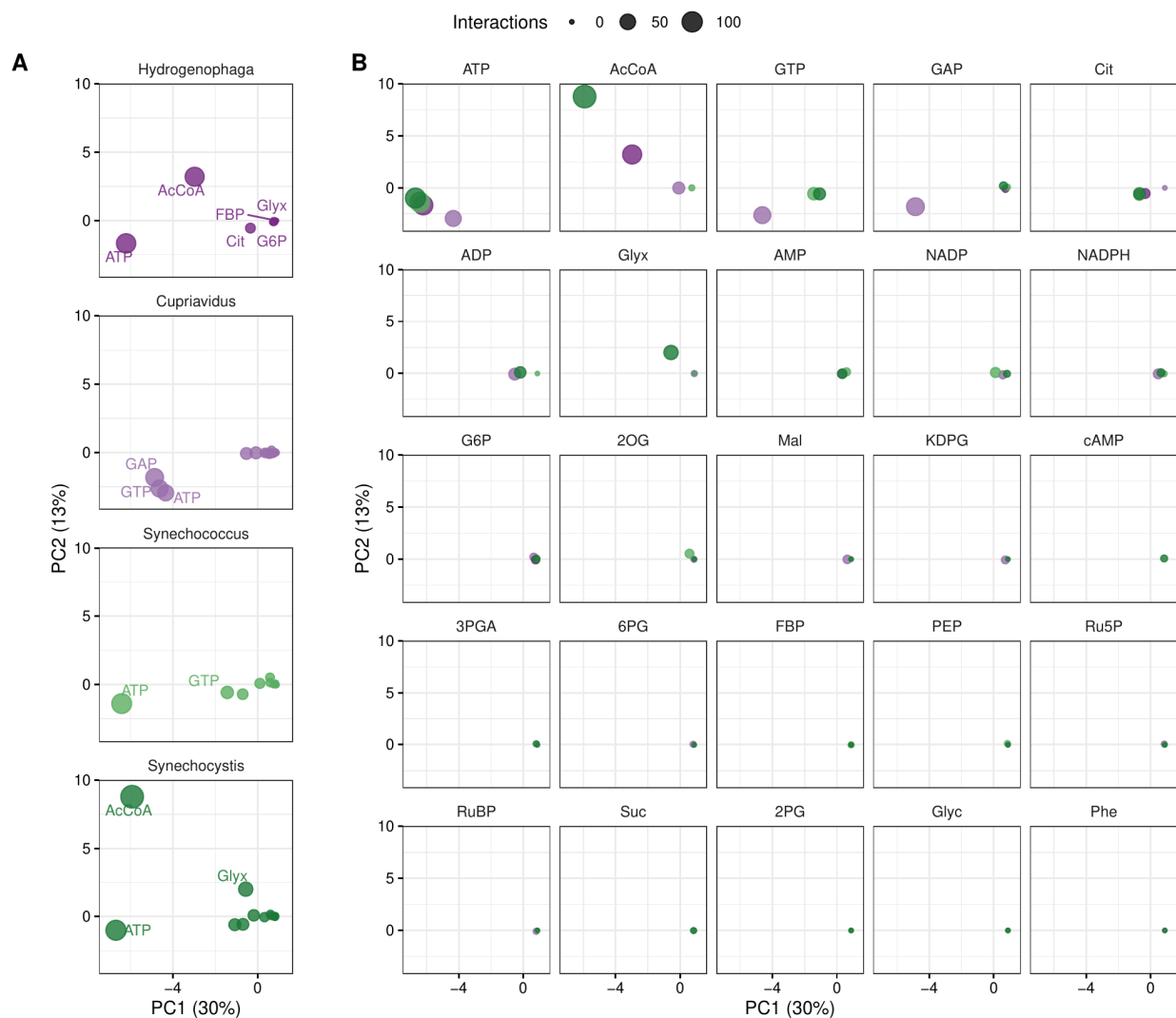


Figure S8. Similarity of ortholog interaction patterns (low concentration). Principal components were calculated from the presence or absence of interaction with each of 321 orthologs (see Materials and Methods). All data points shown here are from the same principal component analysis, but split per organism (A) or metabolite (B) to reduce overplotting. Percentages indicate the fraction of the total variance captured by the principal components.

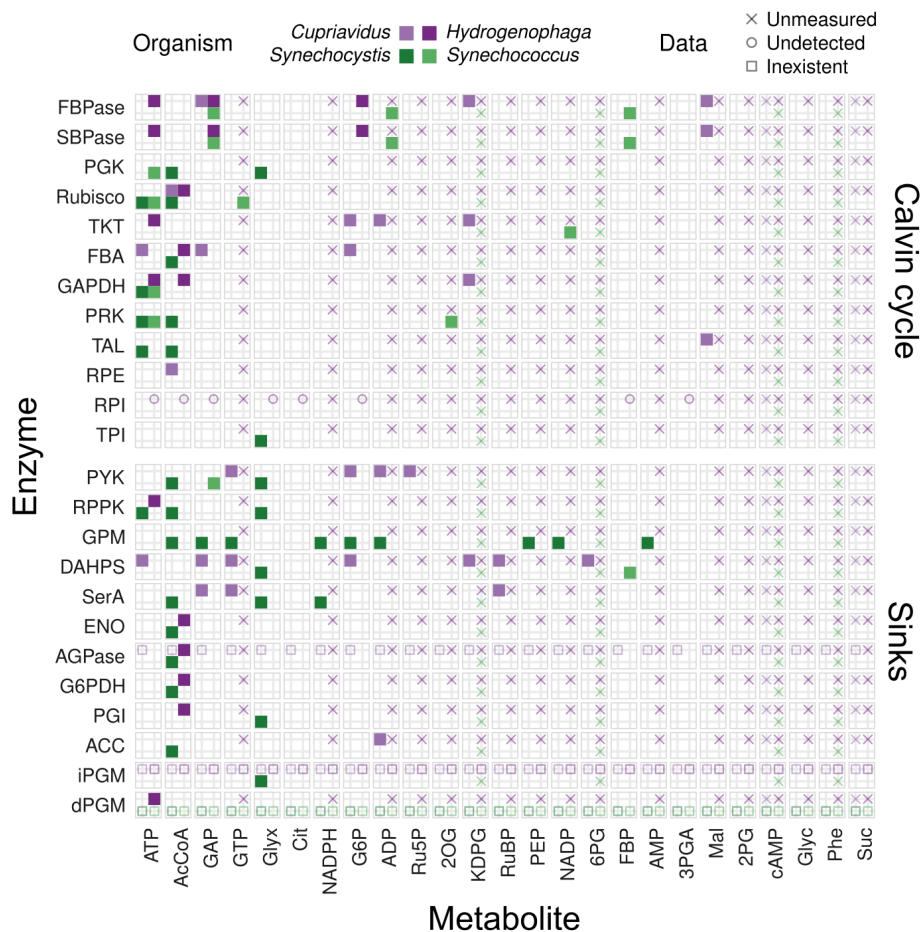


Figure S9. Interactions of Calvin cycle enzymes and selected central carbon metabolism enzymes with metabolites (low concentration). Interactions between metabolites (columns) at low concentration and enzymes (rows) identified by KEGG EC number annotation are shown for each organism by tiles filled with the corresponding color. A blank tile indicates that the interaction was not detected, while missing protein data is explained by a symbol. A cross indicates that the particular condition was not measured, a circle indicates that no proteins were detected, and a square indicates that there was no such enzyme in the corresponding genome. AGPase, ADP-glucose synthase (EC 2.7.7.27); DAHPS, DAHP synthase (EC 2.5.1.54); dPGM, 2,3-diphosphoglycerate-dependent phosphoglycerate mutase (EC 5.4.2.11); ENO, Enolase (EC 4.2.1.11); FBA, Fructose-bisphosphate aldolase (EC 4.1.2.13); FBPase, Fructose-1,6-bisphosphatase (EC 3.1.3.11); G6PDH, Zwf (EC 1.1.1.49); GAPDH, Glyceraldehyde 3-phosphate dehydrogenase (EC 1.2.1.12, 1.2.1.13, 1.2.1.59); GPM, Phosphoglucomutase (EC 5.4.2.2); iPGM, 2,3-diphosphoglycerate-independent phosphoglycerate mutase (EC 5.4.2.12); PGI, Phosphoglucoisomerase (EC 5.3.1.9); PGK, Phosphoglycerate kinase (EC 2.7.2.3); PRK, Phosphoribulokinase (EC 2.7.1.19); PYK, Pyruvate kinase (EC 2.7.1.40); RPE, Ribulose-phosphate 3-epimerase (EC 5.1.3.1); RPI, Ribose 5-phosphate isomerase (EC 5.3.1.6); RPPK, Ribose-5-phosphate pyrophosphokinase (EC 2.7.6.1); Rubisco, Ribulose-bisphosphate carboxylase (EC 4.1.1.39); SBPase, Sedoheptulose-1,7-bisphosphatase (EC 3.1.3.37); SerA, Phosphoglycerate dehydrogenase (EC 1.1.1.95); TAL, Transaldolase (EC 2.2.1.2); TKT, Transketolase (EC 2.2.1.1); TPI, Triose-phosphate isomerase (EC 5.3.1.1).

<Separate PDF file>

Figure S10. Phylogenetic trees of Calvin cycle enzymes labeled with detected protein-metabolite interactions. Each tree is based on fewer than 1 000 representative sequences and all sequences from the four organisms in this study, which belong to KEGG ortholog (KO) families catalyzing steps in the Calvin cycle (see Materials and Methods). The ring indicates organism group; Kingdom for eukaryotes, and phylum for bacteria and archaea, except for Proteobacteria, which are divided into classes. Organism groups that were too small to warrant their own color were grouped into the “Other” categories. Each tree is titled with the KO ID, gene names, enzyme names, and Enzyme Commission number. Sequences from the four organisms in this study are indicated by symbols and text with an organism-specific color. These sequences show additional information in the text boxes; The top text line indicates the UniProt ID, the gene name, and the locus ID (in parentheses). The bottom text line indicates all metabolites with which the enzyme has at least one significantly interacting peptide at low or high concentration. Scale bars indicate substitutions per site.

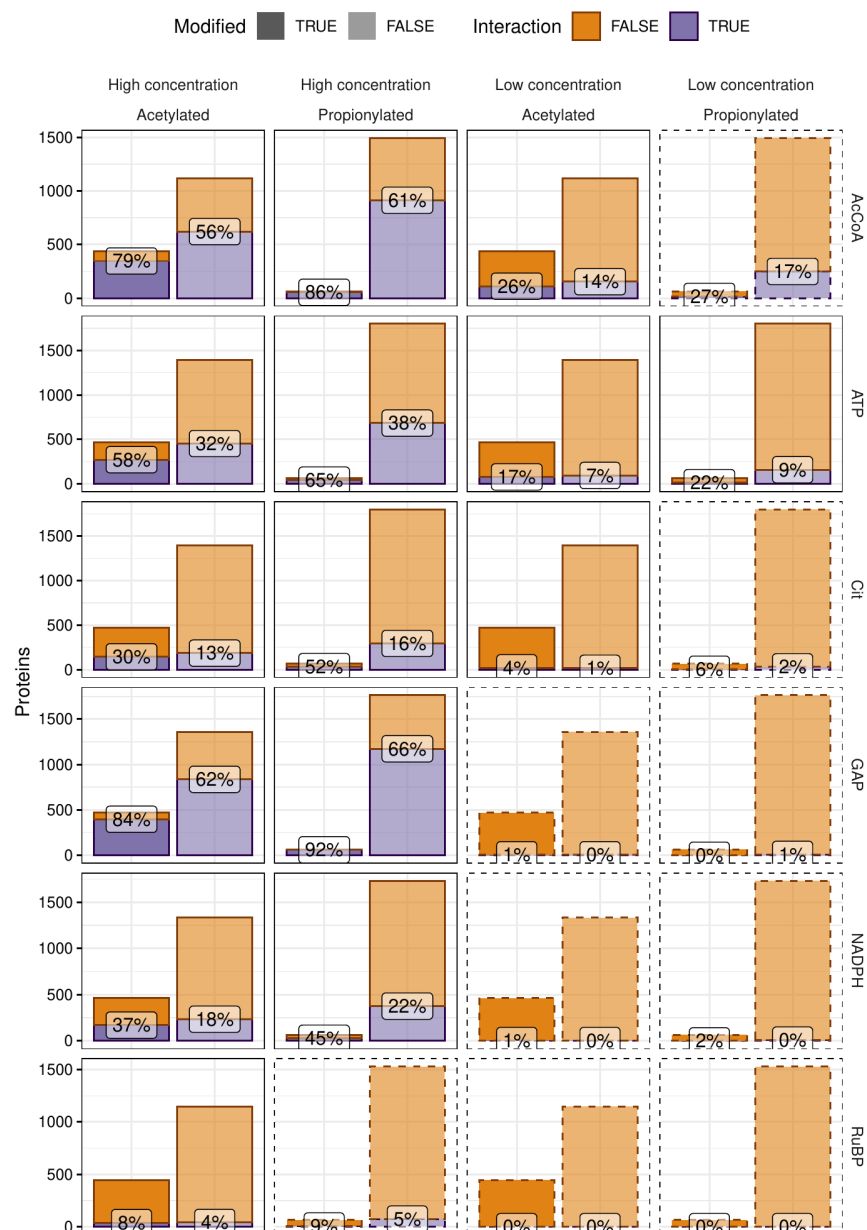


Figure S11. Comparison between protein-metabolite interactions and acetylated or propionylated proteins in *Synechocystis*. Proteins in *Synechocystis* were divided into modified (opaque stacked bars on the left) and unmodified (transparent stacked bars on the right) categories based on post-translational acetylation (Mo et al. 2015) or propionylation (Yang, Huang, and Ge 2019). Labels indicate the fraction (%) metabolite-interacting proteins in each stack of bars. The fractions of modified and unmodified proteins that also interacted with high or low concentration acetyl-CoA (AcCoA), ATP, citrate (Cit), glyceraldehyde 3-phosphate (GAP), NADPH, or ribulose 1,5-bisphosphate (RuBP) were compared with Fisher's exact test, revealing significant overlaps ($p < 0.01$) where panels have a solid frame. A dashed frame indicates no significant overlap between post-translational modification and protein-metabolite interaction.

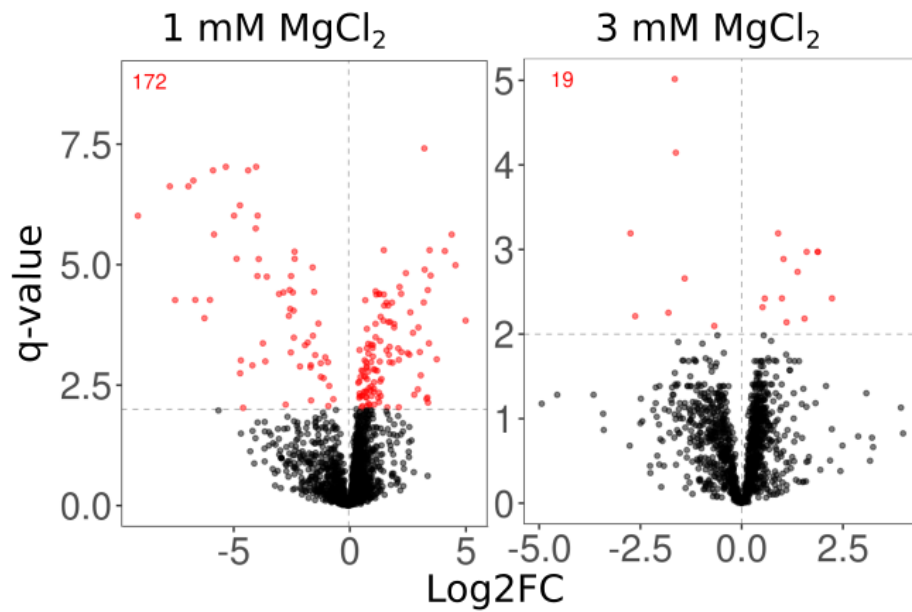


Figure S12. Log2 fold change and significance of detected proteins in presence of 2mM ATP at different Mg^{2+} concentrations. The extracted proteome of *Synechocystis sp. PCC6803* was treated with 2 mM ATP and either 1 or 3 mM MgCl_2 and compared to a sample without ATP but with the same concentration MgCl_2 . Each protein detected in both treated and untreated samples are represented by one dot with significantly ($q < 0.01$) changed proteins in red. The effect of ATP treatment is mitigated by an increased MgCl_2 concentration.

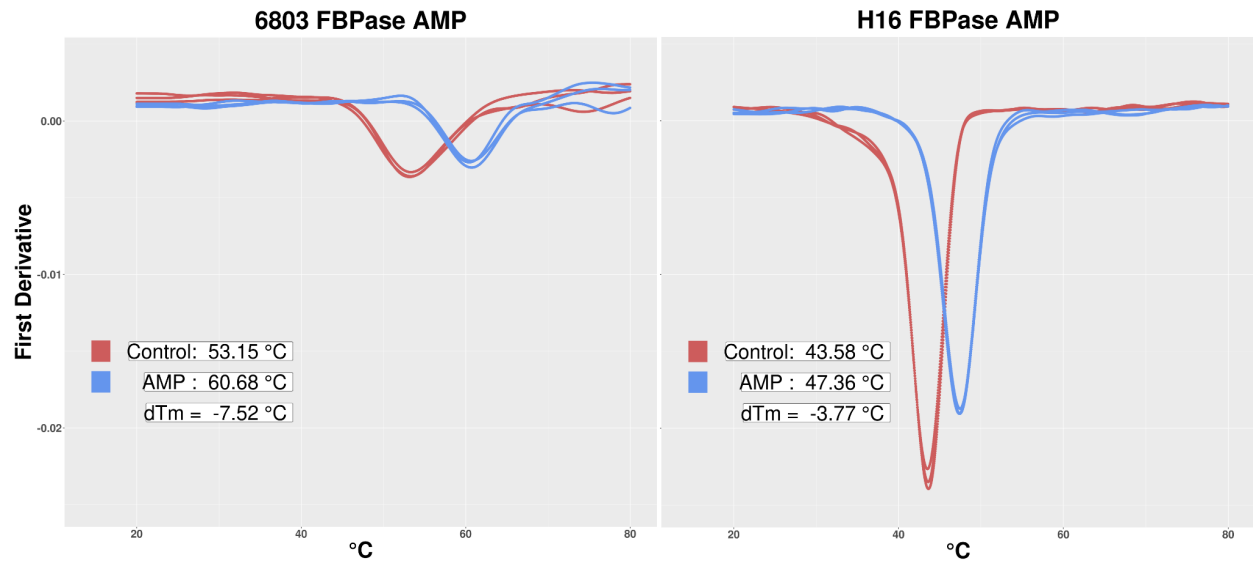


Figure S13. AMP effect on thermal stability of *Synechocystis* (6083) and *Cupriavidus* (H16) F/SBPase. Curves indicate denaturation of F/SBPase over a temperature gradient of 1 °C/min. Y-axis shows the change in the ratio of protein autofluorescence (350 nm/330 nm), and minimum values indicate the melting temperature (T_m) at which half of the enzymes are denatured.

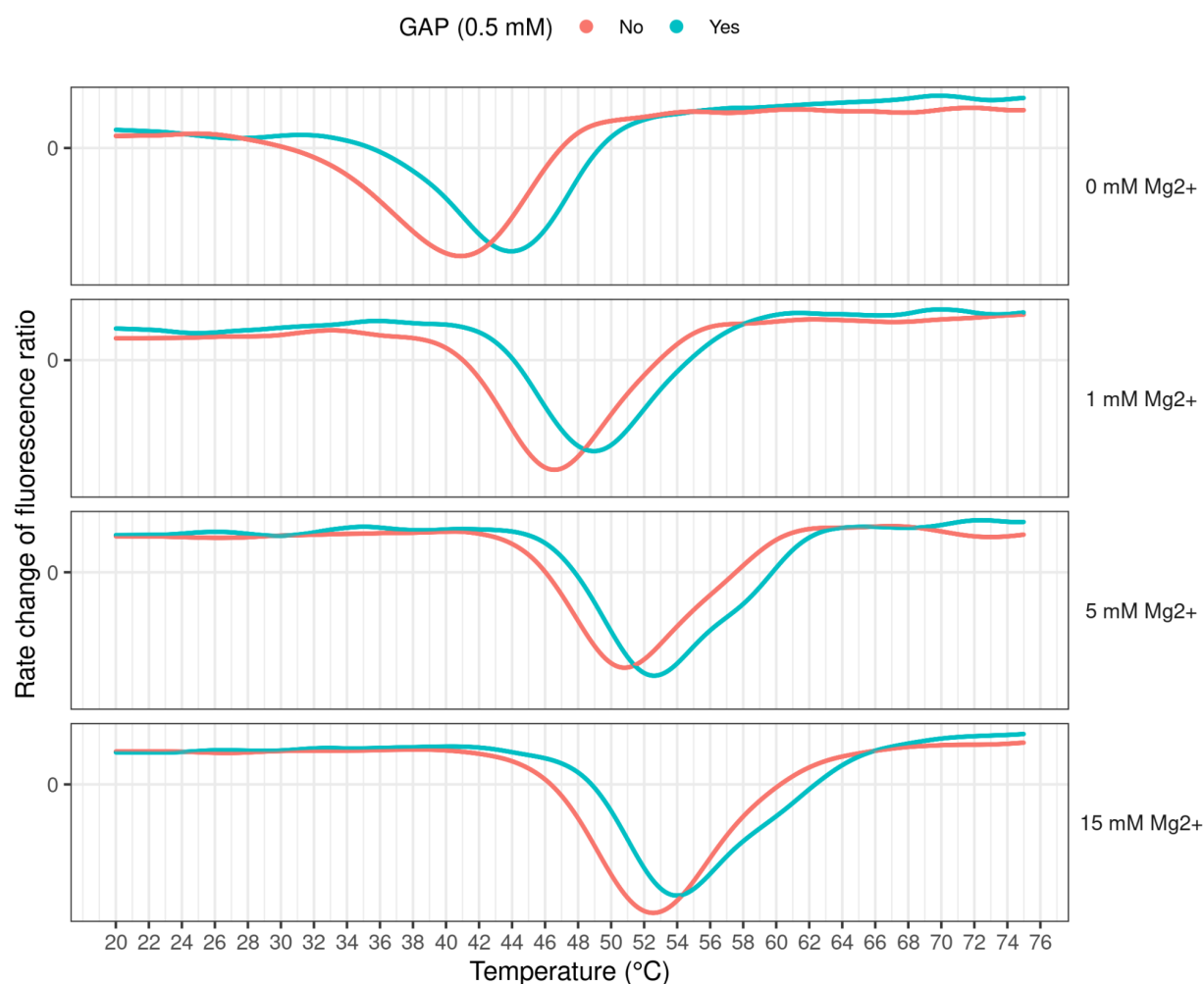


Figure S14. Glyceraldehyde-3-phosphate (GAP) effect on thermal stability of *Synechocystis* F/SBPase at different Mg^{2+} concentrations. Curves indicate denaturation of F/SBPase over a temperature gradient of 1 °C/min. Y-axis shows the change in the ratio of protein auto fluorescence (350 nm/330 nm), and minimum values indicate the melting temperature (T_m) at which half of the enzymes are denatured.

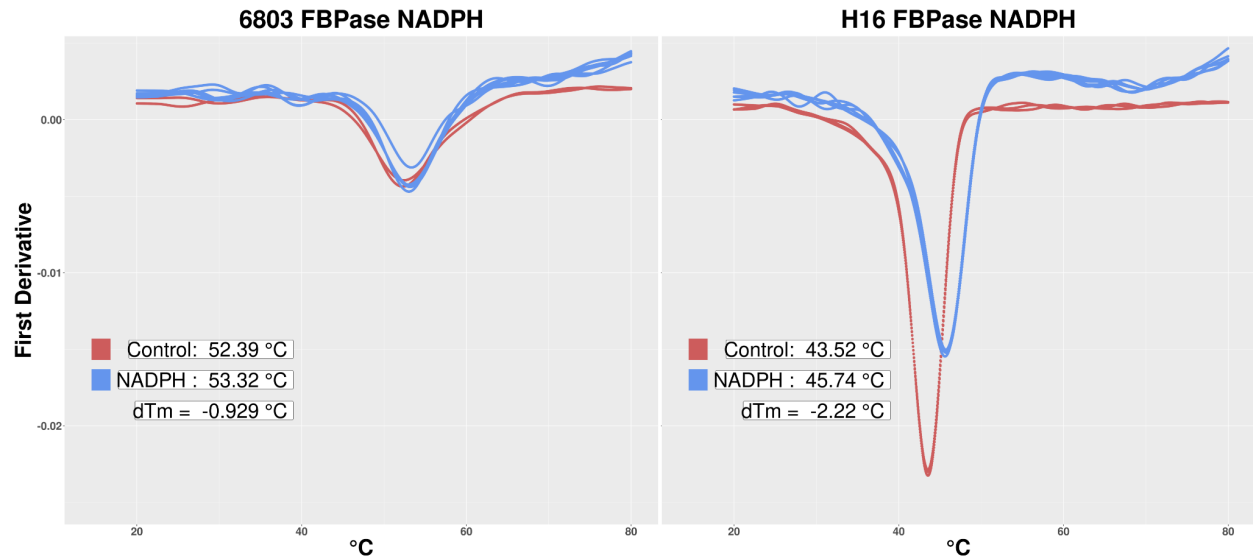


Figure S15. NADPH effect on thermal stability of *Synechocystis* (6803) and *Cupriavidus* (H16) F/SBPase. Curves indicate denaturation of F/SBPase over a temperature gradient of 1 °C/min. Y-axis shows the change in the ratio of protein auto- fluorescence (350 nm/330 nm), and minimum values indicate the melting temperature (T_m) at which half of the enzymes are denatured.

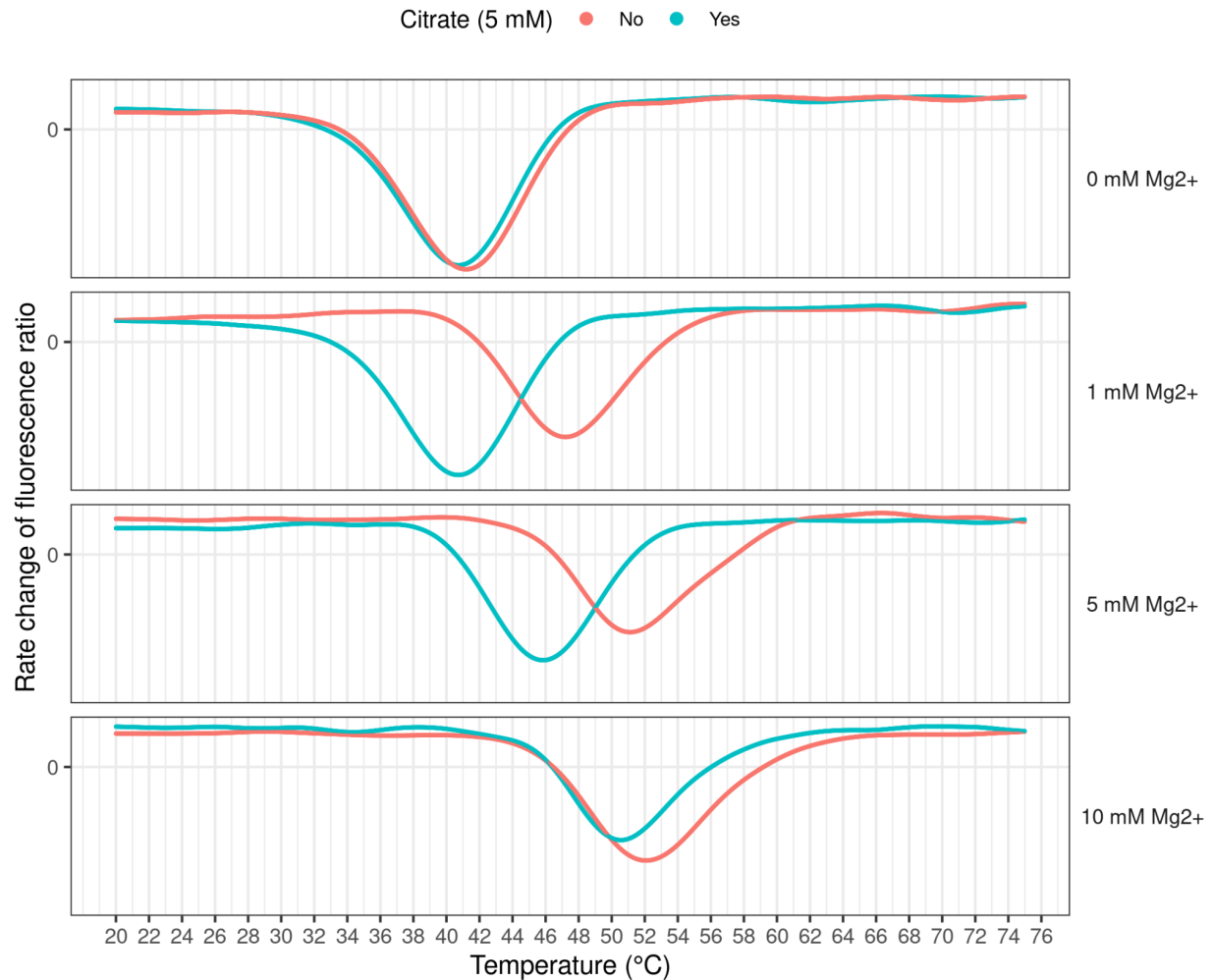


Figure S16. Citrate effect on thermal stability of *Synechocystis* F/SBPase at different Mg^{2+} concentrations. Curves indicate denaturation of F/SBPase over a temperature gradient of 1 °C/min. Y-axis shows the change in the ratio of protein auto- fluorescence (350 nm/330 nm), and minimum values indicate the melting temperature (T_m) at which half of the enzymes are denatured. Addition of 5 mM citrate results in a T_m shift that corresponds to a ~1:1 chelation of Mg^{2+} .

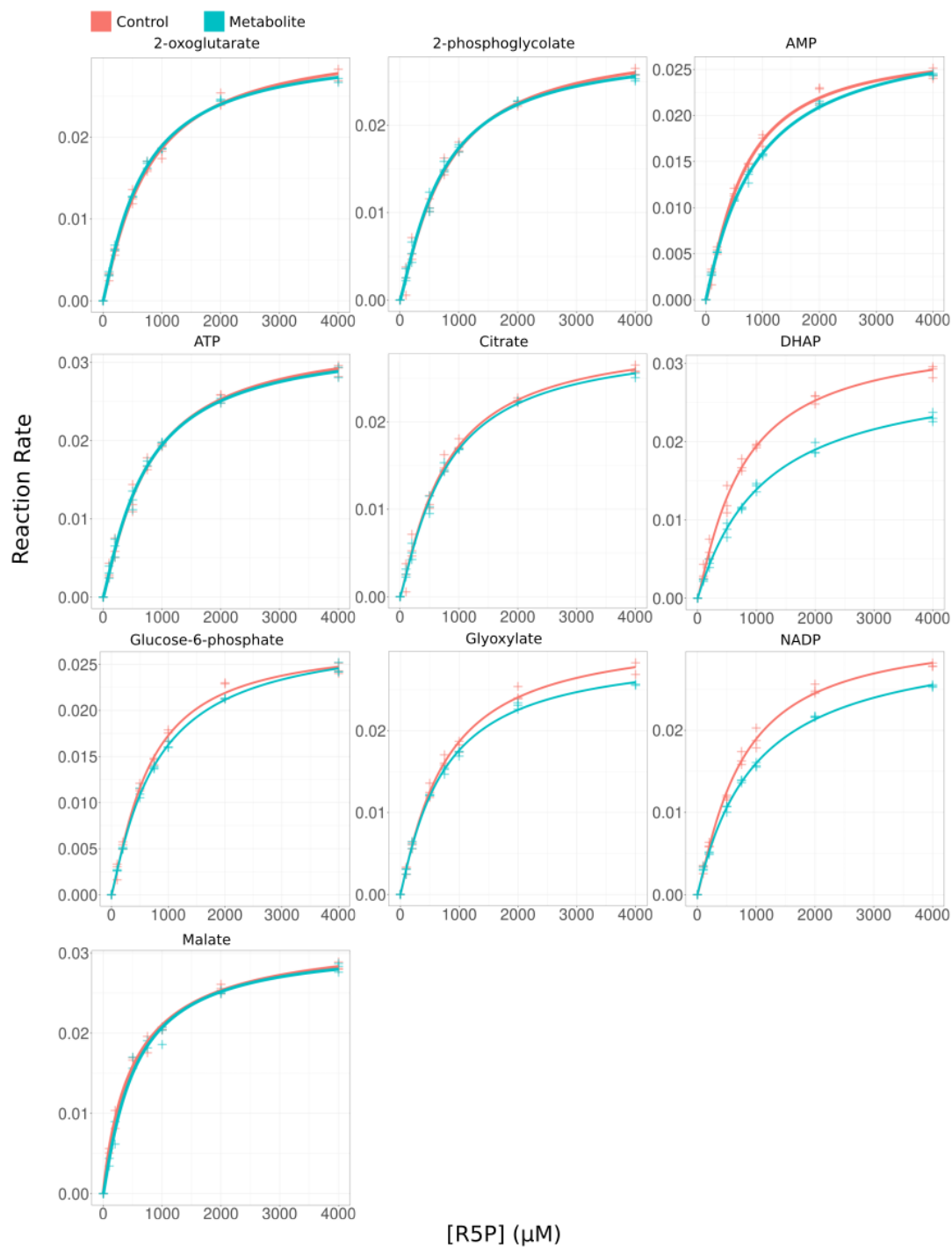


Figure S17. Kinetic profiles of *C. necator* transketolase with added metabolites. Each kinetic profile was characterized by calculating reaction rates for eight different substrate concentrations in triplicates. A new untreated enzyme control was run in parallel with each treated sample. No standard curves were used and as such the reaction rate was never quantified.

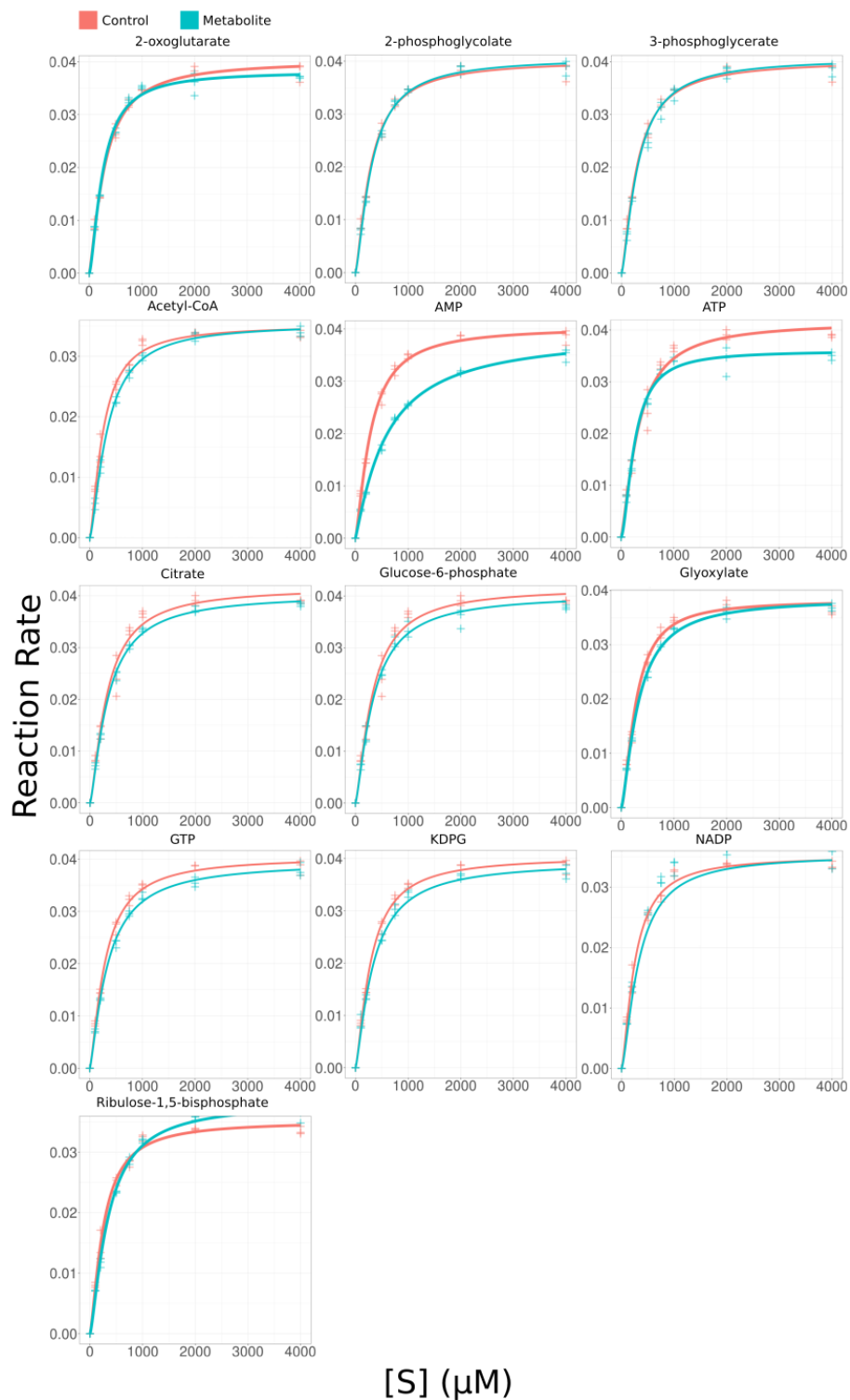


Figure S18. Kinetic profiles of *Synechocystis* sp. PCC6803 transketolase with added metabolites. Each kinetic profile was characterized by calculating reaction rates for eight different substrate concentrations in triplicates. A new untreated enzyme control was run in parallel with each treated sample. No standard curves were used and as such the reaction rate was never quantified.

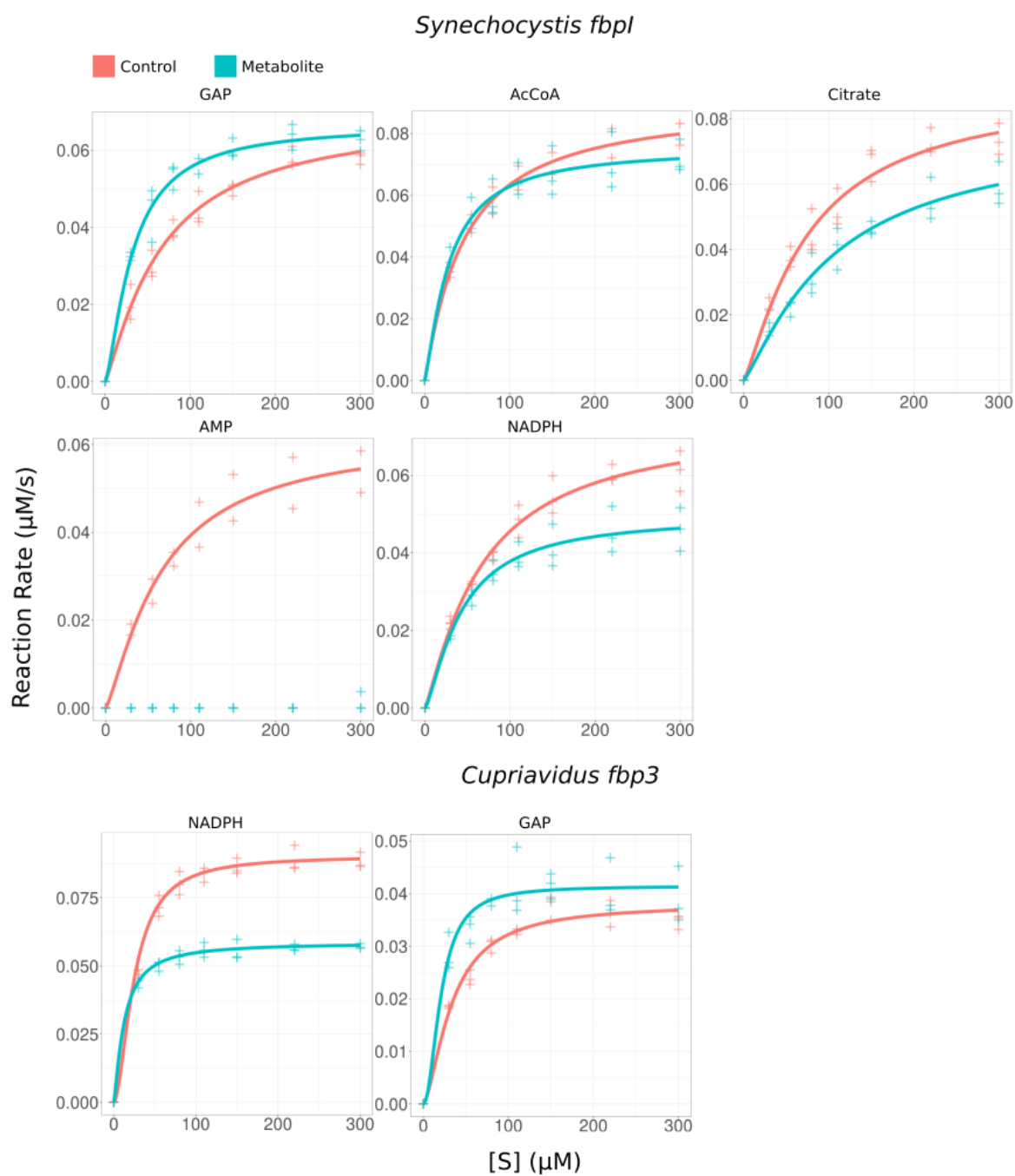


Figure S19. Kinetic profiles of the F/SBPases with added metabolites. Each kinetic profile was characterized by calculating reaction rates for eight different substrate concentrations in triplicates. A new untreated enzyme control was run in parallel with each treated sample.

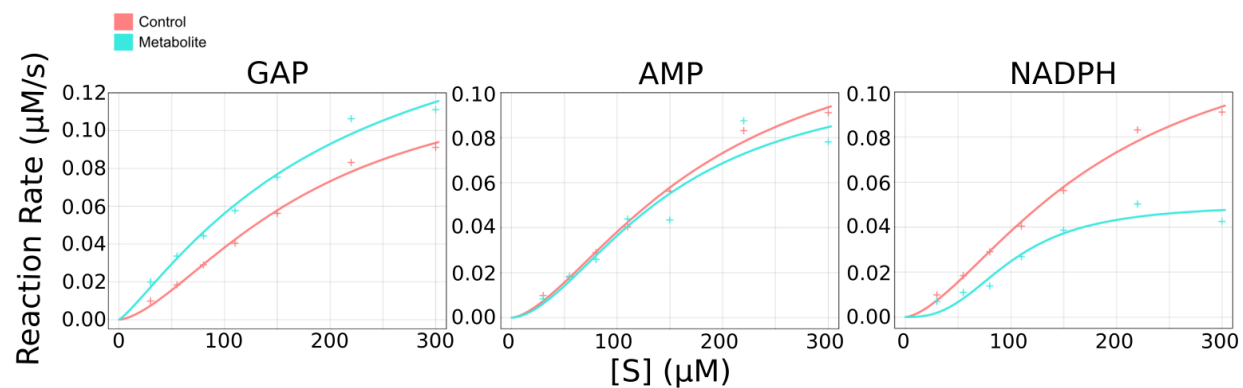


Figure S20. Kinetic analysis of the F/SBPase R194H from *Synechocystis*. The enzyme is AMP insensitive, but retains sensitivity to GAP and NADPH., consistent with binding sites of GAP and NADPH as detected by LiP being distinct from AMP.

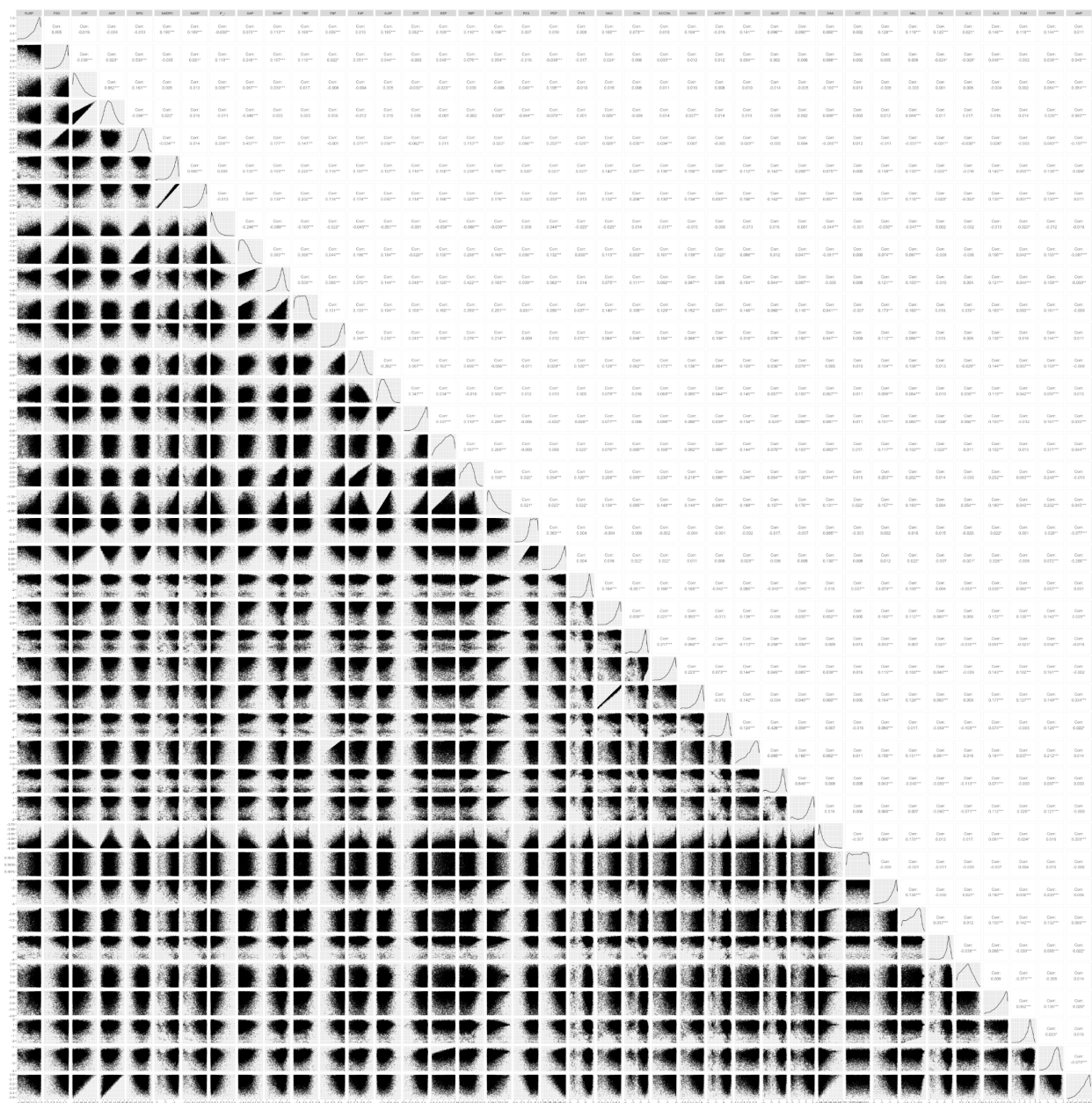


Figure S21. Distributions of metabolite concentrations of the 5000 fMCSs created by random sampling. Metabolite concentrations were randomly sampled via a *hit-and-run* approach as described in the method section, resulting in 5000 thermodynamically feasible metabolite concentration sets.

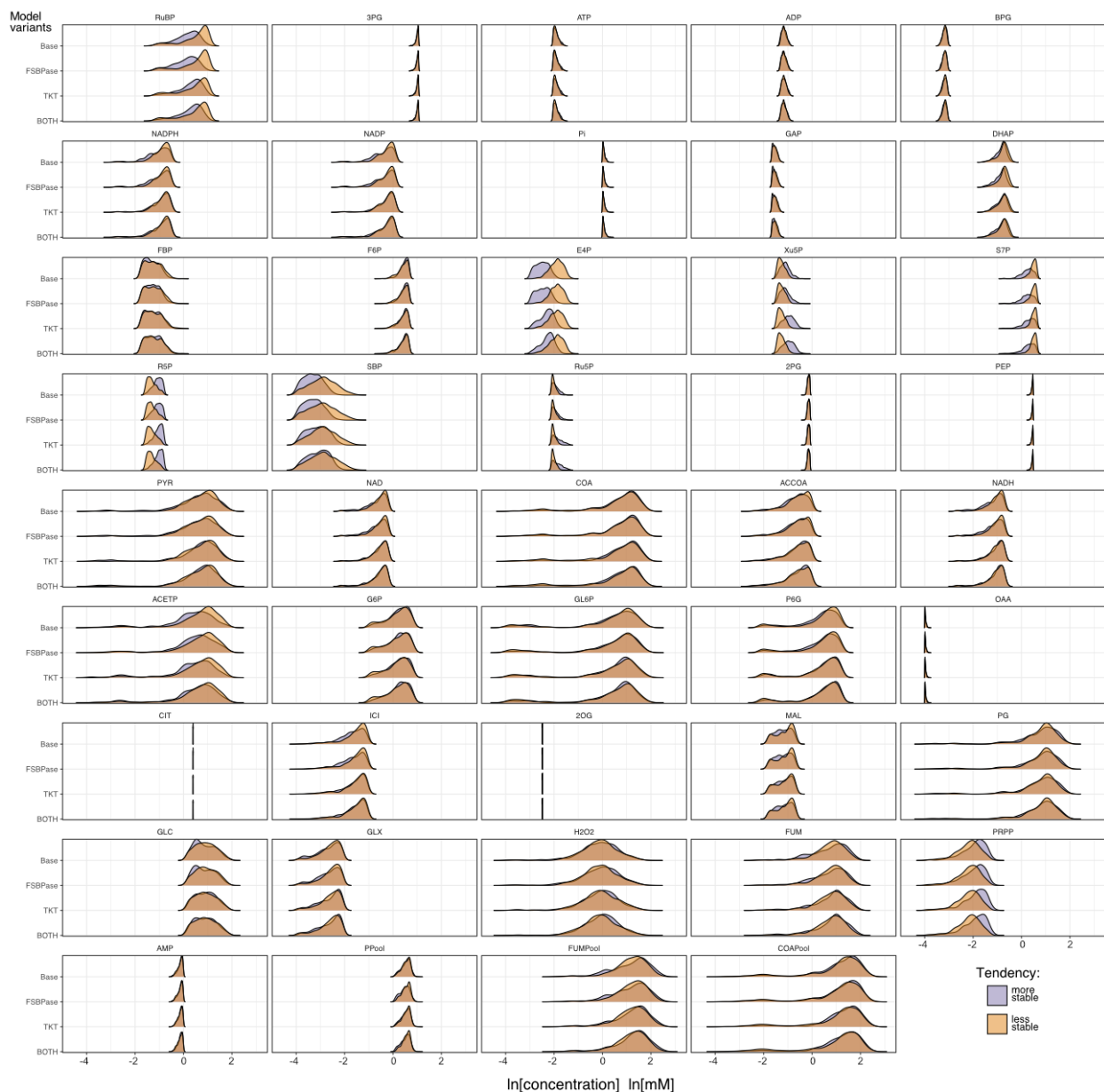


Figure S22. Tendency of metabolite concentrations to be associated with more or fewer stable states. Metabolite concentration distributions corresponding to the top and bottom 10% number of stable states for all four model variants (“Base”, “FSBPase”, “TKT”, “Both”). The narrow concentration ranges for CIT and 2OG taken from (Asplund-Samuelsson, Janasch, and Hudson 2018) make the corresponding plots look line-like.

	Model variant comparison					
	Base Vs FBPase	Base Vs TKT	Base Vs Both	TKT Vs Both	FSBPases Vs Both	FSBPase Vs TKT
AMP	1	0.981	0.725	0.92	0.893	0.977
PRPP	0.985	0.262	0.227	1	0.086	0.133
FUM	0.964	0.198	0.028	0.923	0.031	0.284
H2O2	0.534	0.424	0.147	0.995	0.687	0.699
GLX	0.979	0.074	0.106	1	0.051	0.056
GLC	0.999	0.027	0.204	0.966	0.284	0.051
PG	1	0.976	0.893	1	0.997	0.998
MAL	0.994	0.149	0.477	0.999	0.641	0.433
2OG	0.952	0.483	0.626	1	0.446	0.273
ICI	0.921	0.002	0.005	1	0.01	0.009
CIT	1	0.963	0.857	1	0.796	0.93
OAA	0.136	0.139	0.78	0.943	0.721	0.999
P6G	0.634	0.005	0.001	1	0.012	0.049
GL6P	0.27	0.143	0.085	1	0.235	0.343
G6P	0.927	0.92	0.922	0.95	0.767	0.992
ACETP	0.014	0.313	0.001	0.117	0.334	0.108
NADH	0.997	0.001	0	1	0	0
ACCOA	0.801	0.02	0.001	0.875	0.049	0.184
COA	0.954	0.288	0.726	0.969	0.827	0.474
NAD	0.999	0.004	0.001	1	0	0.002
PYR	0.952	0.063	0.171	0.952	0.045	0.028
PEP	1	0.782	0.633	0.999	0.439	0.658
2PG	0.992	0.87	0.549	0.999	0.654	0.997
Ru5P	1	0	0	0.967	0	0
SBP	0.993	0	0	0.481	0	0
R5P	0.994	0.001	0	0.991	0	0
S7P	0.947	0.002	0.007	0.993	0.003	0.001
Xu5P	0.918	0	0	1	0	0
E4P	0.395	0	0	0.629	0	0
F6P	0.995	0.024	0.071	0.998	0.203	0.08
FBP	0.062	0.045	0	0.431	0.05	0.527
DHAP	0.243	0.108	0.2	1	0.031	0.009
GAP	0.737	0.777	0.831	0.926	0.747	0.834
P _i	0.915	0.939	1	0.998	0.727	0.707
NADP	0.243	0	0.001	0.991	0.124	0.047
NADPH	0.121	0	0	0.981	0.027	0.009
BPG	0.388	0.247	0.02	0.534	0.595	0.868
ADP	1	0.043	0.143	0.998	0.288	0.138
ATP	0.985	0.765	0.979	0.838	0.699	0.307
3PG	0.953	0.362	0.914	0.947	0.988	0.576
RuBP	0.236	0	0	1	0	0

Significance
($p < 0.05$)

FALSE
TRUE

Figure S23. Statistically testing the differences in metabolite concentration distributions with most stable states between the model variants. The metabolite concentrations leading to most stable states (top 10%) were tested for statistically significant differences in their distributions between the four model variants (“Base”, “FSBPase”, “TKT”, “Both”) using a two-sided Kolmogorov-Smirnov test, significance at $p < 0.05$.

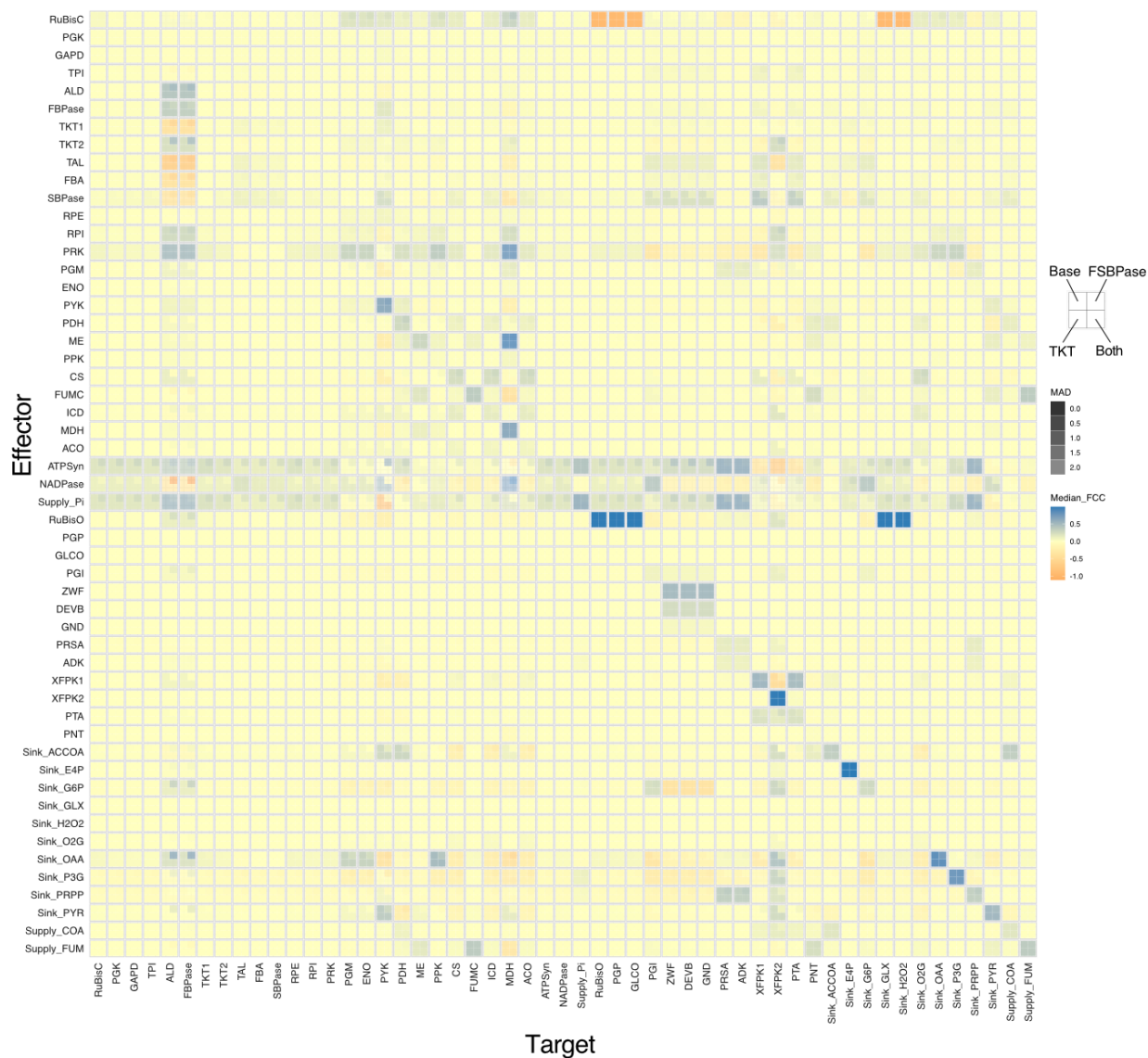


Figure S24. Flux control coefficients for all reactions in the model. Median FCCs and MAD values were calculated over all stable parameter sets for all four model variants as described in the methods section.

Table S1. Chosen concentrations (mM) for every used metabolite and boundary values found in literature.

The metabolite concentrations chosen for the LiP-SMap experiments in mM, the highest and lowest concentration found in literature, in mM (**Table S2**), and the highest and lowest concentrations allowed in the thermodynamically constrained model of Asplund-Samuelsson et al. 2018. In addition to the values shown below, several other reports have shown that metabolite concentrations can vary strongly across different conditions (Lempp et al. 2019; Marcus, Harel, and Kaplan 1983). As such we decided to use similarly high concentrations for our experiments to make sure few metabolite effectors were missed.

Metabolite		Concentration ranges in literature				Chosen concentrations	
Name	KEGG	Literature range lower limit	Literature range upper limit	Modeling range lower limit	Modeling range upper limit	Low	High
2-phosphoglycolate	C00988	0.17	0.17	0.0001	100.0000	0.2	4
2-oxoglutarate	C00026	0.19	3.4	0.0031	2.1200	1	10
3-phosphoglycerate	C00597	1.54	19.02	-	-	2	20
6-phosphogluconate	C00345	0.07	9.58	0.0070	16.3800	1	10
Acetyl-CoA	C00024	0.01	1.54	0.0001	0.9640	1	10
ADP	C00008	0.58	5.26	0.0428	4.1867	1	10
AMP	C00020	0.34	13.4	0.0470	11.2000	1	10
ATP	C00002	0.2	3.06	0.0300	43.4300	2	32
cAMP	C00575	0.34	0.34	-	-	0.5	5
Citrate	C00158	0.17	5.45	0.0240	2.4800	2	20
Fructose-1,6-bisphosphate	C00354	0.17	4.97	0.0163	7.0694	1	10
Glucose-6-phosphate	C00668	0.17	3.4	-	-	1	10
Glyceraldehyde-3-phosphate	C00118	0.17	0.65	0.0001	100.0000	0.5	5
Glycolate	C00160	0.09	0.17	-	-	1	10
Glyoxylate	C00048	0.17	0.17	0.0001	100.0000	1	10
GTP	C00044	0.14	4.87	0.1595	1.0358	1	10
KDPG	C04442	-	-	-	-	0.5	5
Malate	C00149	0.17	6.79	0.0142	2.0602	1	10
NADP	C00006	0.17	2.14	0.0055	1.3200	0.5	5
NADPH	C00005	0.14	0.24	0.0001	49.4100	0.5	5
Phosphoenolpyruvate	C00074	0.51	6.79	0.1700	2.9900	0.5	10
Phenylalanine	C00079	0.12	0.25	0.0151	0.0955	0.5	5
Ribulose-5-phosphate	C00199	0.03	5.09	0.0077	3.8900	1	10
Ribulose-1,5-bisphosphate	C01182	0.05	17.15	0.0001	11.2311	1	10
Sucrose	C00089	-	-	-	-	1	10

Table S2. All metabolite concentrations found across 7 metabolomics studies in mM.

Absolute metabolite concentrations found in literature. All values obtained from articles studying cyanobacteria were converted from μmol per gram cell dry weight to millimolar. This was done by calculating the amount of cell volume per gram dry weight from the values reported by Zavřel et al. for a growth rate of 0.05 h^{-1} (Zavřel et al. 2019). The cell volume was calculated from the cell diameter and multiplied by the cell count per liter culture to obtain the total cell volume per liter culture. This was then divided by the dry weight per liter cell culture, giving the amount of cell volume per dry weight.

Metabolite		E.coli	PCC. 6803					
Name	KEGG	Bennet (2009)	Nishiguchi (2019)	Yoshikawa (2013)	Takahashi (2008)	Shastri (2007)	Hasunuma (2013)	Dempo (2014)
2-phosphoglycolate	C00988	-	-	-	-	0.17	-	-
2-oxoglutarate	C00026	0.44	-	0.71	0.19	3.40	-	-
3-phosphoglycerate	C00597	1.54	12.24	2.26	2.38	10.19	2.21	19.02
6-phosphogluconate	C00345	1.64	0.07	0.15	0.08	0.17	-	9.58
Acetyl-CoA	C00024	0.73	1.54	0.27	-	0.17	0.01	0.70
ADP	C00008	0.56	0.58	1.12	0.85	-	1.87	5.26
AMP	C00020	0.28	-	0.76	0.34	-	1.51	13.40
ATP	C00002	9.63	1.34	13.12	1.02	-	0.20	3.06
cAMP	C00575	0.08	-	-	-	-	0.34	-
Citrate	C00158	0.85	5.45	1.70	0.85	0.17	0.49	3.23
Fructose-1,6-bisphosphate	C00354	15.20	0.51	4.97	0.17	0.17	-	0.42
Glucose-6-phosphate	C00668	-	1.70	2.46	0.17	3.40	0.49	3.24
Glyceraldehyde-3-phosphate	C00118	-	-	-	0.17	0.17	-	0.65
Glycolate	C00160	-	-	-	-	0.17	-	0.09
Glyoxylate	C00048	-	-	-	-	0.17	-	-
GTP	C00044	4.87	-	0.90	-	-	-	0.14
KDPG	C04442	-	-	0.00	-	-	-	-
Malate	C00149	-	0.49	0.48	0.17	6.79	0.19	0.20
NADP	C00006	0.00	2.14	1.17	0.17	-	-	0.97
NADPH	C00005	0.12	0.14	-	0.24	-	-	-
Phosphoenolpyruvate	C00074	0.18	6.79	1.49	0.51	6.79	1.09	2.90
Phenylalanine	C00079	0.04	-	0.12	-	-	0.13	0.25
Ribulose-5-phosphate	C00199	-	0.02	0.37	0.10	5.09	0.05	0.03
Ribulose-1,5-bisphosphate	C01182	-	0.85	5.91	0.05	17.15	-	0.48
Sucrose	C00089	-	-	-	-	-	-	-

References: [\(Bennett et al. 2009; Nishiguchi et al. 2019; Yoshikawa et al. 2013; Shastri and Morgan 2007; Hasunuma et al. 2013; Dempo et al. 2014; Takahashi, Uchimiya, and Hihara 2008\)](#)

Table S3. Changes in fructose/sedoheptulose biphosphatase kinetic parameters in the presence of metabolites. The changes in kinetic parameters are presented as percentages of the parameters of the untreated control sample, with statistically significant changes outlined in blue.

Metabolite	K_M	k_{cat}	k_{cat}/K_M	Hill Coefficient
<i>Synechocystis fbpl</i>				
AcCoA	63.06%	83.83%	132.97%	117.43%
Citrate	138.67%	85.53%	61.67%	97.56%
GAP	48.34%	95.96%	198.55%	118.33%
NADPH	63.24%	67.10%	106.10%	114.41%
<i>Curpriavidus fbp3</i>				
GAP	62.65%	108.98%	173.95%	128.66%
NADPH	50.88%	64.80%	127.35%	73.60%

Table S4. Changes in transketolase kinetic parameters in the presence of metabolites.

The changes in kinetic parameters are presented as percentages of the parameters of the untreated control sample, with statistically significant changes outlined in blue.

Metabolite	K_M	k_{cat}	k_{cat}/K_M	Hill Coefficient
<i>Synechocystis tktA</i>				
2OG	96.16 %	99.16 %	103.12 %	110.62 %
2PG	98.16 %	95.31 %	97.10 %	113.42 %
3PGA	107.78 %	98.24 %	91.15 %	105.18 %
AcCoA	113.92 %	96.45 %	84.67 %	97.40 %
AMP	208.67 %	98.41 %	47.16 %	81.80 %
ATP	82.05 %	87.96 %	107.20 %	117.43 %
Citrate	93.59 %	94.93 %	101.43 %	102.05 %
G6P	97.53 %	93.26 %	95.62 %	104.38 %
Glyoxylate	117.63 %	101.03 %	85.88 %	95.19 %
GTP	119.05 %	98.75 %	82.95 %	94.58 %
KDPG	111.03 %	99.02 %	89.18 %	93.42 %
NADP	102.91 %	99.61 %	96.80 %	108.35 %
RuBP	127.30 %	102.65 %	80.63 %	96.76 %
<i>Curpriavidus cbbTP</i>				
2OG	91.40 %	95.68 %	104.69 %	103.43 %
2PG	89.82 %	94.27 %	104.96 %	107.15 %
AMP	132.17 %	107.07 %	81.01 %	87.22 %
ATP	103.74 %	100.28 %	96.67 %	96.79 %
Citrate	91.32 %	93.60 %	102.50 %	103.64 %
DHAP	136.73 %	89.06 %	65.13 %	91.86 %
G6P	119.82 %	103.78 %	86.61 %	91.95 %
Glyoxylate	101.67 %	91.96 %	90.45 %	99.81 %
NADP	144.32 %	99.69 %	69.08 %	87.31 %
Malate	100.71 %	95.56 %	94.89 %	116.27 %

Supplementary References

- Asplund-Samuelsson, Johannes, Markus Janasch, and Elton P. Hudson. 2018. "Thermodynamic Analysis of Computed Pathways Integrated into the Metabolic Networks of E. Coli and Synechocystis Reveals Contrasting Expansion Potential." *Metabolic Engineering* 45 (January): 223–36.
- Bennett, Bryson D., Elizabeth H. Kimball, Melissa Gao, Robin Osterhout, Stephen J. Van Dien, and Joshua D. Rabinowitz. 2009. "Absolute Metabolite Concentrations and Implied Enzyme Active Site Occupancy in Escherichia Coli." *Nature Chemical Biology* 5 (8): 593–99.
- Dempo, Yudai, Erika Ohta, Yasumune Nakayama, Takeshi Bamba, and Eiichiro Fukusaki. 2014. "Molar-Based Targeted Metabolic Profiling of Cyanobacterial Strains with Potential for Biological Production." *Metabolites* 4 (2): 499–516.
- Hasunuma, Tomohisa, Fumi Kikuyama, Mami Matsuda, Shimpei Aikawa, Yoshihiro Izumi, and Akihiko Kondo. 2013. "Dynamic Metabolic Profiling of Cyanobacterial Glycogen Biosynthesis under Conditions of Nitrate Depletion." *Journal of Experimental Botany* 64 (10): 2943–54.
- Lempp, Martin, Niklas Farke, Michelle Kuntz, Sven Andreas Freibert, Roland Lill, and Hannes Link. 2019. "Systematic Identification of Metabolites Controlling Gene Expression in E. Coli." *Nature Communications* 10 (1): 4463.
- Marcus, Y., E. Harel, and A. Kaplan. 1983. "Adaptation of the Cyanobacterium Anabaena Variabilis to Low CO₂ Concentration in Their Environment." *Plant Physiology* 71 (1): 208–10.
- Mo, Ran, Mingkun Yang, Zhuo Chen, Zhongyi Cheng, Xingling Yi, Chongyang Li, Chenliu He, et al. 2015. "Acetylome Analysis Reveals the Involvement of Lysine Acetylation in Photosynthesis and Carbon Metabolism in the Model Cyanobacterium Synechocystis Sp. PCC 6803." *Journal of Proteome Research* 14 (2): 1275–86.
- Nishiguchi, Hiroki, Natsuki Hiasa, Kiyoka Uebayashi, James Liao, Hiroshi Shimizu, and Fumio Matsuda. 2019. "Transomics Data-Driven, Ensemble Kinetic Modeling for System-Level Understanding and Engineering of the Cyanobacteria Central Metabolism." *Metabolic Engineering* 52 (March): 273–83.
- Shastri, Avantika A., and John A. Morgan. 2007. "A Transient Isotopic Labeling Methodology for ¹³C Metabolic Flux Analysis of Photoautotrophic Microorganisms." *Phytochemistry* 68 (16-18): 2302–12.
- Takahashi, Hideyuki, Hirofumi Uchimiya, and Yukako Hihara. 2008. "Difference in Metabolite Levels between Photoautotrophic and Photomixotrophic Cultures of Synechocystis Sp. PCC 6803 Examined by Capillary Electrophoresis Electrospray Ionization Mass Spectrometry." *Journal of Experimental Botany* 59 (11): 3009–18.
- Yang, Mingkun, Hui Huang, and Feng Ge. 2019. "Lysine Propionylation Is a Widespread Post-Translational Modification Involved in Regulation of Photosynthesis and Metabolism in Cyanobacteria." *International Journal of Molecular Sciences* 20 (19). <https://doi.org/10.3390/ijms20194792>.
- Yoshikawa, Katsunori, Takashi Hirasawa, Kenichi Ogawa, Yuki Hidaka, Tsubasa Nakajima, Chikara Furusawa, and Hiroshi Shimizu. 2013. "Integrated Transcriptomic and Metabolomic Analysis of the Central Metabolism of Synechocystis Sp. PCC 6803 under Different Trophic Conditions." *Biotechnology Journal* 8 (5): 571–80.
- Zavřel, Tomáš, Marjan Faizi, Cristina Loureiro, Gereon Poschmann, Kai Stühler, Maria Sinetova, Anna Zorina, Ralf Steuer, and Jan Červený. 2019. "Quantitative Insights into the Cyanobacterial Cell Economy." *eLife* 8 (February). <https://doi.org/10.7554/eLife.42508>.